Manipulating Surface Energy to form Compound Semiconductor Nanostructures

by

Matthew T. DeJarld

A dissertation submitted in partial fulfillment
of the requirements for the degree of
Doctor of Philosophy
(Materials Science and Engineering)
in the University of Michigan
2016

Doctoral Committee:

Professor Joanna Mirecki-Millunchick, Chair
Professor Chris Pearson
Professor Jamie Dean Phillips
Associate Professor Pierre Ferdinand Poudeu-Poudeu

©Matt DeJarld 2016

Acknowledgements

The research presented in this work has been highly collaborative. I am very grateful to my research group including former lab mates including Dr. Kevin Grossklaus, Dr. Adam Duzik, and Dr. Andrew Martin, who helped teach me various lab equipment and analytical techniques. I also want to recognize my current lab mates, Lifan Yan, Ryan Tait, Evan Anderson who have helped me with experiments and equipment maintenance over the past few years. A special thanks is given to Lifan Yan who lent me her nanostructure characterization expertise for multiple projects.

A great deal of credit is due to the various researchers outside our research group. This includes Prof. Jamie Phillips, Prof. David Blaauw, Dr. Alan Teran, and Eun Seong Moon in the Electrical Engineering Department. Their expertise in semiconductor based devices and semiconductor processing have been vital for the success of my research. I also want to give credit to Prof. Vanessa Sih and Marta Luengo-Kovac in Physics who have been co-authors on many of my publications. Other collaborators include Dr. Erwin Smakman, and Prof. Paul Koenraad of the Eindhoven Technical University, and the Michigan Center for Materials Characterization. I also want to thank Dr. Hirak Parikh for his mentorship during the NSF I-CORPS program in New York.

I would also like to acknowledge the various funding sources for this work including the NSF through Grant No. DMR-0906909, and the I-CORPS program, the NIH though

grant No.1 R01 CA195655-01, and Center for Solar and Thermal Energy Conversion, an Energy Frontier Research Center funded by the U. S. Department of Energy, Office of Science, Basic Energy Sciences under Award No. #DE-SC0000957.

Table of Contents

Acknowledgements ii

List of Figures viii

Chapter 1 Introduction and Background 1

1.1 Introduction 1
1.2 Objectives 2
1.2.1 GaSb Quantum Dots 3
1.2.2 GaAs Nanowires 4
1.3 Scientific Background 5
1.3.1Overview of Compound Semiconductors 5
1.3.1 Nanotechnology 9
1.3.3 Surface Energy 13
1.4 Experimental Methods: Growth and Characterization Techniques 16
1.4.1 Molecular Beam Epitaxy 16
1.4.2 Scanning Probe Microscopy 22
1.4.3 Electron Microscopy 24
1.4.4 Photoluminescence 25
1.4.5 Atom Probe Tomography 26
1.4.6 Kinetic Monte Carlo Simulations 27
1.5 References 28

Chapter 2 Capping Chemistry in GaSb/GaAs Quantum Dots 33

2.1 Introduction 33

2.2 Experimental Methods 34
2.3 Data Analysis 36
2.3.1 $Al_xGa_{1-}As$ Capping of GaSb Quantum Dots 36
2.3.2 Defect Formation under Aluminum Capping 38
2.3.3 Statistical analysis of capped quantum dots 40
2.3.4 Photoluminescence of $Al_xGa_{1-x}As$ capped GaSb Quantum Dots 42
2.4 Conclusions 46
2.5 References 47
Chapter 3 Droplet Epitaxy in Lattice Mismatched Systems 50
3.1 Introduction 51
3.2 Experimental Methods 52
3.3 Data Analysis 53
3.3.1 GaSb Quantum Dots grown by Droplet Epitaxy 53
3.3.2 Droplet Epitaxy Mechanisms in Lattice Mismatched systems 57
3.3.3 Morphology Control with Droplet Epitaxy 60
3.3.4 Kinetic Monte Carlo Simulations 64
3.4 Conclusions 66
3.5 References 67
Chapter 4 A comparison of SK and DE quantum dot growth mechanisms in GaSb/GaAs system 73
4.1 Introduction 74
4.2 Experimental Methods 75
4.3 Data Analysis 76
4.3.1 Morphology of SK and DE quantum dots 76
4.3.2 Antimony Compositional Profiles of SK and DE quantum dots 79
4.3.3 Structural Analysis of SK and DE quantum dots 81
4.3.4 Photoluminescence of SK and DE quantum dots 86
4.4 Conclusions 90
4.5 GaSb Quantum Dot Motivations and Applications 90

4.6 References ... 92
Chapter 5 GaAs Nanowires for on-chip optoelectronic device integration ... 97
5.1 Introduction ... 97
5.2 Experimental Methods ... 99
5.3 Data Analysis ... 101
5.3.1 Growth on Polycrystalline films ... 101
5.3.2 Doping and Nanowire Formation ... 108
5.3.3 Structural and Optical Characteristics of Doped Nanowires ... 110
5.3.4 Effect of Surface Energy and Growth on Metallic Films ... 116
5.3.5 Temperature Dependent Photoluminescence ... 119
5.3.6 Core-Shell Nanowires ... 123
5.4 Conclusions ... 130
5.5 References ... 131
Chapter 6 Bismuth as a catalyst for GaAs nanowire growth ... 140
6.1 Introduction ... 140
6.2 Experimental Methods ... 142
6.3 Data Analysis ... 143
6.3.1 Bismuth Catalyst Formation and Desorption ... 143
6.3.2 Self-terminating VLS growth ... 147
6.3.3 Catalyst destabilization mechanism ... 148
6.3.4 Other Material Systems ... 155
6.4 Conclusions ... 156
6.5 GaAs Nanowire Motivation and Applications ... 156
6.6 References ... 158
Chapter 7 Summary and Future Work ... 167
7.1 Summary and Conclusions ... 167

7.2 Future Work 170
7.3 References.. 173

List of Figures

Figure 1.1: Plot of the bandgap energy as a function of lattice parameter for commonly used III-V semiconductor materials.[14] 7

Figure 1.2. Energy band structure of GaAs with respect to momentum space K.[16]......... 8

Figure 1.3: Illustration demonstrating the differences in the density of states for a) 3D bulk materials, b) 2D quantum wells, c) 1D nanowires, and d) 0D quantum dots.[27] 11

Figure 1.4: Electron microscope images and schematics of the three primary nanostructures, the a) quantum well, the b) nanowire, and the c) quantum dot........ 12

Figure 1.5: Schematic showing a liquid droplet on a solid substrate where the droplet has a) high, b) moderate, and c) low surface energy relative to the substrate. 14

Figure 1.6: The EPI 930 solid-source MBE chamber used for the growths presented in this work........ 16

Figure 1.7: A schematic of the MBE chamber showing the relative positions of the sample stage, effusion cells, shutters, and RHEED gun........ 17

Figure 1.8: Schematic detailing the a) epitaxial b) critical thickness and c) island growth stages in the Stranski-Krastanov growth mode........ 20

Figure 2.1: Select XSTM images of GaSb quantum dots capped with a) GaAs, b) 1ML AlAs, c) 3ML AlAs, and d) 20nm of $Al_{0.5}Ga_{0.5}As$ 37

Figure 2.2: a) Topographical and b) Current XSTM images of a defected GaSb quantum dot capped with $Al_{0.6}Ga_{0.5}As$........ 39

Figure 2.3: Ball-and-stick model of defects form in GaAs capping layer surrounding a GaSb quantum dot........ 40

Figure 2.4: Bar graphs detailing the fraction of measurements vs. quantum dot height in a) GaAs, b) 1ML AlAs, c) 3ML AlAs, and d) $Al_{0.5}Ga_{0.5}As$ samples that are intact, disintegrated, and defected 41

Figure 2.5: Normalized photoluminescence measurements of the four capped samples 44

Figure 2.6: Chart showing the ground state emission for simulated quantum dots with various heights 45

Figure 3.1: AFM images of nanostructures grown by droplet epitaxy at substrate temperatures of a) 200°C, b) 250°C, and c) 300°C 55

Figure 3.2: AFM images of a a) single halo nanostructure and of b) multiple halo nanostructures grown at 400°C 56

Figure 3.3: Schematic illustrating toroid formation that occurs during the initial stages of droplet epitaxy crystallization 60

Figure 3.4: AFM scan of ring shaped GaSb nanostructures with protrusions grown at 250°C 62

Figure 3.5: AFM image of ring GaSb nanostructures grown at 250°C after depositing 4 monolayers of Ga. 63

Figure 3.6: Kinetic Monte Carlo Simulations of toroids before and after annealed at a,b) 300°C and c,d) 400°C 65

Figure 4.1: Atomic Force Micrographs of uncapped a) SK and b) DE nanostructures. . 77

Figure 4.2: Planar sections of Atom Probe Tomography reconstructions showing the distribution of Sb atoms for a) SK and b) DE nanostructures. Areas in the APT reconstructions with at least 9% Sb concentration or higher are shaded in purple. 78

Figure 4.3: Cross-sectional contour maps of the Sb concentration in both a) SK and b) DE nanostructures. Single line Sb compositional profiles through the c) nanostructures and the d) wetting layer in both SK and DE samples. 80

Figure 4.4: TEM images of capped a-c) SK and d-e) DE nanostructures. High resolution images of an b) intact SK dot, a c) defected SK dot and e) DE ring........ 82

Figure 4.5: EELS analysis of a)SK and b) DE quantum to dots. A TEM image showing the sampling area (dotted line) is included 84

Figure 4.6: Photoluminescence measurements of a) SK quantum dots and b) DE quantum dots with the GaAs substrate peak removed. Measurements were taken at 10K by a 633nm HeNe laser with a spot size of 5 μm and an intensity of 3mW 87

Figure 4.7: a) AFM image showing GaSb Discs grown by droplet epitaxy and b) Photolumminescence measurements of SK dots, DE rings, and DE disks. Measurements were taken in the same manner as Figure 4.6 89

Figure 5.1: a) Top down and b) cross sectional scanning electron microscope (SEM) images of GaAs nanowires grown on indium tin oxide (ITO) for 30 minutes. c) High magnification SEM image of the GaAs-ITO interface, with the interface between the ITO and GaAs (dotted line) indicated. 102

Figure 5.2: Cross-sectional SEM micrographs of Nanowires grown on ITO after a) 5 min, b) 20 minutes, and c) 60 minutes. All scale bars are 500nm. 104

Figure 5.3: Statistical measurements of nanowire samples grown on ITO with growth times between 5 and 60 minutes. a) Nanowire forest height, b) nanowire orientation angle and the c) continuous film thickness are measured. 106

Figure 5.4: Cross-sectional SEM images of GaAs nanowires grown on ITO for 15 minutes with a) no doping, b) Si doping, and c) Be doping. 109

Figure 5.5: Transmission Electron Microscope images and diffraction patterns of a-b) undoped, c-d) Si doped, and e-f) Be doped GaAs nanowires grown on ITO. 112

Figure 5.6: Photoluminescence data of nanowires grown on ITO with a) no doping, b) Si doping, and c) Be doping. (inset) Current Density vs Electrical Potential of Be doped nanowires. 113

Figure 5.7: Plan-view SEM images of GaAs nanowires grown on Pt films at a) low Ga fluxes ($6x10^{-7}$ Torr) and b) high Ga fluxes ($9x10^{-7}$ Torr) along with the addition of c) Si and d) Be dopants at the higher deposition rate. 117

Figure 5.8: a) Cross-sectional SEM images of Be-doped GaAs nanowires grown for 30 minutes on a Ti film. b) I-V characteristics of Be-doped nanowires on Ti. 118

Figure 5.9: Temperature dependent photoluminescence of Be nanowires on Ti. 120

Figure 5.10: The photoluminescence peak energy positions vs temperature of Be doped nanowires on Ti.. 121

Figure 5.11: The integrated photoluminescence peak intensity vs inverse temperature of Be doped GaAs nanowires on Ti 122

Figure 5.12: GaAs core-shell nanowires grown on a-b) ITO and c-d) Ti substrates with varied shell deposition steps. 125

Figure 5.13: GaAs nanowires grown on ITO with a-b) low and c) high Be and Si doping levels. Each doping step was either a,c) 7.5 min or b,d) 15 min long. 128

Figure 6.1: Planar SEM images of growths at T_s=320°C with increasing Bi fluxes and correspond to a) sample A b) sample B and c) sample C. 143

Figure 6.2: Cross-sectional SEM images of Bi droplets on sample D at T_s=360°C. 145

Figure 6.3: 45° angled SEM image of staircase nanostructures formed on sample E. Identical structures also appeared on Sample F. 148

Figure 6.4: Schematic illustrating the stages of staircase nanostructure formation. a) Initial Bi_ℓ droplet formation, b) catalysis of GaAs VLS growth c) droplet growth with pinned edges, d) droplet destabilization by the Gibb's Criterion, e) droplet growth with sidewall wetting, f) droplet destabilization by substrate contact, g) droplet re-equilibrates on substrate, and h) growth of a new disc. 150

Figure 6.5: SEM images of nanowire features that are overgrown observed in a) Sample I and b) Sample J as well as nanowire features above the surface in c) Sample K and Sample L 154

Figure 6.6: Bi droplets on InAs without concurrent InAs deposition on a) Sample M and with concurrent InAs deposition on b) Sample N 155

Figure 7.1: Schematic illustrating a proposed P-N-P nanowire device to measure the PN junction in GaAs nanowires. a) Core-shell nanowire and b) favorable and c) unfavorable P-N-P structure... 172

Chapter 1
Introduction and Background

1.1 Introduction

Nanotechnology, and more generally the prefix “nano” has been a prominent buzzword in both scientific and public communities for the better half of two decades. Conceptually introduced by Dr. Richard Feynman, the word nanotechnology is defined as science and engineering conducted at the scale of 1-100 nanometers.[1] In the 1990’s companies based solely on nanotechnology first started to appear. By the year 2000, nanotechnology began to emerge in consumer markets in products such as antibacterial silver nanoparticles, nanostructured scratch-resistant coatings, and deep-penetrating cosmetics.[2] At the same time, US president Bill Clinton began an initiative known as the National Nanotechnology Initiative (NNI) to advance nanotechnology research and find new nanotechnology based applications.[3] As materials fabrication and processing methods advanced, the scale of devices across all scientific disciplines shrank, and nanotechnology became commonplace. Today nanotechnology is not a field on its own, but the industry standard in areas like computer processing, pharmaceuticals, energy storage, and more.[4] Despite this, new applications utilizing nanotechnology are continually being developed, enabled in part by advances in nanostructure fabrication methods.

Semiconductor based nanostructures are of particular interest because of the widespread use of semiconductors in electronics. The ability to exhibit quantum confinement on electronic carriers allows for a wide range of new applications in quantum computing,[5] photovoltaics,[6] light emission,[7] transistors,[8] and optics.[9] In addition to quantum effects, nanostructures have unique fabrication processes and can enable the integration of semiconductor based devices with dissimilar materials, allowing for flexible electronics[10] and advanced forms of biological sensing.[11] Despite their potential, there are significant fundamental properties that need to be understood about semiconductor nanostructures before their widespread adoption in consumer devices. For example, embedded nanostructures are vital components to some heterostructure designs, but current fabrication processes often result in the nanostructures being inconsistent or damaged.[12] In other cases, high quality nanostructure growth has been demonstrated, but the growth regimes are significantly outside what is required for widespread integration. A deeper understanding of how material and growth parameters effect nanostructure development and optoelectronic properties is vital for the advancement of nanostructure based devices.

1.2 Objectives

The goal of this work is to discover effective ways in controlling the shape, structure, and composition of nanostructures during crystal growth. This is achieved by manipulating the surface energy of key growth components. Elemental, architectural, and kinetic modifications are demonstrated to significantly impact these semiconductor nanostructure systems. In this work I will analyze two different compound semiconductor nanostructures, GaSb quantum dots and GaAs nanowires.

1.2.1 GaSb Quantum Dots

The goal of this section is to obtain a deeper understanding of embedded GaSb quantum dots by changing surface energy and growth kinetics. This research is covered in chapters 2, 3, and 4 which discuss capping chemistry, droplet epitaxy growth kinetics, and embedded quantum dot structure respectively. These studies provide further insight into the relationships between GaSb quantum dot structure and their characteristic optical spectrum. Each study can be separated as follows:

The goal of Chapter 2 is to investigate the role of surface chemistry on embedded quantum dot structure. Specifically, GaSb quantum dots grown by the Stranski Krastanov method are overgrown with different semiconductor compounds (a process known as capping). The different compounds change the surface energy but not the lattice induced strain. This is achieved by incorporating Al_x into the $Ga_{1-x}As$ capping layer. The key finding of this chapter is that the surface energy of the capping layer does impact the quantum dot's structural integrity and can be used to prevent shape demolition. Increasing the surface energy of the capping layer prevents out diffusion of GaSb material, but at the cost increasing the strain due to a taller structure.

The goal of Chapter 3 is to investigate the mechanisms of lattice mismatched droplet epitaxy, specifically GaSb droplet epitaxy on GaAs substrates. The key finding of this chapter is that the energy of crystallization (E_c) is not insignificant and manifests in the form of an incubation time during which no crystallization occurs. A qualitative model is presented to describe the differing morphologies and can be used to control droplet epitaxy in strained systems. We demonstrate that this method can be used as an alternative to the Stranski Krastanov growth for epitaxial quantum dot formation

The goal of Chapter 4 is to compare the characteristics of capped GaSb quantum dots grown by Stranski-Krastanov and by droplet epitaxy. The key finding of this chapter is that there is inhomogeneity between the topography and composition of droplet epitaxy nanostructures. Furthermore, the Sb concentration, size, and capping layer strain is significantly different in the Stranski-Krastanov and droplet epitaxy quantum dots. Despite this, both samples have nearly identical photoluminescence spectra, suggesting the emission is emanating from a shared feature such as the wetting layer and the large Stranski-Krastanov quantum dots are not luminescent.

1.2.2 GaAs Nanowires

The goal of this section is to analyze nanowire growth under conditions more favorable to CMOS integration and widespread adoption. We present a concept for integrating optoelectronic devices using nanowires as well as study the physics governing nanowire formation. This section contains chapters 5 and 6 which discuss nanowire growth on polycrystalline films and Bi catalyzed nanowire growth respectively.

The goal of Chapter 5 is to provide a deeper understanding of GaAs nanowire growth on conducting polycrystalline films at temperatures suitable for on-chip

applications. The key finding of this chapter is that high quality nanowire growth on polycrystalline film at low temperatures is feasible through the use of specific dopants. Incorporating Be during deposition significantly improves the nanowire morphology, crystal structure, and optical characteristics. Temperature dependent photoluminescence emission of Be-doped nanowires, in combination with structural and electrical characterization, suggests they are of high enough quality for integrated optoelectronic devices.

The goal of Chapter 6 is to investigate the use of Bi as a catalyst for vapor-liquid-solid (VLS) nanowire growth. The key finding of this chapter is that VLS growth is capable with a Bi catalyst but difficult because of Bi's volatility at growth temperatures. It is demonstrated that nanowire formation can fail during growth due to excessive sidewall wetting by the catalyst.

1.3 Scientific Background

1.3.1 Overview of Compound Semiconductors

The type of materials used in this work are III-V compound semiconductors. The semiconductor material class is famous for their role in creating the age of computers.

Semiconductors have conducting properties between that of an insulator and a metal, and can be modified by use of doping elements.[13] Compound semiconductors are composed of two or more materials that form a semiconductor when alloyed together. The most common compound semiconductors are the III-V and II-IV semiconductors, which consist of materials in group III/II of the periodic table bonding with materials in group V/IV respectively. This work is focused solely on III-V semiconductors in the Al,Ga,As,Sb,Bi systems. The ability to alloy multiple III-V semiconductor materials into ternary and quaternary compounds allows the growth engineer to tune the characteristic energy band gap. The band gap is the gap in energy states between the conduction band minimum and the valence band maximum. **Figure 1.1** is a plot of bandgap vs lattice parameter.[14] The lines connecting III-V compounds show the representative energy ranges of the ternary alloys.

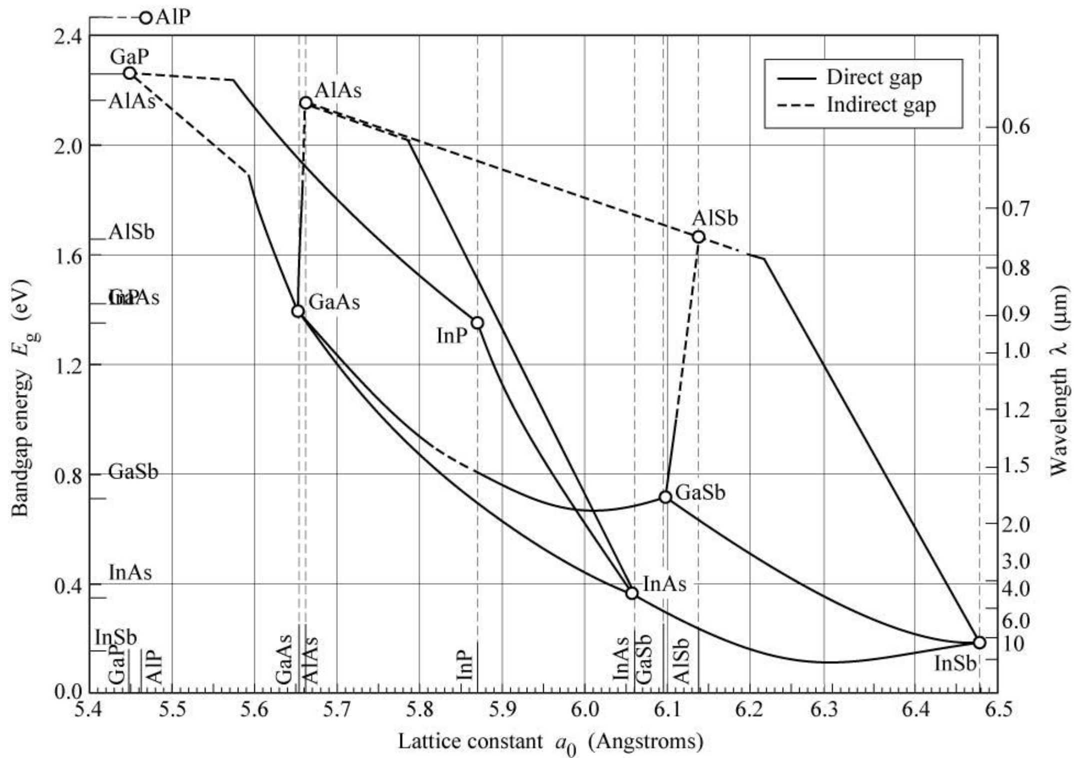

Figure 1.1: Plot of the bandgap energy as a function of lattice parameter for commonly used III-V semiconductor materials.[14]

Most III-V semiconductors have a direct band gap, in which the valence band maximum and conduction band minimum are at the same position in momentum space.[15] **Figure 1.2** is an E-k diagram of GaAs. An E-k diagram plots the electron energy states against the wave vector.[16] In **Figure 1.2** the conduction band minimum and the valence band maximum are both at the same position in k-space. In **Fig. 1.2** this is the Γ-point and the valence band minimum has an energy value of 0eV. This means an electron can excite from the valence band to the conduction band without any additional momentum.[13] The energy required for this is equal to the energy separation in **Fig. 1.2** and is referred to as the energy band gap (E_G). In the case of direct band gap semiconductors, this energy can be provided by absorbed photons, as photons have very little momentum.[15] For this reason III-V semiconductors are ideal for devices that require photon absorption,

such as photodetectors and photovoltaics. Furthermore, by pumping current across the band gap, these materials can act as a light emitting diode or laser.

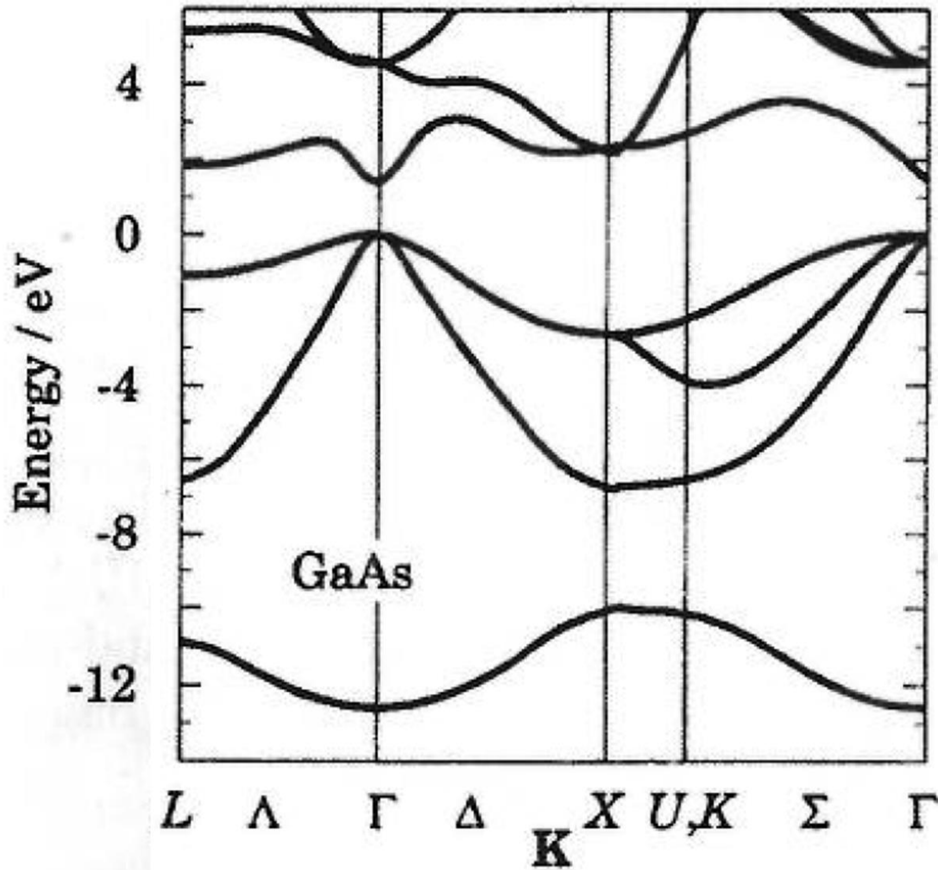

Figure 1.2. Energy band structure of GaAs with respect to momentum space K.[16]

As mentioned earlier, the compound semiconductors this work will be focused on are $Al_xGa_{1-x}As$, GaAs, GaSb, GaAs with dilute Bi. GaAs is one of the most common compound semiconductor and holds the record for a single junction solar cell at 28.8%.[17] GaAs was also used in the development of the first laser.[18] As such, it is an ideal compound semiconductor to demonstrate novel structures for optoelectronic devices. It can easily be alloyed with lattice matched AlAs to tune the bandgap energy from 1.42eV to 2.23eV[14] and $Al_xGa_{1-x}As$ alloys are often used in conjunction with GaAs solar cells and

light emitting devices because of its wider bandgap.[19] GaSb has a much narrower energy bandgap at 0.726eV.[20] Because of this GaSb and its alloys are often targeted for applications using infrared light.[21] Recently, increasing infrared light absorption has become a strategy for improving photovoltaic technologies.[22] Some approaches include integrating GaSb and other lower energy bandgap materials with other photovoltaic technologies.[23]

1.3.1 Nanotechnology

Quantum Confinement

In the bandgap model mentioned earlier, carriers can transfer between the valence band and conduction band through excitation and relaxation. Both the valence band and conduction band have a certain amount of states for carriers to occupy at a given energy. This is known as the density of states (DOS).[24] Using electron wavevectors, the DOS can be found by deriving the electron volume in k-space with respect to energy. In a three dimensional structure, it can be shown that the density of states is proportional to the square root of the energy and continuous over all energy ranges. The separation of energy between the states in the valence band and the conduction band is what is labeled as the bandgap.[24]

As the physical dimensions of a material approach the scale of its de Broglie wavelength, the optical and electronic properties start to deviate significantly from its bulk properties.[5] These dimensions are different depending on the material, but are typically on the nanometer scale. At these size scales the electron wavefunction becomes confined and bandgap increases as the conduction band shifts towards higher energies.

Furthermore, carriers can only occupy discrete energy levels. The model for particle in a box in 3-D demonstrates the relationship between energy and dimension (1).[25] In this equation E is the energy of the exciton state, m^* is the effective mass, h is the planck constant, L is the length in the Cartesian coordinate system, and n is the discrete energy state in the respective dimension. As the dimensions shrink, the energy increases. While this model is useful for predicting the relative shift in energy at the nanoscale, other factors such as strain can have a significant impact on the final value.[26]

$$E = \frac{h^2}{8m^*}\left(\frac{n_x^2}{L_x^2} + \frac{n_y^2}{L_y^2} + \frac{n_z^2}{L_z^2}\right) \quad (1)$$

The quantization of energy states in the bandgap is dependent on dimensionality. If a material has bulk-like length scales in two direction, and nanoscale dimensions in one direction, it is known as a 2D material, and exhibits quantum confinement in only one dimension. This has an impact on the DOS and the quantization can be visualized for 2D materials. Further reducing the length in other dimensions can result in 1D and 0D materials that exhibit two dimensional and three dimensional quantum confinement respectively. **Figure 1.3** visualizes the effect of the DOS with regards to different levels of confinement. In 2D materials, the DOS is independent of energy within finite energy ranges, and this confinement is increased with 1D and 0D materials.[27]

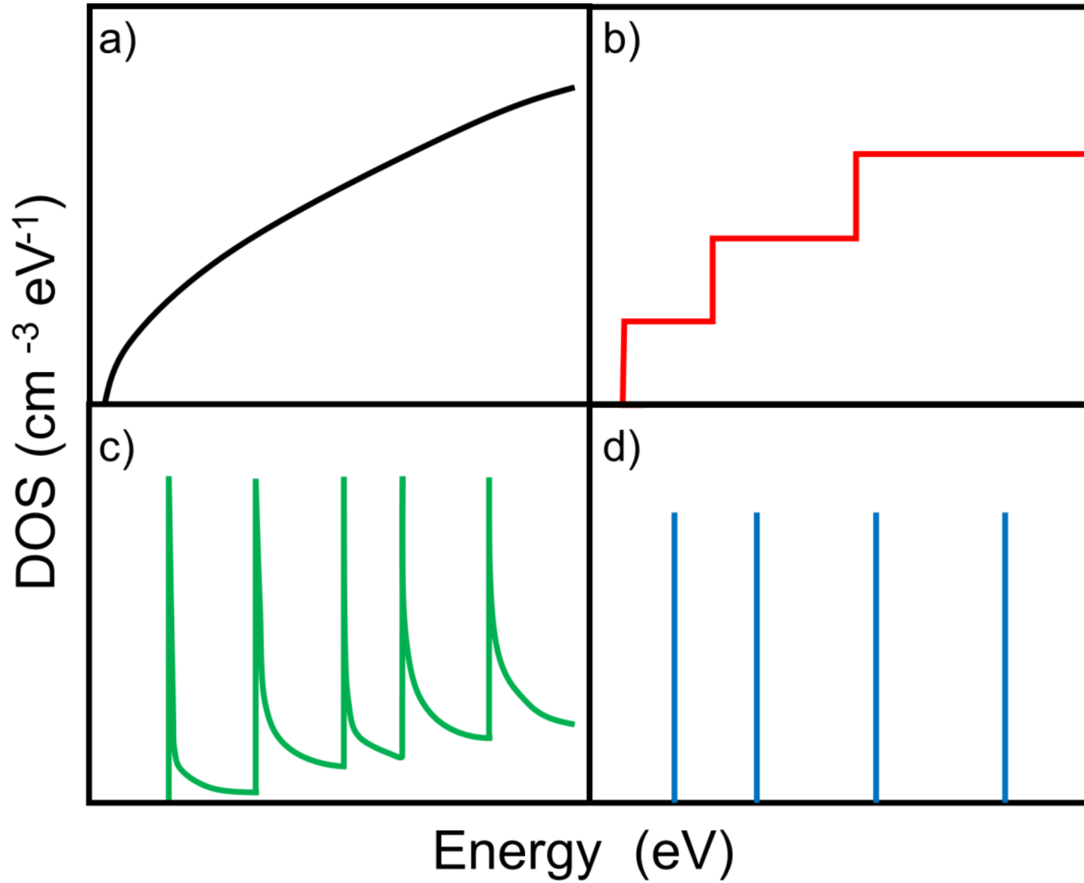

Figure 1.3: Illustration demonstrating the differences in the density of states for a) 3D bulk materials, b) 2D quantum wells, c) 1D nanowires, and d) 0D quantum dots.[27]

Nanostructures

Structures that have such small dimensions and can exhibit quantum confinement have been labeled as nanostructures, due to their nanometer sized features. There are many creative and unique nanostructures, but the fundamental three are presented in **Figure 1.4.** These three nanostructures are often the simplest to fabricate and are the types included in the results of the experimental work presented in this thesis.

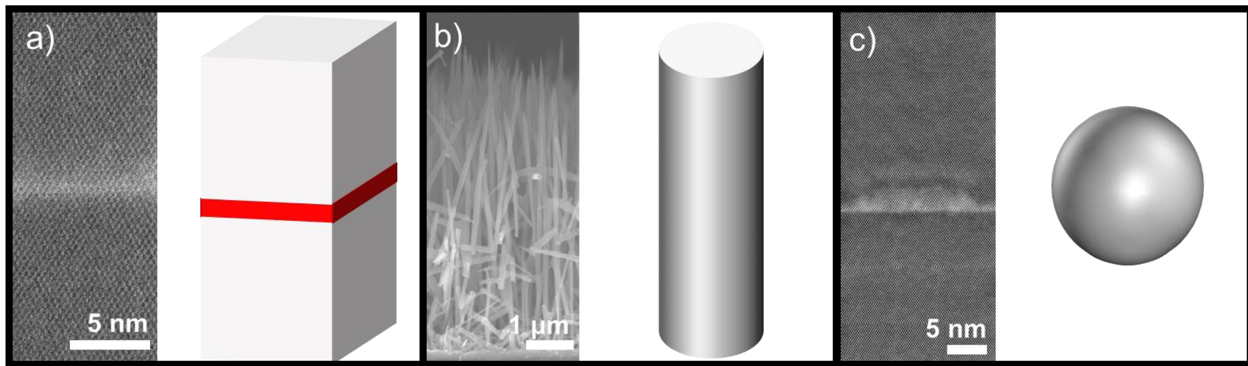

Figure 1.4: Electron microscope images and schematics of the three primary nanostructures, the a) quantum well, the b) nanowire, and the c) quantum dot

Quantum Well: (**Fig. 1.4a**) A quantum well is thin layer of material that has quantum confinement in the direction perpendicular to the layer surface.[27] In semiconductors, the quantum well is typically fabricated by depositing a few monolayers of material between two subsequent films. Typically the quantum well material has a narrow bandgap relative to its surrounding films in order to act as a potential well.[28] Quantum wells are often used in devices such as laser diodes and high electron mobility transistors.[28,29] A TEM image of a GaSb quantum well in GaAs can be seen in **Fig. 1.4a.**

*Nanowire (***Fig. 1.4b**): A nanowire, also called a quantum wire, is a structure with nanometer sizes in two dimensions with a third unconstrained dimension. Typically the structure is cylindrical in shape with the diameter being constrained to the nanoscale, hence the "wire" part of the nomenclature.[27] However, nanowires with faceted cross-sections are possible depending on the crystal orientation and fabrication process.[30] Transistors and optoelectronic devices have been fabricated using nanowires but these devices have not yet achieved significant commercial success.[31] Due to their unique geometry nanowires significantly increase the amount of exposed surface area. This attribute offers many advantages for electrochemical based devices such as batteries and

biosensors.[11,32] Lastly, due to their spacing and diameter size, nanowire arrays exhibit light trapping effects that can improve the amount of light absorption.[33] An SEM image of GaAs nanowires can be seen in **Fig 1.4b.**

Quantum Dot (**Fig. 1.4c**): A quantum dot is a structure that can confine carriers in all three spatial dimensions.[27] Quantum dots can be fabricated using many different methods. Colloidal and solution based quantum dots are the most commercially successful and can be used as additives in many products.[34] The quantum dots presented in this work are all self-assembled epitaxial quantum dots. Semiconductor quantum dots are often used for their optical capabilities. By controlling the particle diameter, one can manipulate the wavelength of light associated with the quantum dot.[35] Quantum dots are also used to create single electron transistors which are necessary in studying electron entanglement and other phenomenon that require splitting of electron pairs.[36] A TEM image of a GaSb quantum dot embedded in GaAs can be seen in **Fig. 1.4c.**

1.3.3 Surface Energy

Surface energy significantly impacts the formation of nanostructures. Nanostructures typically have a high surface area/volume ratio and because of this surface effects play a key role in their fabrication.[37] In the case of GaSb quantum dots, the difference in surface energy of the GaSb quantum dot and GaAs capping layer influences the final quantum dot shape, morphology, and dimensions. In the case of GaAs nanowires, the difference in surface energy between the liquid catalyst and the substrate influence the diameter and quality of the nanowires.

Surface energy is the work per unit area done by a force to create a new surface.[13] The change in surface energy at an interface can determine whether the material will bead up as a sphere, or spread out as a thin film. **Figure 1.5** shows a liquid ℓ on a solid *s*. Depending on the surface energy of the liquid and solid, the liquid will form a sphere (**Fig. 1.5a**), a droplet (**Fig. 1.5b**), or a thin film (**Fig. 1.5c**). In the case of spherical formation (**Fig. 1.5a**) the surface energy of the liquid is high relative to the substrate, and the liquid prefers to minimize its surface area. In the case of wetting (**Fig. 1.5c**) the surface energy of the liquid is low relative to the substrate, and the liquid prefers to maximize the surface area. Wetting occurs when the liquid spreads completely across the surface forming a thin film. The angle between the liquid and the substrate is known as the contact angle (φ). If the liquid has a high surface energy, the contact angle approaches 180° (**Fig. 1.5a**) and if it has a low surface energy it approaches 0° (**Fig. 1.5c**).[13]

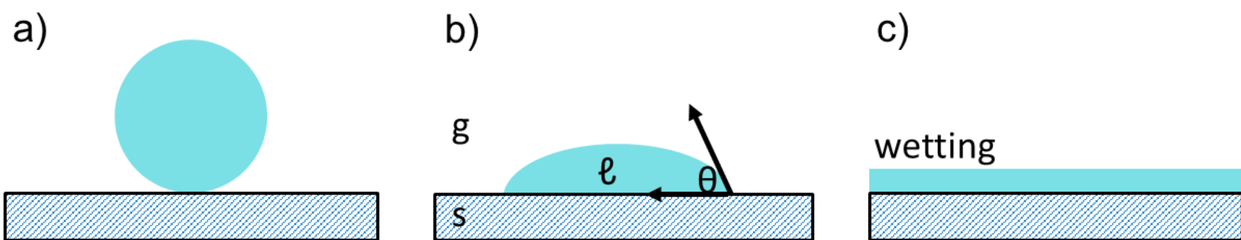

Figure 1.5: Schematic showing a liquid droplet on a solid substrate where the droplet has a) high, b) moderate, and c) low surface energy relative to the substrate.

One parameter used to determine the wettability of two materials is known as the Spreading Parameter (2), where S is the spreading parameter γ_s is the surface energy of the solid substrate, γ_ℓ is the surface energy of the liquid, and $\gamma_{s\text{-}\ell}$ is the interfacial energy

between the substrate and the liquid. If $S<0$ the liquid partially wets the substrate (**Fig. 1.5b**), and if $S>0$ the liquid completely wets the substrate (**Fig. 1.5c**).[38]

$$S = \gamma_s - \gamma_\ell - \gamma_{s\ell} \tag{2}$$

To more accurately determine the contact angle of liquids on an exposed surface, Young's equation using interfacial energies can be used (3), where γ_{sg} is the interfacial energy between the solid and gas phases, $\gamma_{s\ell}$ is the interfacial energy between the solid and liquid phases, $\gamma_{\ell g}$ is the interfacial energies between the liquid and gas phases, and φ is the contact angle.[13]

$$\gamma_{sg} = \gamma_{s\ell} + \gamma_{\ell g}\cos(\phi) \tag{3}$$

The examples presented here are for liquid-solid interfaces, but surface energy behaves similarly for solid-solid interfaces. For GaSb quantum dots capped with GaAs, the surface energies of solid-solid interfaces play a key role. For GaAs nanowires, the surface energies of liquid-solid interfaces play a key role.

1.4 Experimental Methods: Growth and Characterization Techniques

The purpose of this section is to provide a brief introduction to the various growth and characterization techniques and tools used in this work.

1.4.1 Molecular Beam Epitaxy

The bulk of the work presented here is concerning growths using solid source molecular beam epitaxy (MBE). MBE is a form of physical vapor deposition used to create ultra high quality thin films with monolayer precision. It is especially useful in the growth of crystalline semiconductors. Deposition in solid source MBE is achieved by heating various materials until they form an evaporative flux. This flux is directed towards a sample stage or substrate. The equipment used in these studies is an EPI 930 solid source MBE chamber. A picture of the lab equipment is presented in **Figure 1.6**.

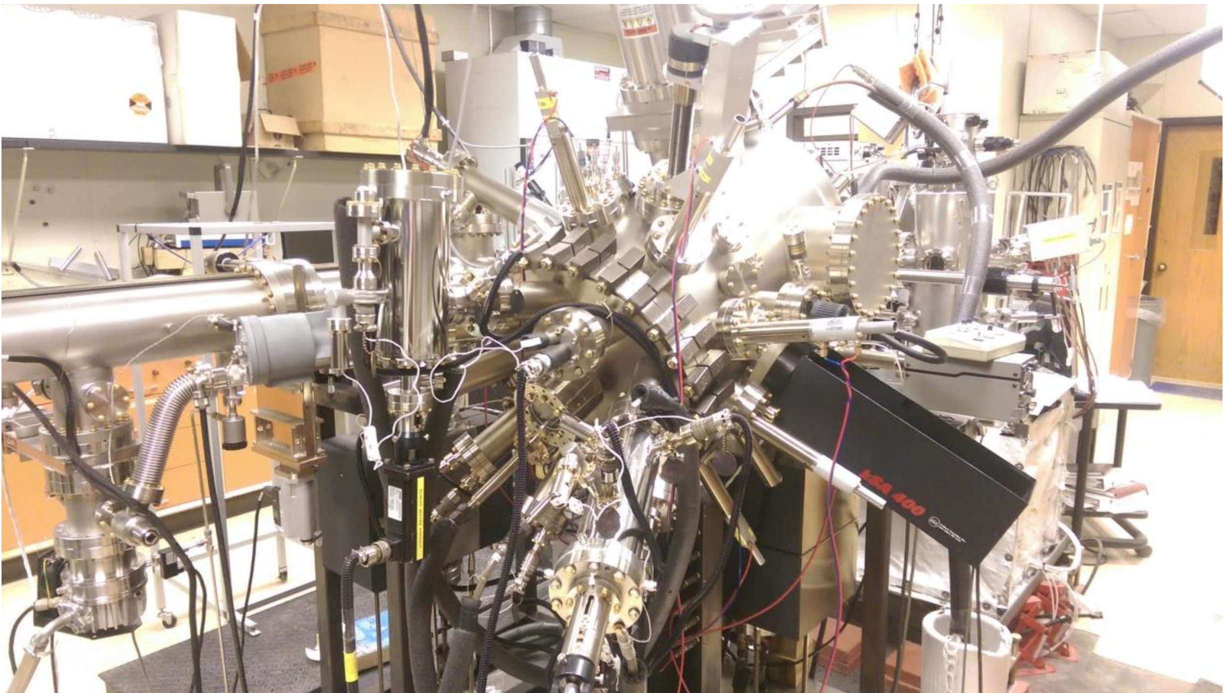

Figure 1.6: The EPI 930 solid-source MBE chamber used for the growths presented in this work.

General Information

The MBE chamber is operated at ultra-high vacuum (10^{-9}-10^{-11} Torr). This is achieved by using multiple pumps and cooling methods. The two types of pumps we utilize are throughput and capture pumps. Throughput pumps operate by compressing a gas through a vented outlet which is then removed by a secondary backing pump. Capture pumps operate by capturing the molecules in the vacuum via gettering or freezing.[39] In our system we have roughing pump, turbo pump, titanium ion pump and liquid helium cryo pump that can all operate on the MBE chamber simultaneously. In addition to these pumps there is a shroud around the MBE chamber which can be filled with liquid nitrogen. The liquid nitrogen cools the interior walls of vacuum chamber causing molecules to attach to it, reducing the vacuum by an order of magnitude.

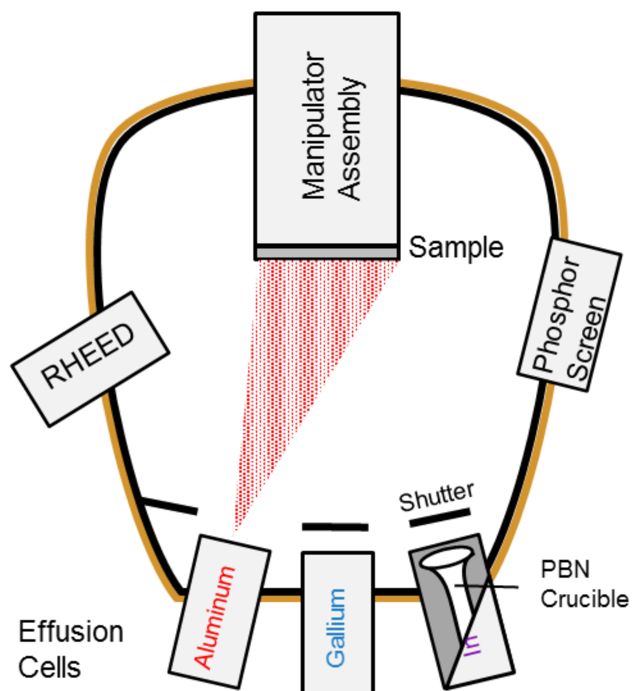

Figure 1.7: A schematic of the MBE chamber showing the relative positions of the sample stage, effusion cells, shutters, and RHEED gun.

Figure 1.7 is a schematic detailing the different components of the chamber in **Fig. 1.6**. In the center of the chamber is the sample stage. The sample stage is positioned so it faces the effusion cells. In the schematic, multiple effusion cells can be seen on the perimeter of one side of the chamber. These effusion cells are responsible for evaporating the different elemental source materials. Our chamber contains three different group III source materials (Ga, In, Al), three group V source materials (As, Sb, Bi), and two dopant source materials (Si, Be). For the group III, dopant, and Bi effusion cells, a pyrolytic boron nitride crucible is used. This crucible is filled with extremely pure ingots of each respective element. Heating coils surrounding the crucible heat the material until it forms an evaporative flux. During daily operation, the flux of these materials is controlled by changing the effusion cell temperature. For As and Sb, each effusion cell has a valved cracker. In this configuration the effusion cell consists of two independent components: the base and the cracking zone. Each component has its own heating elements and thermocouples. The base contains the pure elemental source material, and is constantly maintained at one elevated temperature. The cracking zone passes the material through a series of channels to break down larger molecules.[40] The cracking zone also provides means of differentiating between different molecules from the bulk (As_4 vs As_2, Sb_4 vs Sb_2) by changing the temperature. During daily operation, the flux of these materials is controlled by opening and closing the cracking zone to different valve positions. In front of each of these effusion cells is a pneumatic shutter which can block the escaping flux when deactivated.

The rate of these fluxes is determined by beam flux monitor (BFM) and reflection high energy electron diffraction (RHEED) measurements. The BFM is an ion gauge that

can be positioned in front of the flux escaping the effusion cell. The ion gauge translates the flux of a given material into a background pressure which is directly related to a specific deposition rate. BFM measurements are a quick and consistent method of measuring flux ratios of two different materials and is especially useful for V/III ratios in nanowire growths. RHEED measurements utilize an electron gun and phosphor coated screen. The electron gun is positioned so an electron beam glances off the sample at a very narrow angle before hitting the phosphor screen. An illuminated pattern is formed from the phosphor-electron interaction. The electron gun only interacts with the surface of the sample, and produces a diffraction pattern based on the surface structure. A highly ordered film produces streaks whereas a disordered film produces spots, rings, or nothing at all. During crystal growth, the pattern will oscillate in intensity. A single oscillation corresponds to the growth of a monolayer of material and can be used to calculate a rate. RHEED measurements are especially useful for growths requiring precise deposition such as GaSb quantum dots.[41]

Stranski-Krastanov Growth

There are a variety of specialized growth techniques utilized in this work to create desired nanostructures. On such technique is the Stranski-Krastanov (SK) growth method. SK growth is actually one of the three primary growth modes for epitaxial thin film heterostructures, the other two being Frank-van der Merwe and Volmer-Weber growth.[42] SK growth mode is used in this work to create GaSb quantum dots.

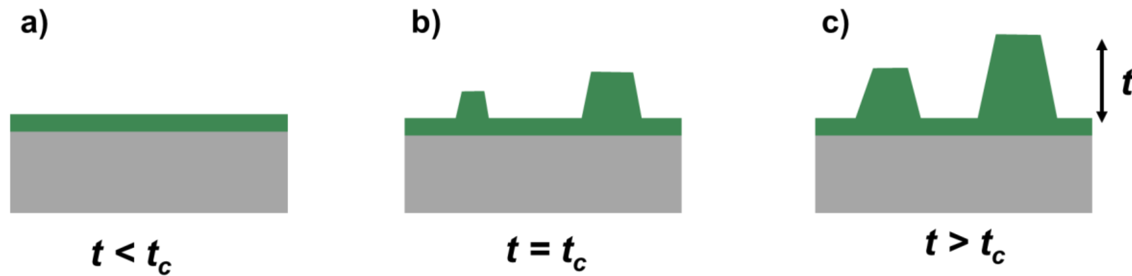

Figure 1.8: Schematic detailing the a) epitaxial b) critical thickness and c) island growth stages in the Stranski-Krastanov growth mode.

Figure 1.8 is a schematic detailing SK growth. During SK growth, the group III and group V materials are deposited on the substrate simultaneously. This process is strain dependent and requires that the depositing material is not lattice matched to the substrate. In this work the group III and group V materials are Ga and Sb respectively, and the substrate is GaAs. Initially a smooth thin film begins to grow (**Fig. 1.8a**). As more material is deposited, the lattice mismatch between the two materials causes strain to build within the film. At some critical thickness, islands form on the surface to compensate for the strain (**Fig. 1.8b**). Further deposition results in subsequent island growth and additional island formation (**Fig. 1.8c**). To create quantum dots, the growth is interrupted near the critical thickness so the resulting islands have the desired quantum dot dimensions. The critical thickness for dot nucleation is dependent on parameters such as the lattice mismatch, temperature, and growth rate.[43] The thin epitaxial film formed during the initial stages of SK growth is not wholly removed during island formation and is known as the wetting layer.

Droplet Epitaxy Growth

Droplet Epitaxy (DE) is another growth technique used to create GaSb quantum dots.[44] **Figure 1.9** is a schematic detailing DE quantum dot growth. During DE growth,

the group III and group V materials are deposited on the substrate in stages. This method is not strain driven and does not require a lattice mismatch between the depositing materials and the substrate. In this work the group III and group V materials are Ga and Sb respectively, and the substrate is GaAs. Initially, just the liquid group III material is deposited on the substrate. As a result, the liquid forms droplets on the substrate (**Fig. 1.9a**). Group III deposition is then terminated, and the droplets are introduced to a group V flux (**Fig. 1.9b**). When the group V flux comes in contact with the group III droplets, the droplets crystallize into a III-V quantum dot (**Fig. 1.9c**). There are many different growth parameters that can be controlled during DE, such as the substrate temperature, the group V deposition rate, and deposition time. By changing these parameters, nanostructures of varying morphologies can be created.

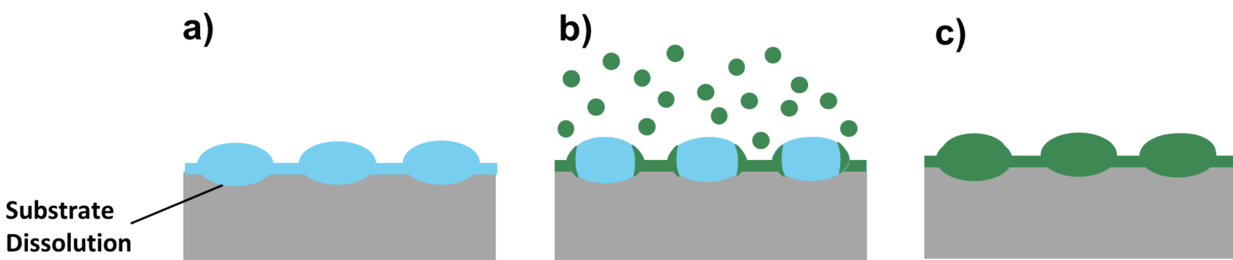

Figure 1.9: Schematic showing the a) group III droplet formation, b) group V introduction and initial crystallization, and c) final crystallization stages of the droplet epitaxy growth method.

Vapor-Liquid-Solid Growth

The Vapor-Liquid-Solid (VLS) mechanism is a growth technique used to create GaAs nanowires.[45] **Figure 1.10** is a schematic detailing VLS nanowire growth. During VLS growth, a liquid droplet is used as a catalyst for crystal growth. Initially the liquid forms a droplet on the solid substrate (**Fig. 1.10a**). When a vapor is introduced, such as

Ga and As during MBE growth, the vapor elements dissolve into the catalyst (**Fig. 1.10b**). These solutes then preferentially crystallize at the liquid-solid interface (**Fig. 1.10c**). During this process there can still be epitaxial growth in regions without a catalyst. As long as the crystallization at this liquid-solid interface within the catalyst is faster than the epitaxial growth in regions without a catalyst, nanowires form. The size of the catalyst determines the initial diameter of the nanowire. The VLS mechanism is often used in epitaxial growth of semiconductor nanowires in vapor deposition chambers.[46]

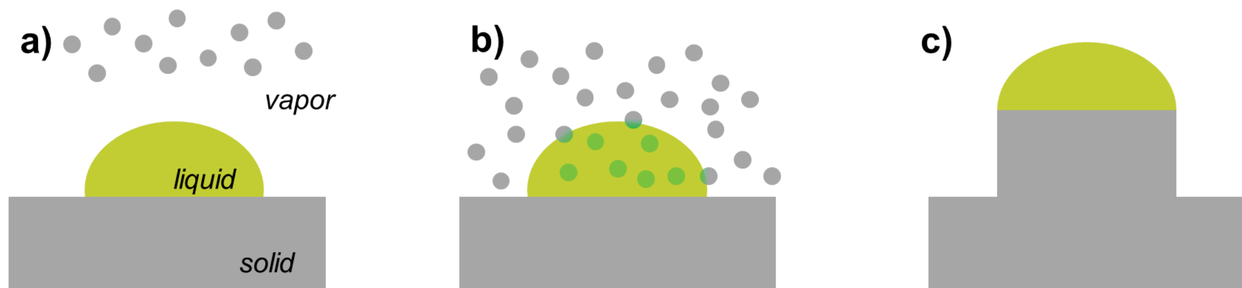

Figure 10: Schematic illustrating the stages of VLS gowth: a) droplet formation, b) vapor dissolution, and c) nanowire formation.

1.4.2 Scanning Probe Microscopy

Atomic Force Microscopy

Atomic force microscopy (AFM) is a form of scanning probe microscopy that can measures a sample by applying a force through a mechanical probe as it is scanned across the surface. The mechanical probe consists of a sharp tip attached to a piezoelectric modulator by a cantilever. AFM is used extensively in the first section of this work to analyze the size, shape, and distribution of GaSb quanum dots on GaAs surfaces. AFM's can be used for a variety of measurements including but not limited to force measurements, imaging, and electrical characterization. For the purposes of his work we

solely use an AFM for imaging. To image the quantum dots the AFM is put in tapping mode. In this mode the piezoelectric modulator oscillates the cantilever causing the probe tip to contact the surface at some constant frequency. As the tip is scanned across the sample, the cantilever will change in amplitude based on features present on the surface. This change in amplitude is measured by a laser that reflects off the end of the cantilever into a four-quadrant photodetector. From this information a three dimensional topographical image of the surface can be generated.

Cross-Sectional Scanning Tunneling Microscopy

Cross-sectional scanning tunneling microscopy (XSTM), and more generally scanning tunneling microscopy (STM), is a form of scanning probe microscopy that measures a sample by analyzing the electrical characteristics of a surface when scanning a conducting tip across the surface. XSTM is used to measure the morphology and crystal structure of GaSb quantum dots and their respective capping layers. This technique requires vacuum conditions to operate. It has atomic resolution and is based on the principles of quantum tunneling. When the tip is brought near the surface of a sample, a bias can be applied to allow electrons to tunnel through the vacuum between the tip and the sample. During a scan, either the bias or tunneling current can be kept constant while other parameter is recorded. Differences in local density of states, material composition, and distance between the tip and the surface, can influence the measurement. The measurement differences across the sample are often portrayed as contrast differences within images. For example, the GaSb material has a much different contrast then the GaAs material in quantum dot measurements. XSTM functions in a similar manner to STM except a cleaved cross-section of the sample is measured instead of the exposed

surface. I thank my collaborator Dr. Erwin Smakman and his advisor Professor Paul Koenraad at the Eindhoven University of Technology for collecting the XSTM measurements present in this work.

1.4.3 Electron Microscopy

Scanning Electron Microscopy

Scanning electron microscopy (SEM) is a form of electron microscopy that produces an image by scanning an electron beam across the sample surface. SEM is used extensively in this work, primarily for the analysis of GaAs nanowires. An SEM works by subjecting a sample to an electron beam and measuring the response using a variety of detectors. An electron beam is initially produced by passing current through a pointed filament. To focus the beam on the sample, the electrons pass through a series of magnetic lenses. When electrons interact with the sample they can produce secondary electrons, backscattered electrons, and characteristic x-rays. Secondary electrons only come from the surface layers of the material and can be used for topographical measurements. Backscattered electrons scatter based on the atomic number of a material and contain compositional information. Characteristic X-rays can be used for compositional information as well. The majority of SEM measurements presented in this work are images from secondary electrons to measure nanowire features from various growth conditions.

Transmission Electron Microscopy

Transmission electron microscopy (SEM) is a form of electronn microscopy that produces an image by transmitting electrons through sample. TEM is used for both GaSb quantum dots and GaAs nanowires to analyze crystal structure and defects in the various growths. A TEM works by positioning a sample in between an electron beam and a detector. In order for the electron beam to pass through the sample, it is necessary to make the sample ultra-thin, otherwise the electrons will be lost through scattering events. Multiple magnetic lenses are used to focus both the primary and transmitted electron beam. An image of the sample can be obtained from the transmitted beam. By changing the focus, information on the sample's crystal structure can be obtained via the image diffraction patterns. Both bright field and dark field images are used in this work. Bright field images are produced from the direct beam and can contains information on the morphology and crystallinity of a nanostructure. Dark field images are produced from scattered electrons and can provide more specific information on a specific crystal plane, defects or atomic composition. Another TEM technique, electron energy loss spectroscopy (EELS), is used in this work. EELS involves measuring the inelastic scattering of electrons interacting with the sample to obtain elemental characterization. I thank my collaborator Lifan Yan, a PhD candidate in Professor Millunnchick's group, who collected the TEM measurements present in this work.

1.4.4 Photoluminescence

Photoluminescence measurements (PL) are a form of optical spectroscopy that measures light emission from a sample after using photons to excite carriers within the material. PL is used to measure the optical emission of both GaSb quantum dots and GaAs nanowires in Parts 1 and 2. PL is a process in which high energy photons from a laser are focused on a sample and excites electrons from the valence band to the conduction band. These excited electrons then combine with the holes in the valence band. Since the valence band is at a lower energy state, the energy is released in the form of radiation. The energy of the photon is equal to the energy bandgap. Electrons excited to energies higher than the conduction band do not emit at higher energies, and instead lose energy in the form of heat until reaching the conduction band. This process is known as thermalization.[ref] Parameters such as laser wavelength, intensity, spot size, sample temperature can be controlled using various equipment to enhance the PL response of a sample. I thank my collaborators, PhD candidate Marta Luengo-Kovac and her advisor Professor Vanessa Sih at the University of Michigan for aiding me in the PL measurements presented in this work.

1.4.5 Atom Probe Tomography

Atom Probe Tomography (APT) is a material analysis technique that is useful for 3D imaging and compositional measurements on the atomic scale. APT is used to measure the compositional features of GaSb quantum dots. Samples for APT are prepared by milling the sample into a very sharp tip. The tip is biased with a high voltage causing an electrostatic field to form around the end of the tip. By pulsing the tip with a laser or high voltage, atoms near the tip can become ionized and are evaporated from the surface. These atoms are then projected onto a position sensitive detector which can

measure values such as time of flight from the tip to the detector, the mass to charge ratio, and X-Y position on the detector. From this data a 3D reconstruction of the tip with atomic elemental information can be generated. I thank PhD candidate Lifan Yan who collected the APT data presented in this work.

1.4.6 Kinetic Monte Carlo Simulations

Kinetic Monte Carlo (KMC) is a computer simulation based on the Monte Carlo method. KMC simulations are used to corroborate proposed GaSb quantum dot growth methods and is compared with experimental results. The Monte Carlo method is a class of computing algorithms that uses random sampling to solve problems that are difficult to approach. In KMC there is a time evolution component and is typically focused on observing the transition of a system from its initial state to its final state. The KMC simulations used in this work are from software developed by Professor Peter Smereka and Dr. Kris Reyes from the Math Department at the University of Michigan. The simulation can be used to emulate the random nature of vapor deposition. The simulation starts with a substrate of fixed parameters built by stacking atoms on top of each other. In this work that substrate is GaAs. Next, vapor deposition is emulated by adding additional elements to the surface. These atoms are allowed to diffuse and crystallize. Parameters such as deposition rate, temperature, time, and binding energies can be modified to observe different crystallization reactions. I thank Dr. Kris Reyes and Professor Peter Smereka from the University of Michigan Math department for performing the KMC simulations presented in this work.

1.5 References

1. Tolochko, N. K. (2009). History of nanotechnology. *Nanoscience and nanotechnologies. Encyclopaedia of Life Support Systems (EOLSS), Developed under the auspices of the UNESCO, Eolss Publishers, Oxford.*
2. Malanowski, N., Heimer, T., Luther, W., & Werner, M. (Eds.). (2008). *Growth market nanotechnology: an analysis of technology and innovation*. John Wiley & Sons.
3. Roco, M. C. (2011). The long view of nanotechnology development: the National Nanotechnology Initiative at 10 years. *Journal of Nanoparticle Research*, *13*(2), 427-445.
4. Fulekar, M. H. (2010). *Nanotechnology: importance and applications*. IK International Pvt Ltd.
5. Harrison, P., & Valavanis, A. (2016). *Quantum wells, wires and dots: theoretical and computational physics of semiconductor nanostructures*. John Wiley & Sons.
6. Tsakalakos, L. (2010). *Nanotechnology for photovoltaics*. CRC press.
7. Bao, J., Zimmler, M. A., Capasso, F., Wang, X., & Ren, Z. F. (2006). Broadband ZnO single-nanowire light-emitting diode. *Nano letters*, *6*(8), 1719-1722.
8. Chau, R., Datta, S., Doczy, M., Doyle, B., Jin, B., Kavalieros, J., ... & Radosavljevic, M. (2005). Benchmarking nanotechnology for high-performance and low-power logic transistor applications. *IEEE Transactions on Nanotechnology*, *4*(2), 153-158.
9. Santori, C., Barclay, P. E., Fu, K. C., Beausoleil, R. G., Spillane, S., & Fisch, M. (2010). Nanophotonics for quantum optics using nitrogen-vacancy centers in diamond. *Nanotechnology*, *21*(27), 274008.

10. McAlpine, Michael C., Habib Ahmad, Dunwei Wang, and James R. Heath. "Highly ordered nanowire arrays on plastic substrates for ultrasensitive flexible chemical sensors." *Nature materials* 6, no. 5 (2007): 379-384.
11. Cui, Y., Wei, Q., Park, H., & Lieber, C. M. (2001). Nanowire nanosensors for highly sensitive and selective detection of biological and chemical species. *Science*, *293*(5533), 1289-1292.
12. Smakman, E. P., Garleff, J. K., Young, R. J., Hayne, M., Rambabu, P., & Koenraad, P. M. (2012). GaSb/GaAs quantum dot formation and demolition studied with cross-sectional scanning tunneling microscopy. *Applied Physics Letters*, *100*(14), 142116.
13. Callister, W. D., & Rethwisch, D. G. (2007). *Materials science and engineering: an introduction* (Vol. 7, pp. 665-715). New York: Wiley.
14. Borovitskaya, E., & Shur, M. S. (Eds.). (2002). *Quantum dots* (Vol. 25). World Scientific.
15. Kalt, H. (2012). *Optical Properties of III–V Semiconductors: The Influence of Multi-Valley Band Structures* (Vol. 120). Springer Science & Business Media.
16. Rohlfing, M., Krüger, P., & Pollmann, J. (1993). Quasiparticle band-structure calculations for C, Si, Ge, GaAs, and SiC using Gaussian-orbital basis sets. *Physical Review B*, *48*(24), 17791.
17. Green, M. A., Emery, K., Hishikawa, Y., Warta, W., & Dunlop, E. D. (2015). Solar cell efficiency tables (Version 45). *Progress in photovoltaics: research and applications*, *23*(1), 1-9.
18. Hall, R. N., Fenner, G. E., Kingsley, J. D., Soltys, T. J., & Carlson, R. O. (1962). Coherent light emission from GaAs junctions. *Physical Review Letters*, *9*(9), 366.

19. McEvoy, A. J., Castaner, L., & Markvart, T. (2012). *Solar cells: materials, manufacture and operation*. Academic Press.

20. Dutta, P. S., Bhat, H. L., & Kumar, V. (1997). The physics and technology of gallium antimonide: An emerging optoelectronic material. *Journal of Applied Physics*, *81*(9), 5821-5870.

21. Wei, Y., Gin, A., Razeghi, M., & Brown, G. J. (2002). Advanced InAs/GaSb superlattice photovoltaic detectors for very long wavelength infrared applications. *Applied physics letters*, *80*(18), 3262-3264.

22. Fraas, L. M., Daniels, W. E., & Muhs, J. (2001, October). Infrared photovoltaics for combined solar lighting and electricity for buildings. In *Proceedings of 17th European Photovoltaic Solar Energy Conference*.

23. Laghumavarapu, R. B., Moscho, A., Khoshakhlagh, A., El-Emawy, M., Lester, L. F., & Huffaker, D. L. (2007). GaSb∕GaAs type II quantum dot solar cells for enhanced infrared spectral response. *Applied Physics Letters*, *90*(17), 173125.

24. Pierret, R. F. (1996). *Semiconductor device fundamentals*. Pearson Education India.

25. Kim, D. M. (2010). *Introductory quantum mechanics for semiconductor nanotechnology*. Wiley-VCH.

26. Notomi, M., Hammersberg, J., Weman, H., Nojima, S., Sugiura, H., Okamoto, M., ... & Potemski, M. (1995). Dimensionality effects on strain and quantum confinement in lattice-mismatched InAs x P 1− x/InP quantum wires. *Physical Review B*, *52*(15), 11147.

27. Mitin, V. V., Sementsov, D. I., & Vagidov, N. Z. (2010). *Quantum Mechanics for nanostructures*. Cambridge University Press.

28. Nagahama, S. I., Iwasa, N., Senoh, M., Matsushita, T., Sugimoto, Y., Kiyoku, H., ... & Chocho, K. (2000). High-power and long-lifetime InGaN multi-quantum-well laser diodes grown on low-dislocation-density GaN substrates. *Japanese Journal of Applied Physics*, *39*(7A), L647.
29. Kuzmík, J. (2002). InAlN/(In) GaN high electron mobility transistors: some aspects of the quantum well heterostructure proposal. *Semiconductor Science and Technology*, *17*(6), 540.
30. Hersee, S. D., Sun, X., & Wang, X. (2006). The controlled growth of GaN nanowires. *Nano letters*, *6*(8), 1808-1811.
31. Patolsky, F., Timko, B. P., Yu, G., Fang, Y., Greytak, A. B., Zheng, G., & Lieber, C. M. (2006). Detection, stimulation, and inhibition of neuronal signals with high-density nanowire transistor arrays. *Science*, *313*(5790), 1100-1104.
32. Choi, J. W., Cui, Y., & Nix, W. D. (2011). Size-dependent fracture of Si nanowire battery anodes. *Journal of the Mechanics and Physics of Solids*, *59*(9), 1717-1730.
33. Garnett, E., & Yang, P. (2010). Light trapping in silicon nanowire solar cells. *Nano letters*, *10*(3), 1082-1087.
34. Wang, Z. M. (Ed.). (2012). *Quantum dot devices* (Vol. 13). Springer Science & Business Media.
35. Konstantatos, G., & Sargent, E. H. (Eds.). (2013). *Colloidal quantum dot optoelectronics and photovoltaics*. Cambridge University Press.
36. Ishikuro, H., & Hiramoto, T. (1997). Quantum mechanical effects in the silicon quantum dot in a single-electron transistor. *Applied Physics Letters*, *71*(25), 3691-3693.

37. Brock, S. L. (2004). Nanostructures and Nanomaterials: Synthesis, Properties and Applications By Guozhang Cao (University of Washington). Imperial College Press (distributed by World Scientific): London. 2004. xiv+ 434 pp. $78.00. ISBN 1-86094-415-9. *Journal of the American Chemical Society*, *126*(44), 14679-14679.

38. Mitchell, B. S. (2004). *An introduction to materials engineering and science for chemical and materials engineers*. John Wiley & Sons.

39. Hoffman, D., Singh, B., & Thomas III, J. H. (1997). *Handbook of vacuum science and technology*. Academic Press.

40. Henini, M. (Ed.). (2012). *Molecular beam epitaxy: from research to mass production*. Newnes.

41. Neave, J. H., Joyce, B. A., Dobson, P. J., & Norton, N. (1983). Dynamics of film growth of GaAs by MBE from RHEED observations. *Applied Physics A*, *31*(1), 1-8.

42. Ayers, J. E. (2007). *Heteroepitaxy of semiconductors: theory, growth, and characterization*. CRC press.

43. Baskaran, A., & Smereka, P. (2012). Mechanisms of Stranski-Krastanov growth. *Journal of Applied Physics*, *111*(4), 044321.

44. Watanabe, K., Koguchi, N., & Gotoh, Y. (2000). Fabrication of GaAs quantum dots by modified droplet epitaxy. *Japanese Journal of Applied Physics*, *39*(2A), L79.

45. Wagner, R. S., & Ellis, W. C. (1964). Vapor-liquid-solid mechanism of single crystal growth. *Applied Physics Letters*, *4*(5), 89-90.

46. Harmand, J. C., Patriarche, G., Péré-Laperne, N., Merat-Combes, M. N., Travers, L., & Glas, F. (2005). Analysis of vapor-liquid-solid mechanism in Au-assisted GaAs nanowire growth. *Applied Physics Letters*, *87*(20), 203101.

Chapter 2
Capping Chemistry in GaSb/GaAs Quantum Dots

This chapter investigates the effects of $Al_xGa_{1-x}As$ capping layers on the morphological, structural, and optical characteristics of GaSb quantum dots grown on GaAs substrates. The Al acts as a diffusion barrier to the Sb that migrates from the quantum dots during capping. The samples are analyzed with cross-sectional scanning tunneling microscopy (XSTM) and photoluminescence. Samples containing Al compounds in the wetting layer exhibited a reduction in quantum dot demolition and an increase in the average quantum dot height. However, in the absence of quantum dot demolition, strain accumulated around the quantum dots causing defects to form. Photoluminescence measurements showed a minor blue shift in the wetting layer emission, but no shift in the quantum dot emission. It is proposed that the larger dots are too heavily defected to contribute to the photoluminescence emission.

2.1 Introduction

GaSb/GaAs quantum dots and their type II band alignment are of interest for a number of semiconductor device applications including intermediate band photovoltaics and charge based memory. Recently it has been demonstrated that their morphology, structure, composition, and optical properties change significantly when capped.[1-5] The lattice mismatch between the capping layer and the quantum dot creates a high local strain field which induces lateral out diffusion of Sb away from the quantum dot core.[6] As a result, some percentage of the embedded quantum dots demolish into rings and clusters of islands. This creates a non-uniform distribution of nanostructures within the structure, which could lead to band broadening. This work attempts to reduce quantum dot demolition by preventing the Sb out-diffusion which occurs during capping. To do this Aluminum is introduced into the GaAs capping layer. Compared to Ga, Al containing compounds generally have higher stronger bond strengths and thus lower surface diffusion rates. AlAs also nominally shares the same lattice parameter as GaAs, so introducing it into the capping layer does not add any additional strain to the system. Al-rich capping of GaSb/GaAs quantum dots has also shown to increase the hole localization energy which is useful for flash memory applications[10,11] as a larger localization energy corresponds to longer lifetimes.[14] The quantum dots are coupled to a 2D hole gas and allows for very fast read and write times.[12,13] Due to the type II band alignment in GaSb/GaAs quantum dots also make them very interesting candidates for intermediate band solar cells.[7-9] In this work, GaSb/GaAs quantum dot are grown with Al-containing capping layers. The quantum dots are measured structurally using cross-sectional scanning tunneling microscopy (XSTM) and optically with photoluminescence (PL).

2.2 Experimental Methods

The quantum dots are grown using a solid-source molecular beam epitaxy chamber on GaAs (100) substrates. The method used to create the quantum dots is known as the Stranski-Krastanov growth mechanism.[ref] SK growth is a strain driven approach in which quantum dots form after a certain critical thickness of lattice mismatched material is deposited. In this case, GaSb deposited on GaAs. Prior to quantum dot growth an undoped 500nm GaAs buffer layer is grown at 1.0 monolayers per second (ML/s) at T_s=580°C. For quantum dot growth the samples were cooled to T_s=460°C and 2.3ML of GaSb were deposited at a Ga rate of r_{Ga}=0.3ML/s with a concurrent Sb flux of BEP_{Sb}=8x10^{-7} Torr. Uncapped quantum dots were measured using atomic force microscopy. The original uncapped quantum dots were 4±1nm tall with a density of 5x10^{10}cm^{-2}.

Immediately after quantum dot growth the capping layer was deposited. The capping layer consisted of either 50nm of GaAs, 1ML of AlAs with 50nm of GaAs, 3ML of AlAs with 50nm of GaAs, or 20nm of $Al_{0.5}Ga_{0.5}As$ with 30nm of GaAs. The capping layers were also grown at a rate of r_{Ga}=0.3 ML/s with an As flux of BEP_{As}=6x10^{-6} Torr with the exception of the $Al_{0.5}Ga_{0.5}As$ layer which was grown at r_{Ga}=0.6ML/s. Afterwards the sample was annealed for 10 minutes and quenched.

For XSTM, one sample was grown and consisted of seven quantum dot layers: one layer with GaAs capping for the control, and two layers of each Al-containing layer. The samples were cleaved under ultra-high vacuum to reveal {110} surfaces. An Omicron LT-STM was used and operated at a pressure of $p \leq 3x10^{-11}$ Torr and a temperature of 77K. For PL, four different samples were grown. Each sample had ten layers of quantum dots of a single capping chemistry.

2.3 Data Analysis

2.3.1 $Al_xGa_{1-}As$ Capping of GaSb Quantum Dots

Figure 2.1 shows topographical images of GaSb nanostructures measured by XSTM. In **Fig. 2.1a-e** features can be distinguished from the yellow-orange contrast. At the chosen tunneling conditions, the STM was primarily imaging the filled states of the group V elements. As such, the contrast is attributed to the differences in the local dangling bonds of As and Sb. The lighter contrast in **Fig. 2.1** corresponds to Sb. Even though we use two different group III atoms (Ga and Al) we do not expect them to influence the contrast. **Figure 2.1a** is an example of a disintegrated quantum dot capped with GaAs. The shape is distorted and shows evidence of potential Sb out-diffusion. At the base of the quantum dot there is a horizontal contrast line that corresponds to the GaSb wetting layer. This wetting layer is present in all quantum dot measurements and is a necessary product of Stranski-Krastanov growth. Near the bottom interface of the quantum dot, there are some dark shapes present in the image. These are from cleaving artifacts and originate form material that was ripped out or left behind when cleaved. This is caused from the built up strain of the quantum dots and surrounding GaAs. When cleaved, the quantum dots can relax and this can result in these cleaving defects. Cleaving defects can also be seen in **Fig. 2.1b, c,** and **e. Figure 2.1b** is an example of an intact quantum dot capped with 1ML of AlAs. The quantum dot is hemispheric in shape and a the bright contrast at the interface is a piece of Sb material projected out of plane during cleaving. **Figure 2.1c** is an example of an intact quantum dot capped with 3ML of

AlAs. Compared to **Fig. 2.1b** this quantum dot is much more pyramidal in shape. Cleaving defects can be seen throughout the quantum dot. **Figure 2.1d** is an example of a disintegrated quantum dot capped with 50nm of $Al_{0.5}Ga_{0.5}As$. This quantum dot demolished during capping, forming a ring or separate islands.

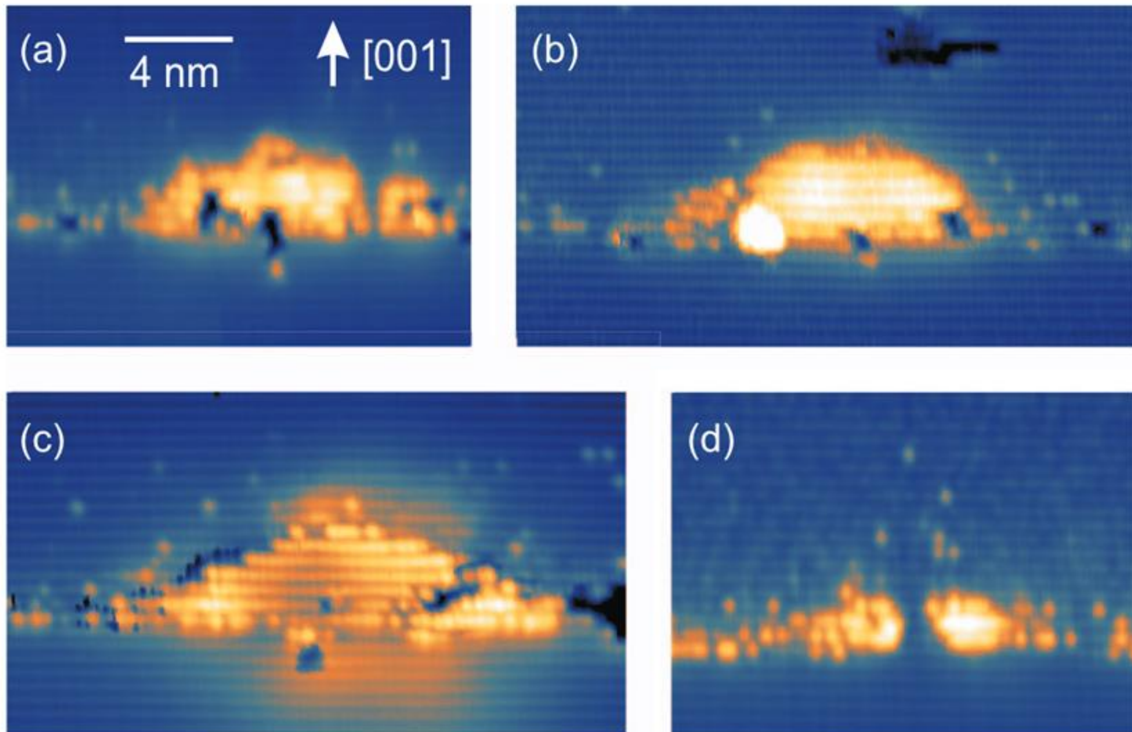

Figure 2.1: Select XSTM images of GaSb quantum dots capped with a) GaAs, b) 1ML AlAs, c) 3ML AlAs, and d) 20nm of $Al_{0.5}Ga_{0.5}As$

Intact and demolished quantum dots are present in all four samples. Intact quantum dots retain the truncated pyramidal and spherical shape of the original quantum dots (**Fig. 2.1b** and **Fig. 2.1c**). Demolished quantum dots and can either appear as deformed quantum dots (**Fig. 2.1a**) or segmented structures (**Fig. 2.1d**). For GaSb quantum dots, there is little to no intermixing with the surrounding GaAs. This is clear from the absence of alloy fluctuations in the XSTM images (**Fig. 2.1**). The contrast edges

of the quantum dots are very sharp and suggest pure Sb nanostructures. This is unlike other quantum dot systems such as InAs/GaAs quantum dots in which intermixing plays a key role in alleviating the strain.[15,16]

2.3.2 Defect Formation under Aluminum Capping

In addition to measuring the group V distribution, the XSTM measured the presence of defects in the capping layer around several of the quantum dots. **Figure 2.2** shows XSTM images of defected quantum dots. **Figure 2.2a** shows topographical and current images of a quantum dot capped with 1ML of AlAs. In the topographical image there is a heavy black region in the capping layer directly above the quantum dot. In the adjacent image produced from the current measurements, a very clear break in the crystal structure is visible in the capping layer on the right side above the quantum dot.

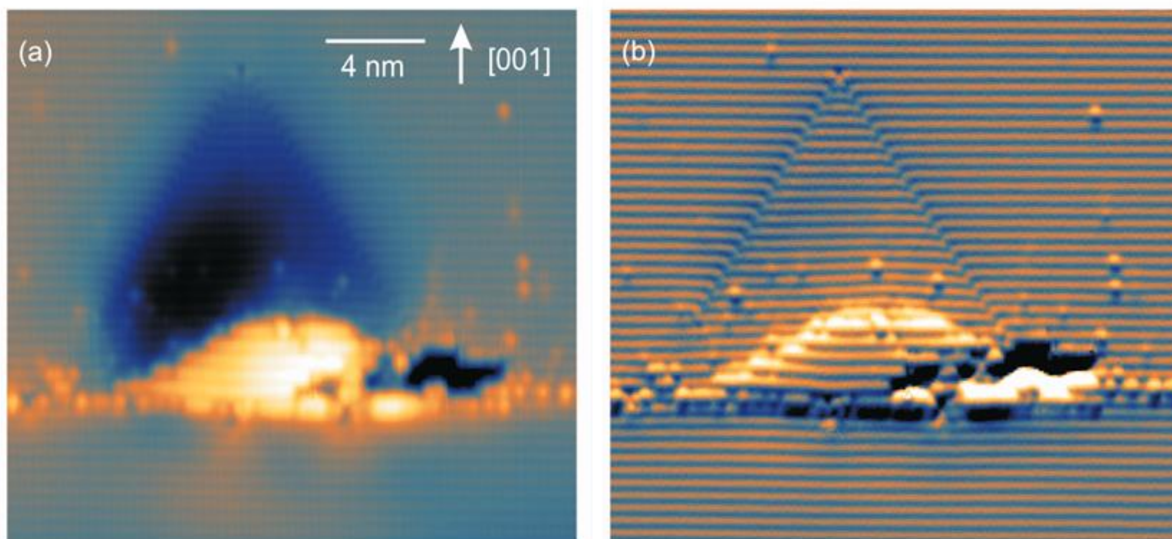

Figure 2.2: a) Topographical and b) Current XSTM images of a defected GaSb quantum dot capped with $Al_{0.6}Ga_{0.5}As$

This dislocation extends from the edge of the quantum dot and extends upwards before either annihilating or going out of plane. **Figure 2.2b** shows topographical and current images of a quantum dot capped with 20nm of $Al_{0.5}Ga_{0.5}As$. Similar to **Fig. 2.2a** there is a black contrast region in the capping layer directly above the quantum dot in the topographical image. From the current image it is clear that this contrast arises from two dislocations. These dislocations originate at the edges of the sides of the quantum dot and propagate in the growth direction. The interruption in the lattice parameter caused by these dislocations is clearly visible near the point at which the dislocations contact each other and annihilate. The area above the quantum dot is relaxed inward compared to the surrounding capping layer and suggests tensile strain in that region.

Figure 2.3 is an atomic model of the (110) plane of the GaSb/GaAs quantum dot and depicts the defect present in **Fig. 2.2b**. The larger dots are represent the atoms in the surface accessible to the XSTM tip. The smaller dots represent atoms 1ML below the larger dots in the in-plane direction. The dotted lines represent the defects and extend in the <111> direction. In this model it is proposed that there are several defects present at the GaSb-GaAs substrate interface. This is consistent with multiple reports that demonstrate that these misfit dislocations can occur during GaSb quantum dot growth.[17,18] Due to the misfit dislocations and local strain, capping layer deposition in the immediate vicinity of the quantum dot does not grow in perfect registry. As a result the capping layer material deposited directly on top of the GaSb quantum dot may be

displaced by 1ML with the surrounding capping layer, creating a stacking fault.[19] This is visualized in the model in **Fig. 2.3.** These stacking faults may terminate in a defect or when meeting another stacking fault.

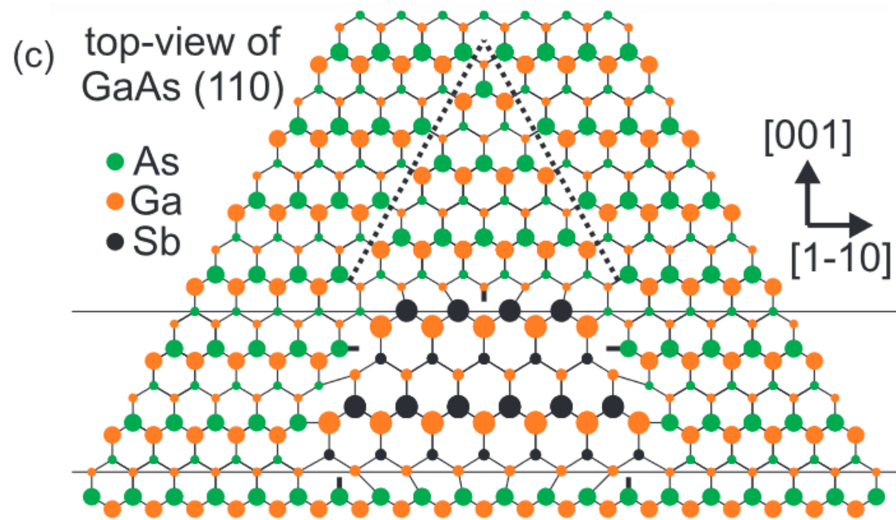

Figure 2.3: Ball-and-stick model of defects form in GaAs capping layer surrounding a GaSb quantum dot.

2.3.3 Statistical analysis of capped quantum dots

In this work 389 quantum dots were analyzed from XSTM measurements across the seven different layers. Their size and morphology were recorded and compared against the different capping chemistries. **Figure 2.4** shows the quantum dot height distribution in each of these layers. In addition to measuring the height, each quantum dot is classified as either intact or disintegrated. To be considered disintegrated at least 10% of the quantum dot shape must have been impacted by capping. Also included is the percentage of intact dots that are defected. Due to the 2D nature of XSTM measurements, it is estimated that there is a 10% error in the statistical analysis. **Figure 2.4a** shows the statistical measurements of GaAs capped quantum dots. The average

quantum dot height is 3.1nm and 52% (11%) of the quantum dots were intact (defected). **Figure 2.4b** shows the statistics of quantum dots capped with 1ML of AlAs. The average quantum dot height is 4.5nm and 70% (9%) of the quantum dots were intact (defected). **Figure 2.4c** shows the statistics of quantum dots capped with 3ML of AlAs. The average quantum dot height is 4.5nm and 79% (17%) of the quantum dots were intact (defected). **Figure 2.4d** shows the statistics of quantum dots capped with 20nm of $Al_{0.5}Ga_{0.5}As$. The average quantum dot height is 4.5nm and 83% (22%) of the quantum dots were intact (defected).

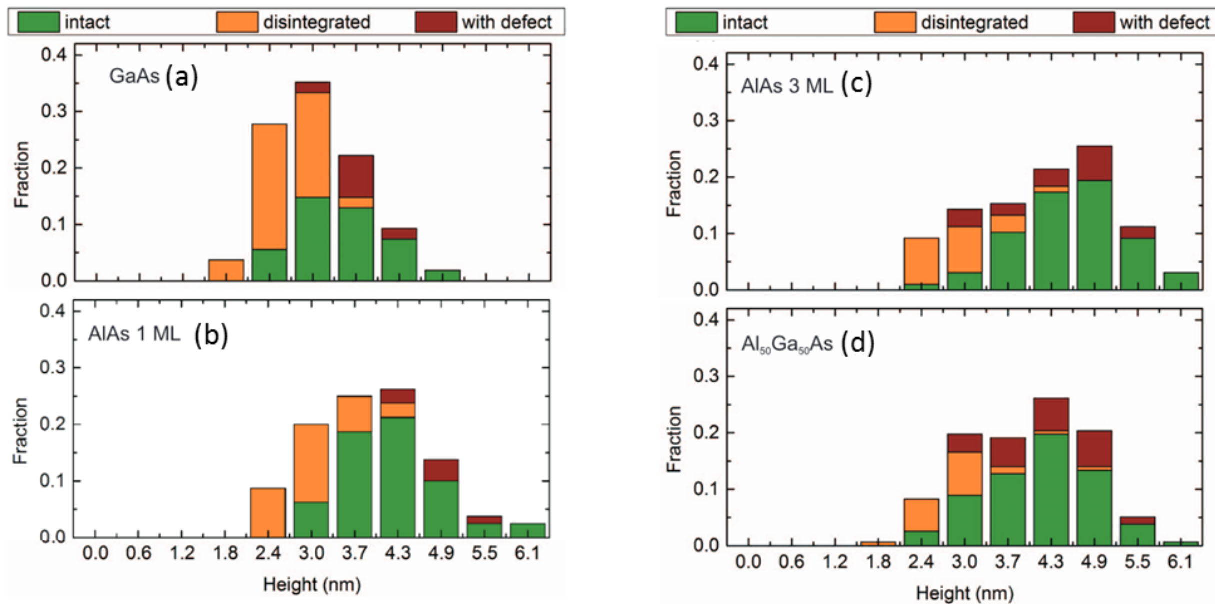

Figure 2.4: Bar graphs detailing the fraction of measurements vs. quantum dot height in a) GaAs, b) 1ML AlAs, c) 3ML AlAs, and d) $Al_{0.5}Ga_{0.5}As$ samples that are intact, disintegrated, and defected

From the statistical measurements of the XSTM quantum dots, it is observed that the percentage of quantum dots that remain intact increase when capped with Al-compounds, from 52% in the GaAs control to 70-83% with Al-compounds. During GaAs capping, Sb is known to diffuse laterally from the GaSb quantum dot. The nonsymmetrical

outline of the quantum dot in **Fig 2.1a** is a result of this out-diffusion. Al is much more resistant to diffusion than Ga, and prevents the migration of Sb. As a result, more quantum dots remain intact. Another observation from the statistical measurements is that the average quantum dot height increases from 3.1nm in the control to 4.5nm in the samples capped with Al-compounds. This is also consistent with a reduction in Sb out-diffusion. The 4.5nm height of the quantum dots in the Al-capped samples is consistent with the uncapped AFM height measurements. The increase in percentage of intact quantum dots in addition to the increase in quantum dot height suggests that the presence of Al in the capping layer preserves the original uncapped quantum dot structure.

The statistical measurements of the XSTM quantum dots also reveal an increase in defects in the Al-compound samples. In the GaAs control, 11% of the quantum dots were surrounded with defects, while 9%, 17%, and 22% of the quantum dots capped with 1ML AlAs, 3ML AlAs and 20nm $Al_{0.5}Ga_{0.5}As$ respectively, were surrounded with defects. During quantum dot capping, the lattice mismatch between the quantum dot and the capping layer introduces a significant amount of local strain. To reduce this strain, Sb diffuses away from the quantum dot core. This is responsible for the quantum dot demolition present in **Fig 2.1a** and **Fig 2.1d**. In the Al-rich samples, the Al prevents the Sb out-diffusion and in order to compensate for the local strain defects form in the surrounding capping layer.

2.3.4 Photoluminescence of $Al_xGa_{1-x}As$ capped GaSb Quantum Dots

Figure 2.5 shows the PL measurements of the four GaSb quantum dot samples. The samples were cooled to T=10K and measured using a Coherent Ti:Sapph tunable laser at λ=845nm with a spot size of 5μm. An 850nm filter was placed in the path of the

collection beam, between the sample and an InGaAs detector. At 845nm, excitation was isolated below the bandgap of the GaAs substrate material. The emission is normalized to better compare relative peak positions and emission. In each profile there are two clear excitation peaks. The higher energy peak corresponds to emission from the wetting layer and the lower energy peaks corresponds to emission from the quantum dots. The wetting layer peak position in the GaAs, 1ML AlAs, 3ML AlAs, and 20nm $Al_{0.5}Ga_{0.5}As$ are 1.32, 1.35, 1.35, and 1.36 respectively. The quantum dot peak position is 1.16eV in all samples. Absolute emission was strongest in the $Al_{0.5}Ga_{0.5}As$ sample and weakest in the 1ML AlAs sample. The quantum dot/wetting layer emission ratio was also the highest and lowest in the $Al_{0.5}Ga_{0.5}As$ and 1ML AlAs samples respectively.

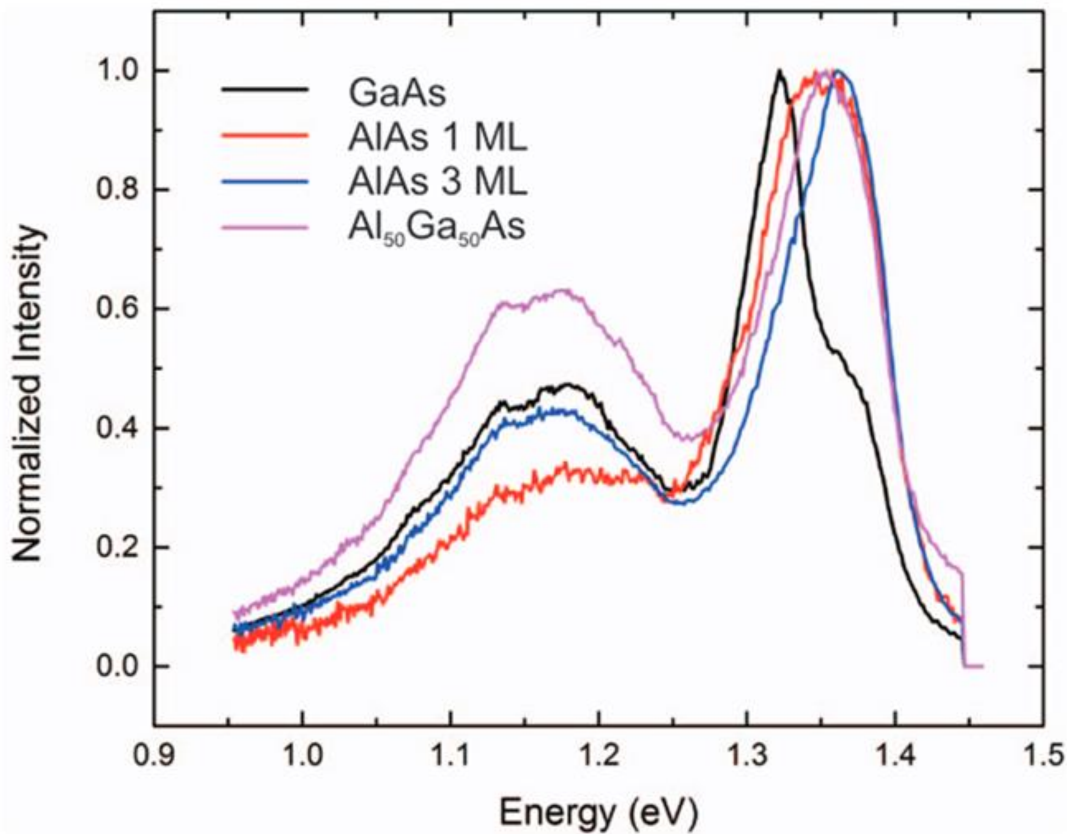

Figure 2.5: Normalized photoluminescence measurements of the four capped samples

The trends observed in **Fig. 2.5** is consistent with the XSTM images. The peak positions and relative intensities are also photoluminescence measurements in other quantum dot studies.[20-22] In **Fig. 2.5** there is a blue shift in the wetting layer peak from the control to the Al-rich samples. The higher energy emission could be from one of two causes. One possibility is that Al incorporated into the wetting layer and the blue shift is from the resulting larger bandgap. Another possibility is that the blue shift arises from a thinner GaSb wetting layer. It has previously been reported that the Sb out-diffusion that occurs during capping will incorporate into the surrounding wetting layer.[22] In the Al-rich samples, we have demonstrated that Al prevents the out-diffusion of Sb and it is expected this would result in a thinner GaSb wetting layer. A thinner GaSb wetting layer would emit at higher energies as represented in **Fig. 2.5.** Considering larger quantum dots in in the Al-rich samples are larger in size (**Fig. 2.3**) it might be expected for them to emit at lower energies than the control. However, this is not observed and the quantum dot peak in all four samples emit at the same position. It is suggested that only the smaller quantum dots with an average height similar to those in the GaAs control are contributing to the emission.

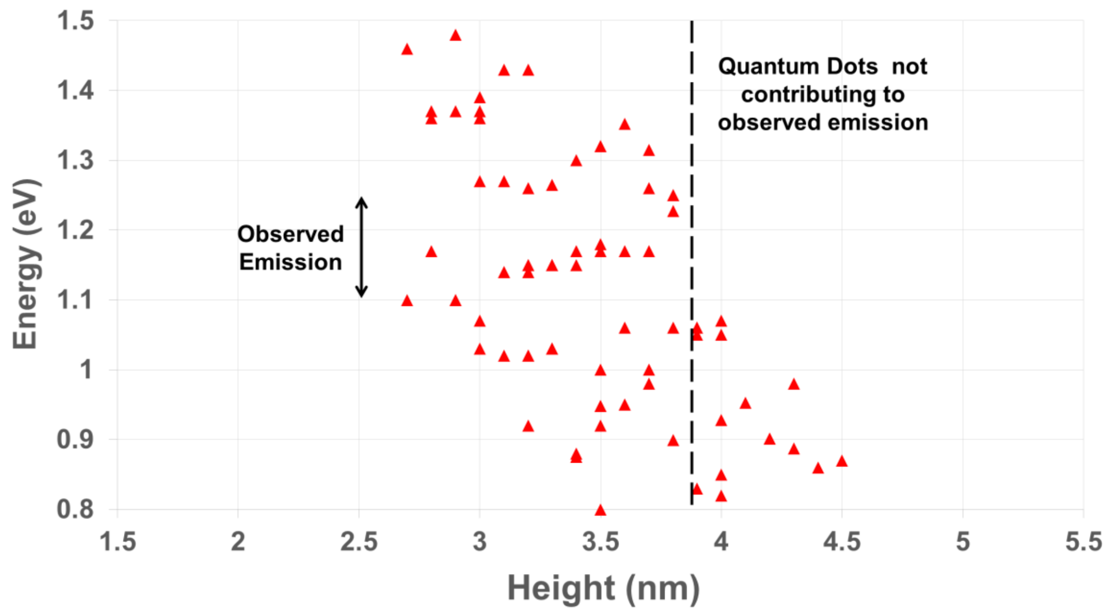

Figure 2.6: Chart showing the ground state emission for simulated quantum dots with various heights

Nemo 3D's Quantum Dot Lab tool[23] was used to simulate the ground state energy state of strained GaSb quantum dots at T=10K. **Figure 6** shows the ground state emission energy vs. quantum dot height. Pyramidal quantum dots with heights of 2.4-6.0nm, diameters of 5-16nm, and aspect ratios of 0.2-0.5 were simulated. Experimentally it is observed that the quantum dots emit between 1.10 and 1.25eV (**Fig. 5**). The simulated quantum dots that emit in this range are between 2.5 and 4.0nm tall, which is shorter than the average height of the quantum dots in the Al-rich sample. As such, it is possible that the larger quantum dots measured in **Fig.4** are not emitting and consistent with the suggestion that only the smaller quantum dots are contributing to the PL. Also, the larger quantum dots have a higher percentage to be surrounded with defects, and these defects may be acting as non-radiative recombination centers.

2.4 Conclusions

In summary it is demonstrated that the addition of Al to the GaAs capping layer can improve the retention of GaSb quantum dots. The percentage of intact quantum dots is improved from 53% to 83% in the Al-rich compounds. The Al-compounds successfully curtail the out-diffusion of Sb from the GaSb quantum dot, resulting in taller quantum dots. Defects form in the capping layer to compensate for the strain imposed by the larger quantum dots. The optical PL measurements are consistent with the XSTM measurements. A blue shift is observed in the wetting layer emission consistent with a thinner wetting layer in the Al-rich samples. No shift is observed in the quantum dot peak as only the smaller quantum dots, a feature shared in both the control and Al-samples, are emitting.

2.5 References

1. Timm, R., Eisele, H., Lenz, A., Becker, S. K., Grabowski, J., Kim, T. Y., ... & Dähne, M. (2004). Structure and intermixing of GaSb⁄GaAs quantum dots. *Applied physics letters*, *85*(24), 5890-5892.
2. Timm, R., Eisele, H., Lenz, A., Ivanova, L., Balakrishnan, G., Huffaker, D. L., & Dähne, M. (2008). Self-organized formation of GaSb/GaAs quantum rings. *Physical review letters*, *101*(25), 256101.
3. Kamarudin, M. A., Hayne, M., Zhuang, Q. D., Kolosov, O., Nuytten, T., Moshchalkov, V. V., & Dinelli, F. (2010). GaSb quantum dot morphology for different growth temperatures and the dissolution effect of the GaAs capping layer. *Journal of Physics D: Applied Physics*, *43*(6), 065402.
4. Smakman, E. P., Garleff, J. K., Young, R. J., Hayne, M., Rambabu, P., & Koenraad, P. M. (2012). GaSb/GaAs quantum dot formation and demolition studied with cross-sectional scanning tunneling microscopy. *Applied Physics Letters*, *100*(14), 142116.
5. Martin, A. J., Hwang, J., Marquis, E. A., Smakman, E., Saucer, T. W., Rodriguez, G. V., ... & Millunchick, J. (2013). The disintegration of GaSb/GaAs nanostructures upon capping. *Applied Physics Letters*, *102*(11), 113103.
6. Blossey, R., & Lorke, A. (2002). Wetting droplet instability and quantum ring formation. *Physical Review E*, *65*(2), 021603.
7. Marent, A., Geller, M., & Bimberg, D. (2009). A novel nonvolatile memory based on self-organized quantum dots. *Microelectronics Journal*, *40*(3), 492-495.
8. Marent, A., Nowozin, T., Geller, M., & Bimberg, D. (2010). The QD-Flash: a quantum dot-based memory device. *Semiconductor Science and Technology*, *26*(1), 014026.

9. Nowozin, T., Bonato, L., Högner, A., Wiengarten, A., Bimberg, D., Lin, W. H., ... & Huffaker, D. L. (2013). 800 meV localization energy in GaSb/GaAs/Al0. 3Ga0. 7As quantum dots. *Applied Physics Letters*, *102*(5), 052115.
10. Luque, A., & Martí, A. (1997). Increasing the efficiency of ideal solar cells by photon induced transitions at intermediate levels. *Physical Review Letters*, *78*(26), 5014.
11. Cuadra, L., Martı, A., & Luque, A. (2002). Type II broken band heterostructure quantum dot to obtain a material for the intermediate band solar cell. *Physica E: Low-dimensional Systems and Nanostructures*, *14*(1), 162-165.
12. Luque, A., & Martí, A. (1997). Increasing the efficiency of ideal solar cells by photon induced transitions at intermediate levels. *Physical Review Letters*, *78*(26), 5014.
13. Cuadra, L., Martı, A., & Luque, A. (2002). Type II broken band heterostructure quantum dot to obtain a material for the intermediate band solar cell. *Physica E: Low-dimensional Systems and Nanostructures*, *14*(1), 162-165.
14. Laghumavarapu, R. B., Moscho, A., Khoshakhlagh, A., El-Emawy, M., Lester, L. F., & Huffaker, D. L. (2007). GaSb⁄ GaAs type II quantum dot solar cells for enhanced infrared spectral response. *Applied Physics Letters*, *90*(17), 173125.
15. Gong, Q., Offermans, P., Nötzel, R., Koenraad, P. M., & Wolter, J. H. (2004). Capping process of InAs⁄ GaAs quantum dots studied by cross-sectional scanning tunneling microscopy. *Applied physics letters*, *85*(23), 5697-5699.
16. Offermans, P., Koenraad, P. M., Wolter, J. H., Granados, D., García, J. M., Fomin, V. M., ... & Devreese, J. T. (2005). Atomic-scale structure of self-assembled In (Ga) As quantum rings in GaAs. *Applied Physics Letters*, *87*(13), 131902.

17. Huang, S. H., Balakrishnan, G., Khoshakhlagh, A., Jallipalli, A., Dawson, L. R., & Huffaker, D. L. (2006). Strain relief by periodic misfit arrays for low defect density GaSb on GaAs. *Applied physics letters*, *88*(13), 131911.

18. Balakrishnan, G., Tatebayashi, J., Khoshakhlagh, A., Huang, S. H., Jallipalli, A., Dawson, L. R., & Huffaker, D. L. (2006). III/V ratio based selectivity between strained Stranski-Krastanov and strain-free GaSb quantum dots on GaAs. *Applied physics letters*, *89*(16), 161104.

19. Mikkelsen, A., Sköld, N., Ouattara, L., Borgström, M., Andersen, J. N., Samuelson, L., ... & Lundgren, E. (2004). Direct imaging of the atomic structure inside a nanowire by scanning tunnelling microscopy. *Nature materials*, *3*(8), 519-523.

20. Hatami, F., Ledentsov, N. N., Grundmann, M., Böhrer, J., Heinrichsdorff, F., Beer, M., ... & Heydenreich, J. (1995). Radiative recombination in type-II GaSb/GaAs quantum dots. *Applied physics letters*, *67*(5), 656-658.

21. Alonso-Álvarez, D., Alén, B., García Martínez, J. M., & Ripalda, J. M. (2007). Optical investigation of type II GaSb/GaAs self-assembled quantum dots.

22. Martin, A. J., Hunter, A. H., Saucer, T. W., Sih, V., Marquis, E. A., & Millunchick, J. (2013). Atom probe tomography analysis of different modes of Sb intermixing in GaSb quantum dots and wells. *Applied Physics Letters*, *103*(12), 122102.

23. Klimeck, G., Lee, S., & Ryu, H. (2008). Introduction to Quantum Dot Lab. *Retrieved August*, *11*, 2012.

Chapter 3
Droplet Epitaxy in Lattice Mismatched Systems

This chapter explores the use of droplet epitaxy as a growth mechanism for GaSb quantum dots on GaAs surfaces. We observe that growth results differ greatly with what has been reported in GaAs/AlGaAs droplet epitaxy. This is due to a higher crystallization energy (E_C) in lattice mismatched systems. The GaSb nanostructure morphologies change from two dimensional islands and nano-pores at low temperatures, to disks and compact islands at high temperatures. The structure's shape is determined by the initial Ga_ℓ droplet volume which is a function of substrate temperature. A qualitative model using volumetric relationships is proposed to explain the formation mechanism. Kinetic Monte Carlo simulations validate the model with results that closely mirror the observed nanostructures. The combined experimental and simulation results demonstrate another process to obtain complex nanostructures, widening the design window for devices.

3.1 Introduction

Self-assembled quantum dots have garnered a lot of interest[1,2] because of their potential for many optoelectronic devices such as quantum computing,[3] photodetectors,[4] lasers,[5] spin memory devices,[6] solar cells,[7] and light emitting diodes.[8] GaSb quantum dots in GaAs are of particular interest because they exhibit a type II band structure.[9] This can create spatial separation of charged carriers,[10] increasing recombination time, and reducing thermal emission,[11] which is especially promising for photovoltaic applications. GaSb quantum dots are typically grown using the Stranski-Krastanov (SK) growth mechanism.[12] However, quantum dots grown using this mechanism have been reported to demolish into a range of nanostructures upon capping.[13] The quantum dots that remain intact are surrounded by strain induced defects. Shorter quantum dots show a decreased tendency to be defected, but SK growth gives little control over quantum dot size and shape distribution. An alternative method that has emerged is droplet epitaxy.[14,15] Droplet epitaxy does not require strain for nanostructure formation, and has enabled the creation of quantum dots in previous inaccessible systems. Another advantage is that droplet epitaxy can be easily tuned to create a variety of structures, such as compact islands, disks, and disks.[16-18] This has been demonstrated extensively in the GaAs/AlGaAs system.[19-21] Prior to this work, studies on GaSb droplet epitaxy have only reported compact island formation.[22-26] In this work we examine droplet epitaxy growth in GaSb/GaAs which is a lattice mismatched system. We demonstrate that nanostructures ranging from 2D islands, to nano-pores, disks, and compact islands can be grown by modifying the substrate temperature and Sb deposition rate. The influence of temperature on the nanostructure morphology is very different than what is reported in lattice matched

systems.[27,28] A mechanism is proposed and explained using a qualitative model based on volumetric relationships. The model and results are corroborated with Kinetic Monte Carlo simulations. The model and observed mechanisms allow for the controlled design of GaSb/GaAs nanostructures and can be extended to droplet epitaxy growths in other lattice mismatched systems.

3.2 Experimental Methods

GaSb nanostructures were grown on Si-doped n-type (100) GaAs substrates in a molecular beam epitaxy chamber. Each sample had a 500nm GaAs buffer layer grown at T_s=570°C grown at a Ga deposition rate r_{Ga}=0.6 ML/s with an As flux BEP_{As}= 6x10^{-6} Torr. After buffer layer growth the substrate temperature was reduced to T_S=200°C at which the concurrent As overpressure flux was terminated. The sample was then annealed for 30 minutes during which the chamber pressure, measured by a tungsten ion gauge, typically reached 4x10^{-9} Torr. Afterwards the sample was heated to 200°C ≤ T_s ≤ 400°C without any group V overpressure. Once the substrate equilibrated to the desired growth temperature, droplets were formed by depositing 3ML of Ga at a rate of 0.4 ML/s. To create GaSb nanostructures, the Ga_ℓ droplets were subjected to an Sb flux. There was a 1s delay after closing the Ga shutter before the droplets were subjected to an Sb flux of BEP_{Sb}=8x10^{-7} Torr. The shutter controlling Sb remained open for 2, 5, or 10 seconds. The Sb flux step was limited to 2s at T_s=200°C because further Sb deposition resulted in a polycrystalline Sb film and obscured the nanostructures. Lower substrate temperatures required shorter Sb shutter times to prevent polycrystalline Sb from forming on the surface. After Sb deposition each sample was annealed for 60s at the deposition

temperature and then rapidly cooled to room temperature. Reflection high energy electron diffraction (RHEED) measurements were taken during the deposition steps to measure surface structure during nanostructure formation. The GaAs film exhibited streaks corresponding to a c(4x4) surface prior to droplet epitaxy growth. The RHEED transitioned to halos upon the deposition of Ga droplets and became a spot pattern after Sb crystallization. The surface topography of each sample was measured with atomic force microscopy (AFM). For enhanced AFM resolution, 2nm diameter silicon probes were used.

3.3 Data Analysis

3.3.1 GaSb Quantum Dots grown by Droplet Epitaxy

A series of droplet epitaxy GaSb nanostructures grown at increasing substrate temperatures and measured by AFM is presented in **Fig. 3.1**. The structures grown at T_s=200°C (**Fig. 3.1a**) are a series of wide 2D islands less than a nanometer tall and 60-200nm wide. The underlying GaAs buffer layer consisted of periodic steps and it is likely the 2D islands are from Sb-limited film growth where the Ga was provided by the initial droplets.[29] There is no evidence of crystallized 3D Ga droplets, likely because at T_s=200°C the initial droplet size is very small. The initial Ga droplet size is dependent on the substrate temperature and increasing the substrate temperature increases the initial droplet size.[30] **Figure 3.1b** shows nanostructures grown at T_s=250°C. The structures in **Fig. 3.1b** very closely resemble **Fig. 3.1a** in that they are both predominantly 2D islands. However, in **Fig. 3.1b** there are some 3D features, namely the nano-pores (circled). These holes are 6-7nm wide and arise from etching of the substrate by the liquid Ga

droplets prior to Sb crystallization. Substrate dissolution is a function of temperature with Ga_ℓ droplet etching effects being more prominent at higher temperatures.[21] The 2D islands in **Fig. 3.1b** are 20-30 nm wide and are confined to regions near holes. The 2D islands are smaller and more isolated than those in **Fig. 3.1a**. The nanostructures grown at T_s=300°C are disks (**Fig. 3.1c**), each with a hole in the center. 3D islands 2-3nm in height (arrows) can be seen decorating the perimeter of each hole. Surrounding the holes and 3D islands is a raised disk approximately 0-3nm in height and 80-120nm in diameter. The holes in **Fig. 3.1c** are 11-13nm wide, larger than the holes in **Fig. 3.1b,** which is consistent with larger Ga_ℓ at higher temperatures. Further increasing the T_s to 400°C (**Fig. 3.2**) results in a high density of 3D compact islands. At the center of each group of compact islands is a hole and an enlarged island. A close up of one of these features can be seen in **Fig. 3.2a**. The hole is 22-27nm wide, larger than those present in **Fig. 3.1b** and **Fig. 3.1c** and the island directly on its perimeter is 5nm tall and 30nm wide. The remainder of the islands are 15-30nm wide and 3-4nm tall. The “halo” of islands is fairly isotropic and approximately 400nm in diameter, much larger than the disks in **Fig. 3.1c**. A lower magnification image of the T_s=400°C nanostructures (**Fig. 3.2b**) shows that many of the halos overlap with each other. Each halo of compact islands corresponds to a single Ga_ℓ droplet, and they because the initial droplets were spaced closer than 400nm (the halo diameter) on average.

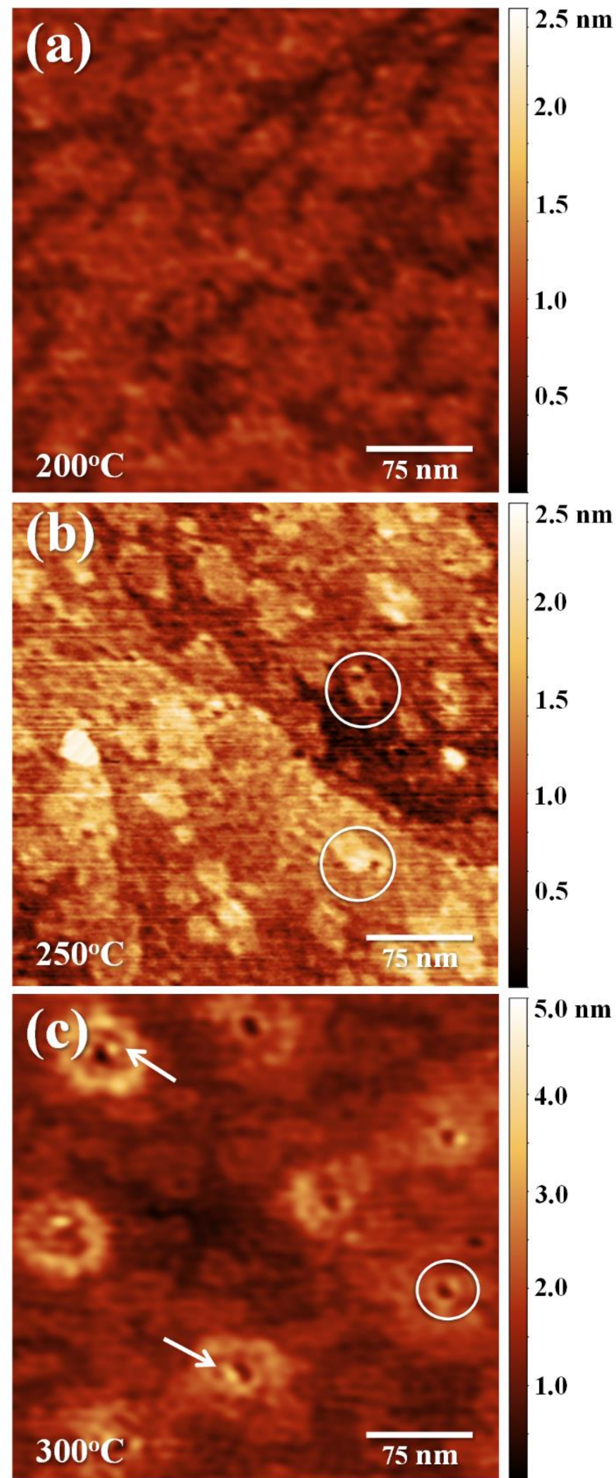

Figure 3.1: AFM images of nanostructures grown by droplet epitaxy at substrate temperatures of a) 200°C, b) 250°C, and c) 300°C

Examining the nanostructures presented in **Figures 3.1** and **3.2** independently, they are qualitatively similar to those reported in GaAs/AlGaAs droplet epitaxy studies. Pores, disks, and 3D compact islands are present in both material systems, but the growth conditions necessary for fabrication are very different. In GaAs droplet epitaxy, compact islands are observed at low temperatures, while disks and pores only form at high temperatures and/or low As fluxes.[31,32] From **Figures 3.1** and **3.2** we demonstrate that disks and pores appear at low temperatures in GaSb/GaAs droplet epitaxy, whereas high temperatures result in a high density of compact islands. While it is likely that the nanostructure shapes result from the same mass-transport mechanisms, there is an additional factor in lattice-mismatched droplet epitaxy that is impacting droplet crystallization.

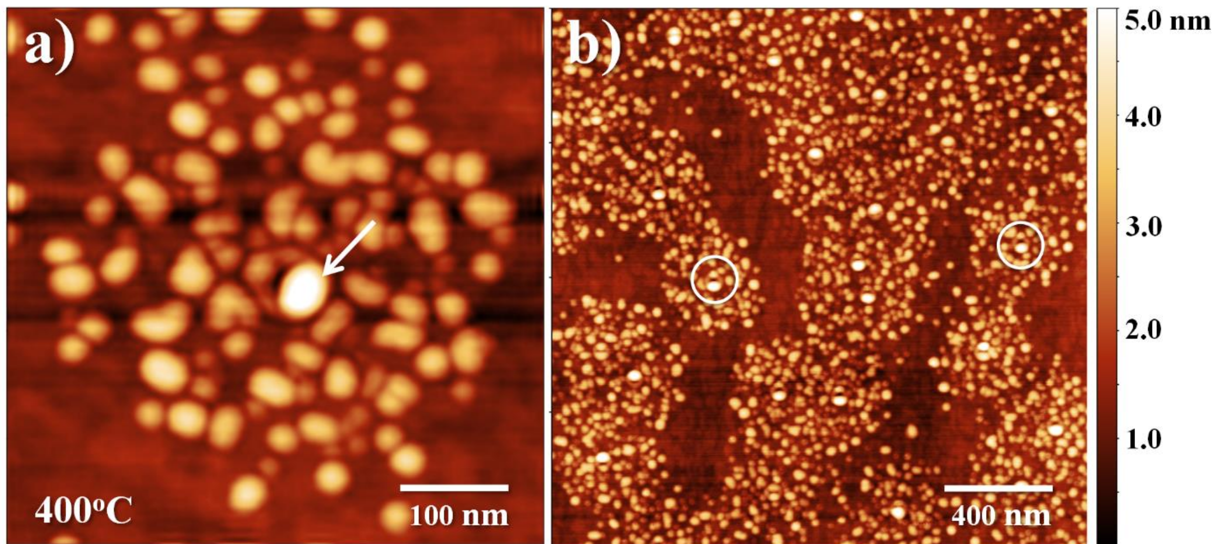

Figure 3.2: AFM images of a a) single halo nanostructure and of b) multiple halo nanostructures grown at 400°C

3.3.2 Droplet Epitaxy Mechanisms in Lattice Mismatched systems

A model for droplet epitaxy in lattice matched systems has been previously proposed by *Reyes et al* [32] and accounts for the formation of the different nanostructure morphologies. In this model, the morphology of the GaAs nanostructure is strongly influenced by two mechanisms, the crystallization of Ga_ℓ with As to form GaAs, and the out-diffusion of Ga_ℓ from the droplet center, a process we describe as wicking. We believe that these mechanisms are also present in lattice-mismatched systems, but with a significant difference in the crystallization process. In lattice-matched systems, the energy for crystallization is very low compared to heterogeneous crystallization of lattice-mismatched materials. As such, there is some energy barrier for crystallization (E_C) in the GaSb/GaAs that is not present or not a limiting factor in the GaAs crystallization on AlGaAs. In lattice-mismatched droplet epitaxy, this energy barrier manifests itself in the form of an incubation time approximated with the formula:[33]

$$t_i \approx \frac{1}{kTF_{Sb}} e^{\frac{E_c}{kT}} \tag{1}$$

where k is the Boltzmann's constant, F_{Sb} is the Sb deposition rate in atoms per unit time, T_s is the substrate temperature, and E_c is the energy barrier for crystallization. Crystallization only begins once the energy barrier is overcome, which takes a certain amount of time, t_i. In the case of lattice-matched systems, GaAs/AlGaAs, the incubation time goes to zero, and can be modeled with the equation in Ref.[32] To better explain how this impacts GaSb crystallization, we can consider the change in volume of a Ga_ℓ droplet over time:

$$V(t) = V_0 - V_c(t) - V_w(t) \tag{2}$$

where V_0 is the initial droplet volume V_c is the volume of Ga_ℓ that is lost due to crystallization events and V_w is the volume of Ga_ℓ that is lost due to wicking events. Furthermore, t=0 corresponds to onset of Sb deposition. After a certain time has passed, the Ga_ℓ is consumed completely by these competing mechanisms. The crystallization term, V_c, can be explained in greater detail as follows:

$$V_c(t) = \begin{cases} 0 & t < t_i \\ 2\pi\alpha(R_0 - (t - t_i)\mathrm{v_c})\big((t - t_i)\mathrm{v_c}\big)^2 & t \geq t_i \end{cases} \tag{3}$$

where t_i is the incubation time for crystallization to begin, R_0 is the initial radius of the droplet, v_c is the crystallization velocity at the growth front, and α is a shape form factor. At $t<t_i$ none of Ga_ℓ has crystallized, but at t_i, crystallization is initialized at the triple point of the droplet and advances towards the droplet core at a velocity v_c. The model assumes that the crystallization front is uniform around the perimeter of the droplet and therefore can be modeled as a toroid. **Figure 3.3** visualizes these terms in a cross-sectional 3D schematic of toroid crystallization. The wicking term V_w can be described as follows:

$$V_w(t) = \begin{cases} 2\pi \mathrm{l}\sqrt{F_{Sb}D}R_0 t & t < t_i \\ 2\pi \mathrm{l}\sqrt{F_{Sb}D}(R_0 - (t - t_i)\mathrm{v_c})t & t \geq t_i \end{cases} \tag{4}$$

where R_0 is the initial radius of the droplet, , F_{Sb} is the Sb deposition rate in atoms per unit time, D is the effective diffusion constant of Ga on the substrate surface, and ℓ is the thickness layer of the material being wicked, which is on the order of the lattice parameter. Wicking occurs when the surface tension of the droplet is broke and Ga_ℓ diffuses away from the droplet. This is because when Sb is introduced, the adjacent areas which were

group III terminated become Sb-rich, making it energetically favorable for Ga_ℓ to wet the surface. As such, there is a thermodynamic driving force for the Ga_ℓ to be wicked out of the droplet by capillary forces that we model to occur at some velocity proportional to $(F_{Sb}D)^{1/2}$.[32] The 2D islands, disks, and halos observed in **Fig. 3.1** and **Fig. 3.2** are annulus of GaSb to form around each droplet from the wicked Ga_ℓ in agreement with (4). The isotropic nature of the experimental disks suggests that diffusivity of Ga on GaSb/GaAs surfaces is also isotropic. We expect the thickness of this annulus to decrease further away from the droplet. From (4), the time for the entire initial droplet volume, V_0, to be lost to wicking processes is as follows:

$$t_w = \frac{V_o}{2\pi R_0 l \sqrt{F_{Sb}D}} \quad (5)$$

where R_0 is the initial radius of the droplet, ℓ is the thickness layer of the material being wicked, F_{Sb} is the Sb deposition rate in atoms per unit time, and D is the diffusion constant of Ga on the substrate surface. For growth conditions where the incubation time is greater than the wicking time, $t_i > t_w$, all of the Ga_ℓ wicks out before any crystallization events occur, resulting in a thin annular GaSb film surrounding the droplet center. This type of behavior is observed in **Fig. 3.1a** and **Fig. 3.1b**. To ensure 3D nanostructure formation the incubation time needs to be shorter than the wicking time, and this can be manipulated by changing the growth conditions. An increase in substrate temperature T_s will reduce the incubation time (1), but also impacts the terms D_{Ga} and V_0. Namely, the diffusion constant increases with temperature as does the initial droplet volume. These terms are competing processes (5), in that a higher V_0 is conducive to droplet crystallization, whereas a higher D_{Ga} means the Ga_ℓ wicks at a faster rate. In **Fig. 3.1** and **Fig. 3.2** the nanostructures have more 3D features at higher temperatures, suggesting V_0 is more

greatly impacted by T_s than D_{Ga}. At low temperatures, **Fig. 3.1a** and **Fig. 3.1b** the droplet volume is very small with a large t_i. As a result, the entire droplet wicks away before any crystallization can occur and 2D islands form. In **Fig. 3.1c** and **Fig. 3.2** the droplet volume is large with a smaller t_i, meaning some of the droplet crystallizes along the perimeter. Wicking still occurs as evident by the disk in **Fig. 3.1c** and the halo of islands in **Fig. 3.2**, where the halo in has a greater diameter due to the faster D_{Ga} at higher temperatures.

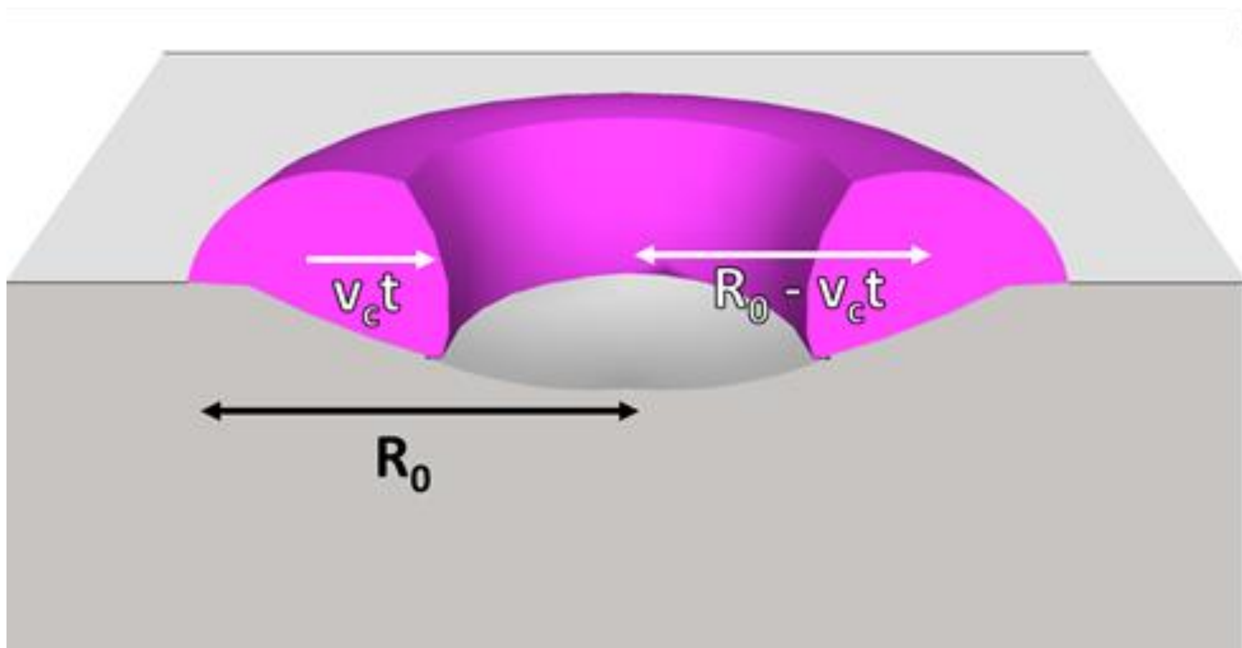

Figure 3.3: Schematic illustrating toroid formation that occurs during the initial stages of droplet epitaxy crystallization

3.3.3 Morphology Control with Droplet Epitaxy

The other term mentioned in equations 1-5 is the Sb flux F_{Sb}. While F_{Sb} has an inverse relationship with both crystallization and wicking, the incubation time is proportional to F_{Sb}^{-1} whereas the wicking time is proportional to $F_{sb}^{-1/2}$, meaning a change in F_{Sb} has a greater impact on t_i. **Figure 3.4** shows GaSb nanostructures grown at T_s=300°C with a F_{sb}=4x10^{-7} Torr. The nanostructures appear as 20-25nm diameter rings around a 10-15nm hole. Each hole has a large 3D structure along the perimeter that is 4nm in dimeter and 3nm tall. The sample grown in **Fig. 3.4** is grown at the sample temperature as those in **Fig. 3.1c** (300°C) but with half of the F_{Sb}. As such, we observe an increase in wicking effects, and a reduction in crystallization effects. The inner structure in **Fig. 3.1c** is similar to the rings in **Fig. 3.4**, but instead disks there are 2D islands of presumably GaSb. With a lower F_{Sb}, more Ga_ℓ was able to wick from the droplet before crystallization, as evident by the differences in the annular GaSb structure.

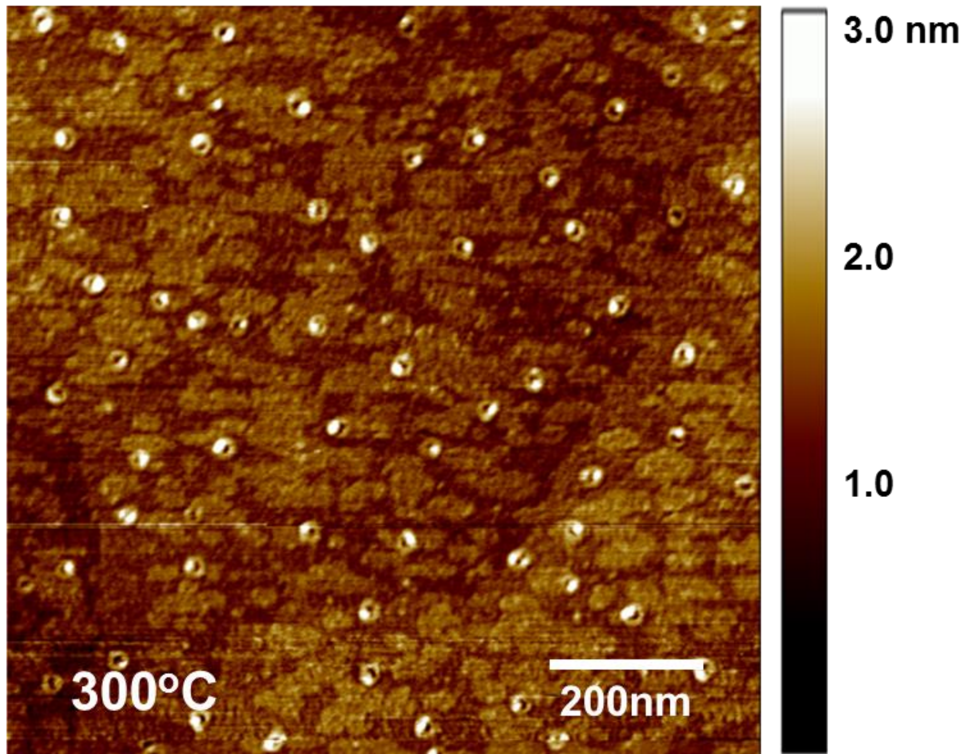

Figure 3.4: AFM scan of ring shaped GaSb nanostructures with protrusions grown at 250°C

Another method of controlling the growths not mentioned in equations 1-5 is by modifying the amount of material deposited. Depositing more Ga_ℓ will increase the droplet volume V_0. **Figure 3.5** shows a film grown at 250°C, the same temperature as the growth in **Fig. 3.1b**, except that 4 ML of Ga_ℓ is deposited instead of 3ML. The nanostructures in **Fig. 3.5** are 40-45nm wide rings surrounding 10-15nm holes with protrusions measuring 10nm wide and 4nm tall (arrows). This is in stark contrast to the 2D islands in **Fig. 3.1b**. Increasing V_0 increased the wetting time such that $t_i < t_w$ and ring shaped nanostructures form as a result of droplet crystallization.

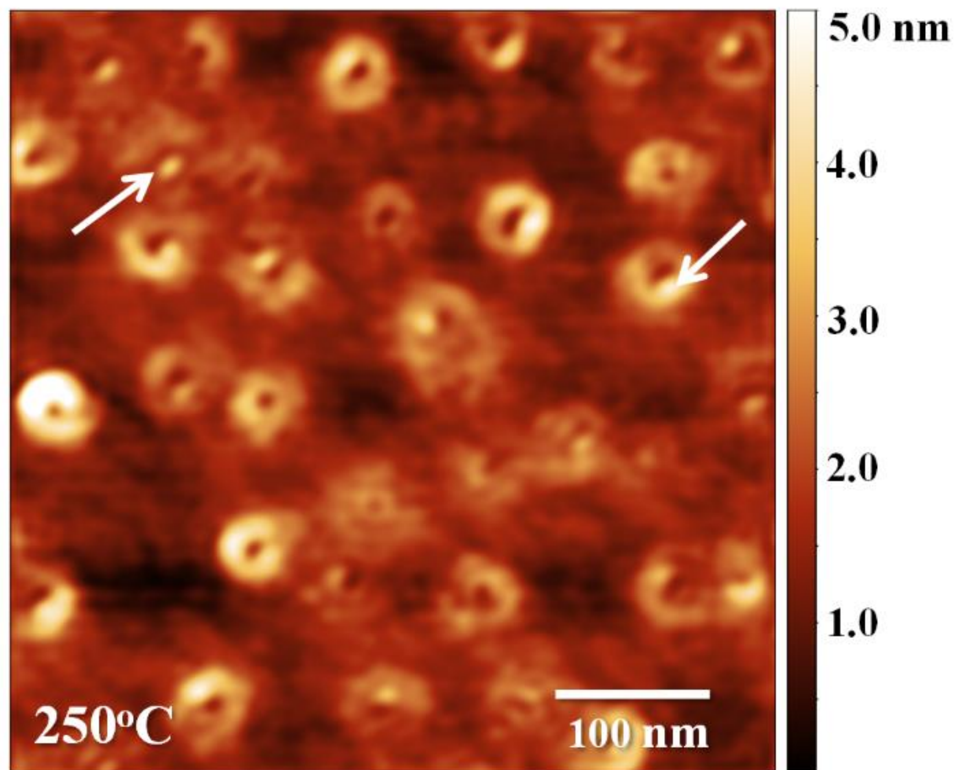

Figure 3.5: AFM image of ring GaSb nanostructures grown at 250°C after depositing 4 monolayers of Ga.

3.3.4 Kinetic Monte Carlo Simulations

Lastly, up on until now our discussion has largely ignored the elastic strain. During crystallization, strain develops due to the misfit between GaSb and GaAs, and portions of the film that are thicker than the critical thickness will be unstable and 3D islands will form. This is from weak elastic and strong surface forces with this instability occurring over relatively large length and time scales. It is reasonable to assume that this occurs at a time scale much greater than t_i and t_w, and as such we simulate a strained GaSb film using Kinetic Monte Carlo (KMC). The KMC simulations use the strained epitaxial growth method used by Smereka and Schulze,[34] a short summary of the model can be found in Refs.[34-39] and it is based in part on algorithms developed in Ref.[40] The simulations were annealed until the morphologies equilibrated into its metastable configuration.

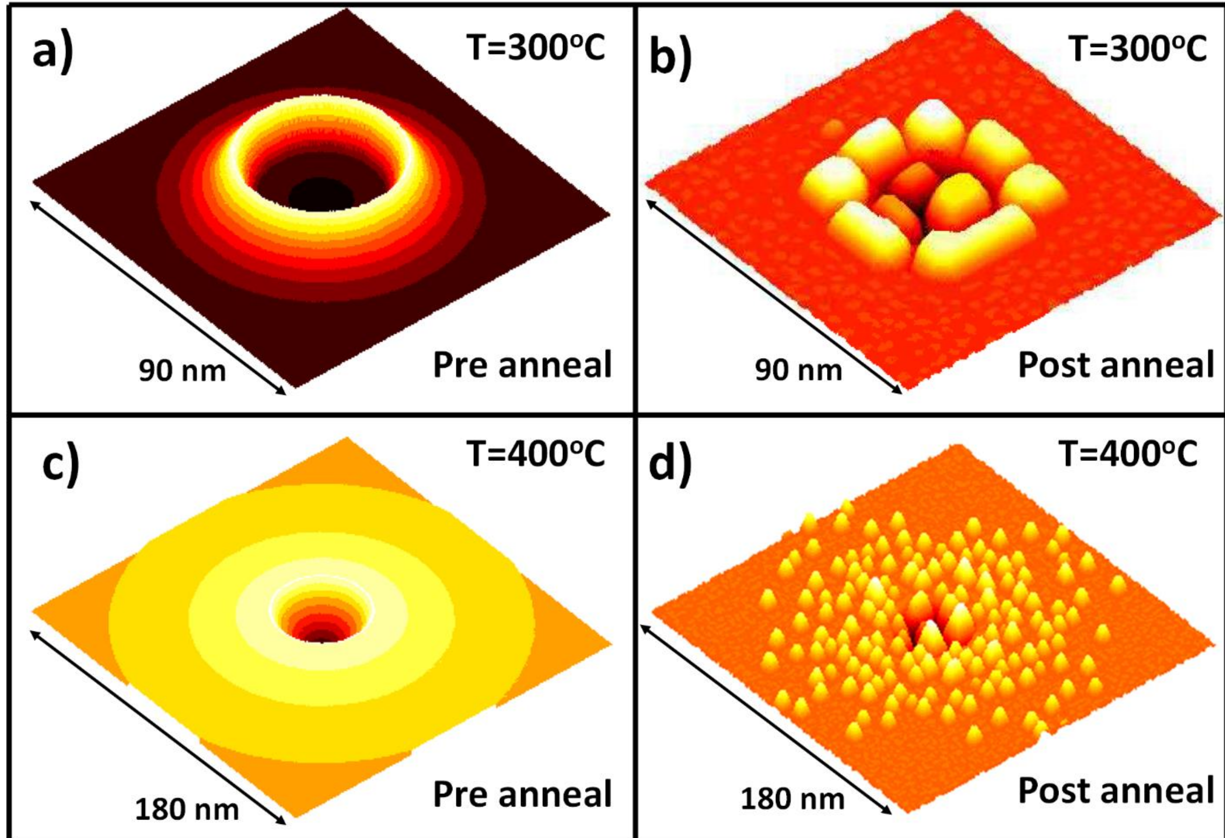

Figure 3.6: Kinetic Monte Carlo Simulations of toroids before and after annealed at a,b) 300°C and c,d) 400°C

Figure 3.6 shows two simulation examples, one at T_s=300°C and one at T_s=400°C, and in both examples t_w>t_i. The simulations begin (**Fig. 3.6a** and **Fig. 3.6c**) as crystallized GaSb annulus in a toroid shape with exponentially decaying heights. The higher temperature structure has a larger radius and thinner profile. After annealing, the structure at T_s=300°C breaks up to lower the strain energy, forming 3D islands around the crater (**Fig. 3.6b**). Similarly, after annealing the structure at T_s=400°C, the toroid breaks up into 3D islands (**Fig. 3.6d**). Due to the large size of the higher temperature structure, multiple islands form along the length of the radius. The post-annealed nanostructures observed in **Fig. 3.6b** and **Fig. 3.6d** closely resemble the experimental growth sin **Fig. 3.1c** and **Fig. 3.2**, corroborating the model and relationships presented in this work. Halos such as

those present in **Fig. 3.2** and **Fig. 3.6b** have been observed in other lattice mismatched systems, namely InAs/GaAs droplet epitaxy, except that halos are anisotropic in shape due to anisotropic diffusion.

3.4 Conclusions

This work shows that droplet epitaxy of GaSb can be used to create a wide range of nanostructures including 2D islands, holes, disks, rings, halos, and compact islands. We demonstrate control over the morphology by changing substrate temperature, the amount of Ga_ℓ deposited, and Sb flux. The droplet epitaxy growth is a competition between the outdiffusion and crystallization of Ga_ℓ. At small droplet volumes, characteristic of low temperatures, Ga_ℓ outdiffusion dominates with only 2D structures visible. At large droplet volumes, characteristic of high temperatures, crystallization of the Ga_ℓ is much more prevalent. Depositing more Ga_ℓ allows for the crystallization of 3D features at lower temperatures, and using a lower Sb flux allows more Ga_ℓ outdiffusion. Wicking occurs concurrently with crystallization, and if the thickness of the wicking layer greater than the critical thickness, it can form 3D islands. The growth mechanisms for lattice mismatched droplet epitaxy are modelled using volumetric relationships and corroborated using Kinetic Monte Carlo simulations.

3.5 References

1. Hatami, F., Grundmann, M., Ledentsov, N. N., Heinrichsdorff, F., Heitz, R., Böhrer, J., ... & Kop'ev, P. S. (1998). Carrier dynamics in type-II GaSb/GaAs quantum dots. *Physical Review B*, *57*(8), 4635.
2. Martin, A. J., Saucer, T. W., Sun, K., Kim, S. J., Ran, G., Rodriguez, G. V., ... & Millunchick, J. (2012). Analysis of defect-free GaSb/GaAs (001) quantum dots grown on the Sb-terminated (2× 8) surface. *Journal of Vacuum Science & Technology B*, *30*(2), 02B112.
3. Loss, D., & DiVincenzo, D. P. (1998). Quantum computation with quantum dots. *Physical Review A*, *57*(1), 120.
4. Chakrabarti, S., Stiff-Roberts, A. D., Bhattacharya, P., Gunapala, S., Bandara, S., Rafol, S. B., & Kennerly, S. W. (2004). High-temperature operation of InAs-GaAs quantum-dot infrared photodetectors with large responsivity and detectivity. *IEEE Photonics Technology Letters*, *16*(5), 1361-1363.
5. Maximov, M. V., Ustinov, V. M., Zhukov, A. E., Kryzhanovskaya, N. V., Payusov, A. S., Novikov, I. I., ... & Mikhrin, S. (2008). A 1.33? m InAs/GaAs quantum dot laser with a 46 cm? 1 modal gain. *Semiconductor Science and Technology*, *23*(10), 105004.
6. Kroutvar, M., Ducommun, Y., Heiss, D., Bichler, M., Schuh, D., Abstreiter, G., & Finley, J. J. (2004). Optically programmable electron spin memory using semiconductor quantum dots. *Nature*, *432*(7013), 81-84.
7. Nozik, A. J. (2002). Quantum dot solar cells. *Physica E: Low-dimensional Systems and Nanostructures*, *14*(1), 115-120.

8. Chen, K. J., Chen, H. C., Shih, M. H., Wang, C. H., Kuo, M. Y., Yang, Y. C., ... & Kuo, H. C. (2012). The influence of the thermal effect on CdSe/ZnS quantum dots in light-emitting diodes. *Journal of Lightwave Technology*, *30*(14), 2256-2261.
9. Chen, K. J., Chen, H. C., Shih, M. H., Wang, C. H., Kuo, M. Y., Yang, Y. C., ... & Kuo, H. C. (2012). The influence of the thermal effect on CdSe/ZnS quantum dots in light-emitting diodes. *Journal of Lightwave Technology*, *30*(14), 2256-2261.
10. Nozik, A. J., Beard, M. C., Luther, J. M., Law, M., Ellingson, R. J., & Johnson, J. C. (2010). Semiconductor quantum dots and quantum dot arrays and applications of multiple exciton generation to third-generation photovoltaic solar cells. *Chemical reviews*, *110*(11), 6873-6890.
11. Hwang, J., Martin, A. J., Millunchick, J. M., & Phillips, J. D. (2012). Thermal emission in type-II GaSb/GaAs quantum dots and prospects for intermediate band solar energy conversion. *Journal of Applied Physics*, *111*(7), 074514.
12. Kobayashi, S., Jiang, C., Kawazu, T., & Sakaki, H. (2004). Self-assembled growth of GaSb type II quantum ring structures. *Japanese journal of applied physics*, *43*(5B), L662.
13. Smakman, E. P., Garleff, J. K., Young, R. J., Hayne, M., Rambabu, P., & Koenraad, P. M. (2012). GaSb/GaAs quantum dot formation and demolition studied with cross-sectional scanning tunneling microscopy. *Applied Physics Letters*, *100*(14), 142116.
14. Jo, M., Mano, T., Sakuma, Y., & Sakoda, K. (2012). Extremely high-density GaAs quantum dots grown by droplet epitaxy. *Applied Physics Letters*, *100*(21), 212113.
15. Mano, T., & Koguchi, N. (2005). Nanometer-scale GaAs ring structure grown by droplet epitaxy. *Journal of crystal growth*, *278*(1), 108-112.

16. Kuroda, T., Mano, T., Ochiai, T., Sanguinetti, S., Sakoda, K., Kido, G., & Koguchi, N. (2005). Optical transitions in quantum ring complexes. *Physical Review B*, *72*(20), 205301.
17. Kuroda, K., Kuroda, T., Watanabe, K., Mano, T., Kido, G., Koguchi, N., & Sakoda, K. (2010). Distribution of exciton emission linewidth observed for GaAs quantum dots grown by droplet epitaxy. *Journal of Luminescence*, *130*(12), 2390-2393.
18. Sanguinetti, S., Abbarchi, M., Vinattieri, A., Zamfirescu, M., Gurioli, M., Mano, T., ... & Koguchi, N. (2008). Carrier dynamics in individual concentric quantum rings: Photoluminescence measurements. *Physical Review B*, *77*(12), 125404.
19. Somaschini, C., Bietti, S., Koguchi, N., & Sanguinetti, S. (2011). Coupled quantum dot–ring structures by droplet epitaxy. *Nanotechnology*, *22*(18), 185602.
20. Mano, T., Kuroda, T., Sanguinetti, S., Ochiai, T., Tateno, T., Kim, J., ... & Koguchi, N. (2005). Self-assembly of concentric quantum double rings. *Nano letters*, *5*(3), 425-428.
21. Somaschini, C., Bietti, S., Koguchi, N., & Sanguinetti, S. (2009). Fabrication of multiple concentric nanoring structures. *Nano letters*, *9*(10), 3419-3424.
22. Fortina, S. C., Sanguinetti, S., Grilli, E., Guzzi, M., Henini, M., Polimeni, A., & Eaves, L. (1998). InAs quantum dots grown on nonconventionally oriented GaAs substrates. *Journal of crystal growth*, *187*(1), 126-132.
23. Kawazu, T., Noda, T., Mano, T., Ohmori, M., Akiyama, Y., & Sakaki, H. (2011). Growth of GaSb and InSb quantum dots on GaAs (311) A by droplet epitaxy. *physica status solidi (c)*, *8*(2), 275-277.

24. Noda, T., & Mano, T. (2008). Fabrication of a complex InAs ring-and-dot structure by droplet epitaxy. *Applied Surface Science*, *254*(23), 7777-7780.

25. Kawazu, T., Mano, T., Noda, T., Akiyama, Y., & Sakaki, H. (2009). Growth of GaSb dots on GaAs (100) by droplet epitaxy. *physica status solidi (b)*, *246*(4), 733-735.

26. Kawazu, T., Mano, T., Noda, T., & Sakaki, H. (2009). Two different growth modes of GaSb dots on GaAs (100) by droplet epitaxy. *Journal of Crystal Growth*, *311*(8), 2255-2257.

27. Wang, Z. M., Holmes, K., Mazur, Y. I., Ramsey, K. A., & Salamo, G. J. (2006). Self-organization of quantum-dot pairs by high-temperature droplet epitaxy. *Nanoscale Research Letters*, *1*(1), 57-61.

28. Somaschini, C., Bietti, S., Sanguinetti, S., Koguchi, N., & Fedorov, A. (2010). Self-assembled GaAs/AlGaAs coupled quantum ring-disk structures by droplet epitaxy. *Nanotechnology*, *21*(12), 125601.

29. Ferguson, I. T., De Oliveira, A. G., & Joyce, B. A. (1992). RHEED intensity effects during the growth of InAs, InSb and In (As, Sb) by molecular beam epitaxy. *Journal of crystal growth*, *121*(3), 267-277.

30. Heyn, C., Stemmann, A., Schramm, A., Welsch, H., Hansen, W., & Nemcsics, A. (2007). Regimes of GaAs quantum dot self-assembly by droplet epitaxy. *Physical Review B*, *76*(7), 075317.

31. Watanabe, K., Koguchi, N., & Gotoh, Y. (2000). Fabrication of GaAs quantum dots by modified droplet epitaxy. *Japanese Journal of Applied Physics*, *39*(2A), L79.

32. Reyes, K., Smereka, P., Nothern, D., Millunchick, J. M., Bietti, S., Somaschini, C., ... & Frigeri, C. (2013). Unified model of droplet epitaxy for compound semiconductor nanostructures: experiments and theory. *Physical Review B*, *87*(16), 165406.
33. Markov, I. V. (2003). *Crystal growth for beginners: fundamentals of nucleation, crystal growth and epitaxy*. World Scientific.
34. Schulze, T. P., & Smereka, P. (2012). Kinetic Monte Carlo simulation of heteroepitaxial growth: Wetting layers, quantum dots, capping, and nanorings. *Physical Review B*, *86*(23), 235313.
35. Schulze, T. P., & Smereka, P. (2009). An energy localization principle and its application to fast kinetic Monte Carlo simulation of heteroepitaxial growth. *Journal of the Mechanics and Physics of Solids*, *57*(3), 521-538.
36. Russo, G., & Smereka, P. (2006). Computation of strained epitaxial growth in three dimensions by kinetic Monte Carlo. *Journal of Computational Physics*, *214*(2), 809-828.
37. Schulze, T. P., & Smereka, P. (2011). Simulation of three-dimensional strained heteroepitaxial growth using kinetic Monte Carlo. *Communications in Computational Physics*, *10*(05), 1089-1112.
38. Baskaran, A., Devita, J., & Smereka, P. (2010). Kinetic Monte Carlo simulation of strained heteroepitaxial growth with intermixing. *Continuum Mechanics and Thermodynamics*, *22*(1), 1-26.
39. Russo, G., & Smereka, P. (2006). A multigrid-Fourier method for the computation of elastic fields with application to heteroepitaxy. *Multiscale Modeling & Simulation*, *5*(1), 130-148.

40. Keizer, J. G., Koenraad, P. M., Smereka, P., Ulloa, J. M., Guzman, A., & Hierro, A. (2012). Kinetic Monte Carlo simulations and cross-sectional scanning tunneling microscopy as tools to investigate the heteroepitaxial capping of self-assembled quantum dots. *Physical Review B*, *85*(15), 155326.

Chapter 4
A comparison of SK and DE quantum dot growth mechanisms in GaSb/GaAs system

This chapter compares GaSb nanostructures embedded in GaAs grown using the Stranski-Krastanov (SK) and droplet epitaxy (DE) growth mechanisms. Using the observations and model presented in Chapter 3 we create GaSb rings with similar dimensions to the GaSb quantum dots presented in Chapter 2 and provide a side-by-side comparison. When capped with GaAs and measured with APT, we observe that the SK dots are compositionally consistent with their topographical morphologies, but the DE structures, which appear as rings in AFM measurements, compositionally resemble compact islands. Furthermore, substantial intermixing between the Ga_ℓ droplet and the GaAs substrate during DE results in a nanostructures with only 14-20% Sb concentration as opposed to 36-40% in SK. TEM measurements of SK quantum dots show a range of intact and demolished morphologies with a percentage of structures exhibiting defects that extend from the quantum dot to the capping surface. Measurements of DE dots show uniform size and shape across the sample with no evidence of defect formation in the capping layer. Lastly, despite having drastically different structures post-capping, photoluminescence measurements of both the SK and DE samples are strikingly similar. The emission in both samples is likely caused by a shared feature such as the wetting

layer as opposed to quantum dots, especially since the Sb wetting layer concentration profiles are nearly identical between the two samples.

4.1 Introduction

GaSb quantum dots embedded in GaAs exhibit a type II band offset,[1,2] making them integral components to the design of many different next generation devices including photovoltaics,[3] lasers,[4] charge based memory devices,[5] and quantum logic gates.[6] In order for these devices to function efficiently, the embedded quantum dot morphology and their spatial distribution needs to be precisely controlled. It is typical to use strain driven mechanisms such as Strasnki-Krastanov to grow self-assembled GaSb quantum dots on GaAs surfaces.[7] After depositing a certain thickness of GaSb, the built up strain in the film causes 3D islands to form. This technique can been used to preferentially order quantum dots on surfaces with non-uniform strain fields, such as the capping layer over a previous layer of quantum dots.[8] It has been demonstrated in previous studies, as well as in Chapter 2, that embedded GaSb quantum dots have a tendency to break up into rings and clusters.[9] Droplet epitaxy is an alternative method of forming quantum dots that is not strain driven.[10] In this method, Ga is first deposited to form a liquid droplet that is then crystallized upon exposure to an Sb flux. This technique can be used to create GaSb nanostructures in a wide range of morphologies, as demonstrated in Chapter 3.[11] Much less is known about the integrity of capped droplet epitaxy nanostructures and how they compare to other capped quantum dots.

In this study we grew nanostructures of similar size using both SK and DE growth modes and compare the effects of capping in a side-by-side comparison. The nanostructures are capped in identical manners and analyzed for their integrity. Atom probe tomography and

transmission electron microscopy is used to analyze the nanostructure composition, shape, uniformity, and capping layer. Photoluminescence is used to measure the optical response of each sample, and despite significant changes in morphology and structure as a result of capping, the emission is nearly identical. This suggests that a shared feature such as the wetting layer is responsible for the response, as opposed to the capped nanostructures.

4.2 Experimental Methods

In this work, two samples were grown using a solid source molecular beam epitaxy chamber. Each sample consisted of a single layer of GaSb nanostructures, one using SK and the other DE growth methods. Initially, a 500nm GaAs buffer layer is grown on n-type (001) GaAs substrates at a growth rate of 0.6 monolayers per second (ML/s) at T_s=580°C. Afterwards the substrate was cooled to T_s=460°C and the nanostructure layer was grown. For the SK sample, Ga and Sb was concurrently deposited at a Ga deposition rate of 0.3 ML/s with a beam equivalent pressure of $BEP_{Ga}=2.2\times10^{-7}$ Torr and an Sb flux of $BEP_{Sb}=8.0\times10^{-7}$ Torr. The nanostructures were annealed for 1 minute at T_s=460°C and the growth procedure closely mimicked conditions in other GaSb SK studies. For the DE sample, the growth conditions were chosen so the nanostructures had similar dimensions to the SK sample. After buffer growth the sample was cooled to T_s=200°C and annealed for 30 minutes without any As overpressure. Next, the substrate was heated to T_s=350°C and allowed to equilibrate, while maintaining no As overpressure. Liquid Ga droplets are formed by depositing 4ML of Ga at 4ML/s ($BEP_{Ga}=2.8\times10^{-7}$ Torr) followed by 1s of annealing. GaSb nanostructures are formed by introducing the droplets to an Sb flux for

ten seconds (BEP_{Sb}=5.0x10^{-7} Torr) for 10 seconds followed by a 1 minute anneal at T_s=350°C.

An identical 50nm GaAs capping layer was grown on top of each nanostructure layer. For the first 10nm, GaAs is deposited at T_s=350°C at a Ga rate of 0.4 ML/s (BEP_{Ga}=2.8x10^{-7} Torr, BEP_{As}=6.0x10^{-6} Torr). Next, the sample was heated to T_s=460°C and 40nm of GaAs is grown at the same growth rate. The sample was annealed for 1 minute at this temperature and then rapidly cooled. The sample never exceeded the temperature used for the SK growth step to prevent any high temperature Sb diffusion and preserve the capped nanostructures morphologies.

4.3 Data Analysis

4.3.1 Morphology of SK and DE quantum dots

Figure 4.1 shows uncapped GaSb nanostructures grown by both SK and DE growth mechanisms measured by AFM. The SK nanostructures (**Fig. 4.1a**) are dots that are approximately 30±10nm in diameter and 4±1nm tall and have a planar density of 3.0x10^{10} cm^{-2}, consistent with the study in Chapter 2 and other reports. Comparatively, the DE nanostructures (**Fig. 4.1b**) are rings that have an outer diameter of 50±5nm, an inner diameter of 15±3 nm, a height of 1.5±0.5nm, and a density of 5.0x10^9 cm^{-2}. The rings are formed from competing crystallization and out diffusion events, discussed in greater detail in Chapter 3.[11] Along the perimeter of the rings there are regions of increased height as indicated by arrows. These protrusions are approximately 1nm taller than the remainder of the ring (2.5 ± 0.5 nm) and are consistent with the features observed in other DE studies, including Chapter 3.[7,11,12]

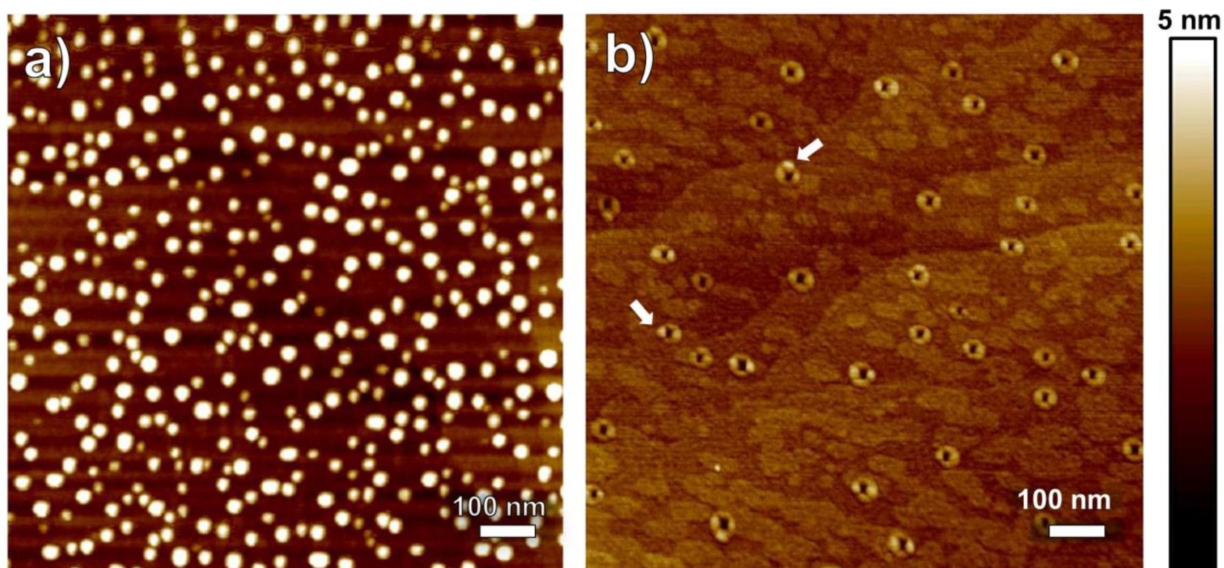

Figure 4.1: Atomic Force Micrographs of uncapped a) SK and b) DE nanostructures.

The capped nanostructures were milled into tips and measured using APT. **Figure 4.2** shows a planar top-down view of the SK (**Fig. 4.2a**) and DE (**Fig. 4.2b**) APT reconstructions. Regions that are shaded purple correspond to areas with a measured Sb concentration ≥ 9%. In each sample there is a layer of loosely scattered purple dots that occupy the entire field of view. This corresponds to the wetting layer and is present in both samples. Greater detail in how the wetting layer is formed from each of these processes can be found in Chapters 2 and 3 respectively. In each sample there are solid purple regions which correspond to the composition of the capped nanostructure. The SK nanostructure (**Fig. 4.2a**) appears as a dot that is approximately 15nm wide and 4nm tall. This is consistent with some of the smaller dots in the AFM image (**Fig. 4.1a**) and previous studies of capped SK quantum dots. Measurements of larger quantum dots by APT have

shown the effects of quantum dot dissolution.[ref] The DE nanostructures (**Fig. 4.2b**) also appear as dots in the APT measurements. The sample consists of two pairs of dots that measure 3-5nm wide and 2-3nm tall. In each pair the dots are separated by approximately 10-12nm. This is in direct contrast with the AFM image (**Fig. 4.1b**) in which the DE nanostructures appear as rings. The dots present in the APT likely correspond to the protrusions observed in **Fig. 4.1b**, but the remainder of the ring is not visible, suggesting its composition is indistinguishable from the surrounding wetting layer. As such, the ring shape is likely formed as a result of Ga_ℓ droplet substrate dissolution as opposed to Sb crystallization of Ga_ℓ. The GaAs displaced by the droplet builds up around the perimeter of the droplet creating a ring. Then when Sb is introduced, crystallization is isolated to one or two spots around the perimeter of the droplet and the remainder of the ring becomes a part of the wetting layer.

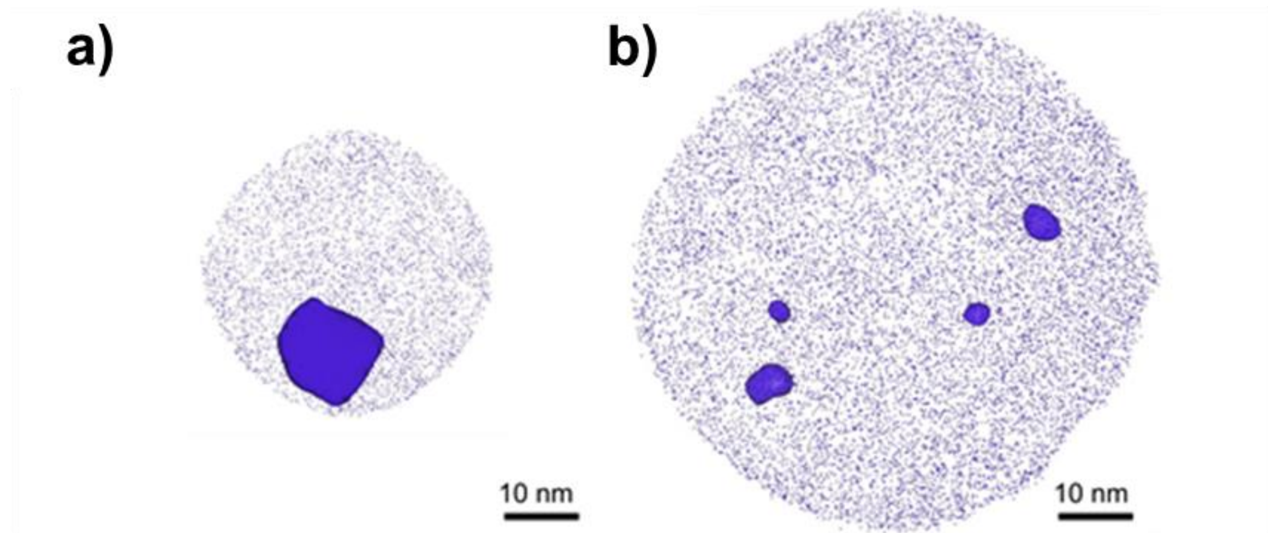

Figure 4.2: Planar sections of Atom Probe Tomography reconstructions showing the distribution of Sb atoms for a) SK and b) DE nanostructures. Areas in the APT reconstructions with at least 9% Sb concentration or higher are shaded in purple.

4.3.2 Antimony Compositional Profiles of SK and DE quantum dots

The Sb concentration was measured through the droplets and the wetting layer as a function of distance. **Figure 4.3** shows the compositional profiles in the form of cross sectional contour maps and line scans. For the contour maps of the SK (**Fig. 4.3a**) and DE (**Fig. 4.3b**) dots, a 30nm x 6nm x 6nm region was sampled and plotted as an average of the 6nm thick region. The SK map (**Fig. 4.3a**) shows a single dot that is 19nm±2nm wide, 4nm±1nm tall, and has a truncated pyramid shape with a concentration of 32%±2% in the center. The DE map (**Fig. 4.3b**) shows the cross section of two dots within a single pair. The larger dot is isotropic with a diameter of approximately 4nm±1nm and has a maximum Sb concentration of 12%±2%, significantly less than the SK dot. The concentration of the DE dot more closely resembles a GaAsSb ternary nanostructure as opposed to a pure GaSb quantum dot. During DE growth, a portion of the As in the substrate dissolves into the liquid droplet. This As later incorporates during crystallization, reducing the Sb content of the nanostructure. Line profiles taken from 2nm diameter sections and sampled through the center of both the SK and DE quantum dot can be seen in **Fig. 4.3c**. The maximum Sb concentration measured by the line profile is 36%±2% and 14%±2% in the SK and DE nanostructures respectively. The growth interface corresponds to 0nm and the maximum is reached at 1nm. The width of the profiles correspond to the height of the nanostructures and are approximately 4nm±1nm and 2nm±1nm for the SK and DE samples respectively. The slope of the Sb concentration between 0nm and 1nm in the Sk profile is twice that of the DE profile, suggesting a more balanced Sb distribution in the DE dot. This is consistent with the DE growth mechanism

and contour map in **Fig. 4.3b**. It also suggests that the DE dot is more isotropic as the concentration is more consistent across the nanostructure.

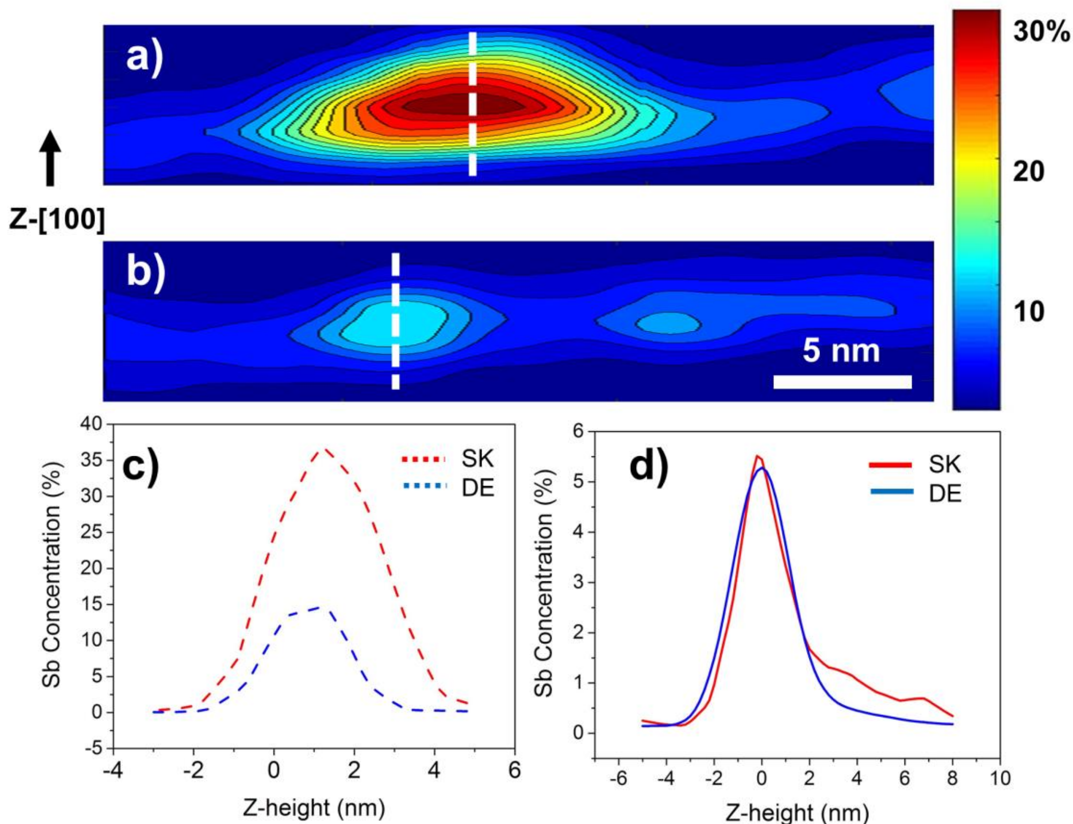

Figure 4.3: Cross-sectional contour maps of the Sb concentration in both a) SK and b) DE nanostructures. Single line Sb compositional profiles through the c) nanostructures and the d) wetting layer in both SK and DE samples.

A 10 nm diameter region of the wetting layer far removed from the quantum dots was sampled for Sb concentration. **Figure 4.3d** shows the wetting layer Sb concentration as a function of film depth in both the SK and DE samples. In both samples the Sb wetting layer had a maximum composition of 5.5% ± 1.2%. Typically we would expect a sharp wetting layer interface and the Sb concentration would follow an exponential decay. However, we observe a Gaussian distribution due to the intermixing of Sb during the atom probe measurement. Nevertheless, the SK and DE profiles in **Fig. 4.3d** are nearly

identical, and this suggests that the wetting layers in both samples are similar within resolution of the APT measurement. The SK profile does have a high concentration tail at high depths and this is possibly due to the disintegration of capped GaSb quantum dots. It has been suggested by other reports that DE can be used to create GaSb quantum dots in the absence of a wetting layer.[13-18] DE growth without a wetting layer has been demonstrated in the GaAs/AlGaAs system,[19] but this procedure does not with GaSb/GaAs nanostructures. To create nanostructures without a wetting layer, the nanostructure and underlying substrate must share the same group V material. During the initial stages of DE, the substrate becomes terminated with Ga atoms, and in some regions droplets form. When Sb is introduced the Ga terminated surface becomes a 1ML GaSb wetting layer. It has also been demonstrated that the SK quantum dots result in a wetting layer that resembles 1ML of GaSb.[20] As such, it is not surprising that there are such similarities in **Fig. 4.3d.**

4.3.3 Structural Analysis of SK and DE quantum dots

It is known that capped quantum dots may exhibit a distribution of nanostructures of varying morphologies.[9,20] Transmission electron microscopy is used to measure the structure of multiple quantum dots, and select structures can be seen in **Fig. 4.4**. Similar to other reports, we observe that a portion of the SK quantum dots demolish into rings and island clusters. **Figure 4.4a** is a low magnification high angle annular dark field (HAADF) image of the SK sample. In the center of the image a demolished quantum dot and its corresponding clusters is visible. Two additional demolished quantum dot structures are visible on the left and right sides of the image. A horizontal line corresponding to the wetting layer sits just below each of these quantum dots and passes

through the entire image. Four additional contrast lines can be seen directly above the central quantum dot cluster. Two of these lines extend along the ⟨111⟩ from the cluster to the surface. These contrast lines arise from the strain associated with stacking faults originating near the quantum dot clusters.[21]

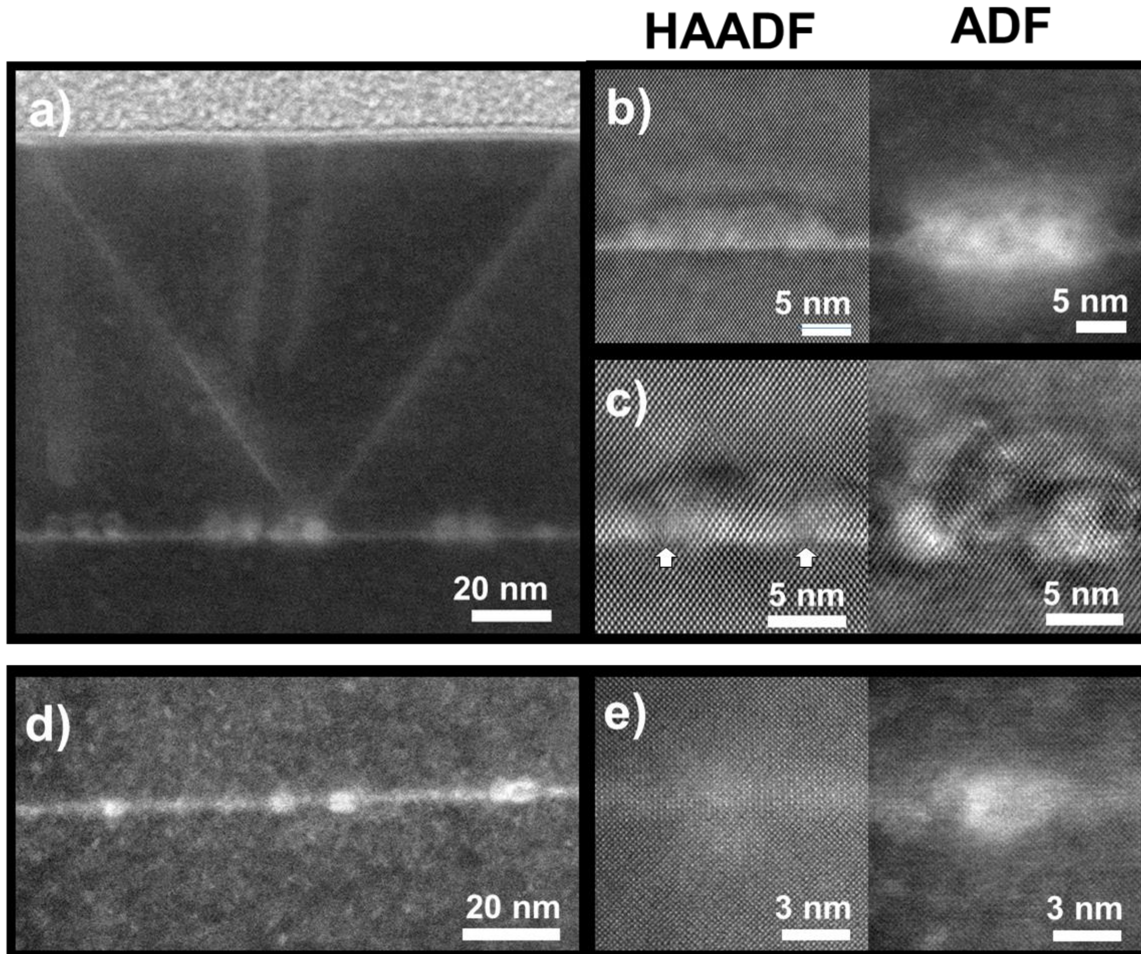

Figure 4.4: TEM images of capped a-c) SK and d-e) DE nanostructures. High resolution images of an b) intact SK dot, a c) defected SK dot and e) DE ring

High magnification high angle annular dark field (HAADF) and annular dark field (ADF) images of a single quantum dot can be seen in **Fig. 4.4b**. The quantum dot is intact and in the HAADF image the truncated pyramid shape is well defined showing that it is 5nm±1nm tall and 25nm±1nm wide, consistent with the AFM measurements (**Fig. 1a**).

The contrast in the HAADF image is from atomic scattering from the larger Sb atoms. Alternatively, the contrast in the ADF image is more influenced by the lattice mismatch strain causing the quantum dot boundaries to be blurry and less defined.

Figure 4.4c shows high magnification HAADF and ADF images of another quantum dot 5nm±1nm tall and 20nm±1nm wide. The perimeter of the quantum dot is clearly defined in the HAADF image, but is obscured by strain in the ADF image, similar to **Fig. 4.4b**. However, unlike **Fig. 4.4b**, two defects, signified by the arrows in the HAADF image. The defects are from the lattice mismatch between the GaSb and the underlying GaAs. These defects significantly impact the ADF image causing severe distortion of the quantum dot features. In combination with the defects present in **Fig. 4.4a**, it is evident that the SK dots may introduce a significant amount of strain in both the capping layer and immediately around the nanostructure. This is consistent with other studies on capped SK GaSb quantum dots.[9,20,22]

Figure 4.4d is a low magnification image of the DE nanostructures and the capping layer. The quantum dots are very consistent in size and shape across the sample and range from 2-3nm in height and 5nm±1nm in diameter, consistent with AFM (**Fig. 4.1b**) and APT (**Fig. 4.3b**) data. A thin wetting layer can be seen between each of the dots. We observe no evidence of defects in the capping layer, but this is not surprising since the dots in the DE sample are short and have a lower Sb concentration than the SK dots. **Figure 4.4e** is high magnification HAADF and ADF images of a single quantum dot. The lower Sb concentration of the DE dot causes less scattering in the HAADF image, making the shape harder to discern. The quantum dot outline can be better seen in the ADF image where the lattice mismatch strain adds to the contrast.

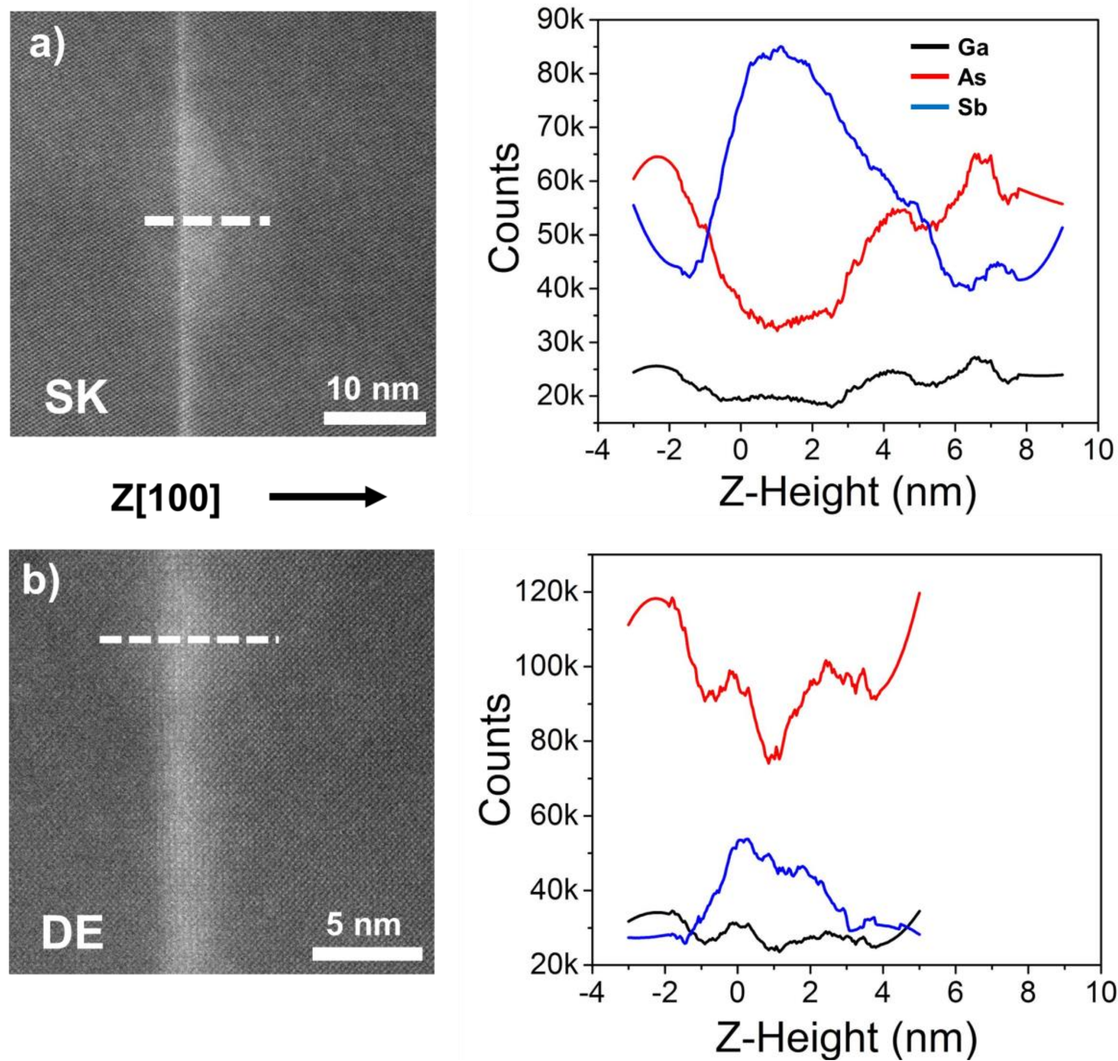

Figure 4.5: EELS analysis of a)SK and b) DE quantum to dots. A TEM image showing the sampling area (dotted line) is included

It has previously been suggested that quantum dots grown by droplet epitaxy may retain elemental Ga within the quantum dot core.[23] To analyze the relative elemental composition of both the SK and DE GaSb quantum dot cores, energy loss spectroscopy (EELS) was used in conjunction with TEM. **Figure 4.5** shows the EELS data of a single quantum dot nanostructure in both the SK (**Fig 4.5a**) and DE (**Fig 4.5b**) samples. The EELS spectrum is collected in the growth direction and outined with the dotted line the

adjacent TEM image of the nanostructure. In the EELS spectrum, the growth interface corresponds to a Z-height of 0nm and each line profile represents the integrated counts of the energy spectrum peaks associated with Ga, As and Sb. The EELS data for the SK sample (**Fig. 4.5a**), taken over 12nm, shows that there is a sharp increase and decrease in Sb and As counts respectively at the growth interface. This is later followed by a gradual decline and increase in Sb and As counts respectively. This response is associated to the SK dot and directly corelates to the nanostructure in the TEM image. While it is expected for there to be a sharp interface in the Sb concentration at the growth interface, we observe a sloped rise due to significant microscope drift that occured during data collection. Nevertheless, the width of the Sb count peak correlates to the height of the SK nanostructures measured by AFM and APT, within error. The maximum Sb concentration is measured at 40±5%. In the DE sample (**Fig 4.5b**) the EELS data is collected over 8nm and we observe a similar rise and decrease in Sb and As counts. The As counts consistently remain greater than the Sb counts across the entire scan range, but the width of the Sb peak also corresponds to the size of the nanostructure as measured by APT and AFM. The maximum Sb concentration is measured at 20±5%. The Sb concentration value is higher than the APT measurements in both the SK and DE sample, but are within error. Because the Ga counts are nominally constant in both the SK and DE samples, it is unlikely this DE dot has an elemental Ga core.

4.3.4 Photoluminescence of SK and DE quantum dots

Figure 4.6 shows photoluminescence data of a single layer of nanostructures grown using SK and DE growth methods. **Figure 4.6a** is a PL spectrum from the SK nanostructures. The spectrum appears as broad emission centered at 1.22eV with two narrow peaks at 1.20eV and 1.14eV. **Figure 4.6b** is a spectrum of DE nanostructures which exhibits emission similar to the SK sample, namely broad emission centered at 1.22eV with narrower peaks at 1.20eV and 1.14eV. In addition, there are two peaks at 1.08eV and 0.98eV. Considering that the broad emission at 1.22eV is present in both SK and DE samples, it likely results from a shared feature. For example, it is possible that the DE quantum dots closely resemble demolished SK quantum dot clusters in size and shape. However, this is unlikely because demolished SK dots exist in a wide range of morphologies whereas the DE dots are consistent across the sample. The similarities between the SK and DE wetting layers in both **Fig. 4.3d** and **Fig. 4.6** strongly suggest that the emission is from wetting layer feature. Broadened emission at 1.22eV **Fig. 4.6** has been reported in other GaSb quantum dot studies and has been attributed to a distribution of quantum dot sizes.[16,24-27] This is unlikely because in the APT (**Fig. 4.2**) and TEM analysis (**Fig. 4.4**), the tall quantum dots in the SK sample are not present in the DE sample. Lastly, a portion of the emission in **Fig. 4.6** could also be from dilute Sb defects in the GaAs matrix.[28]

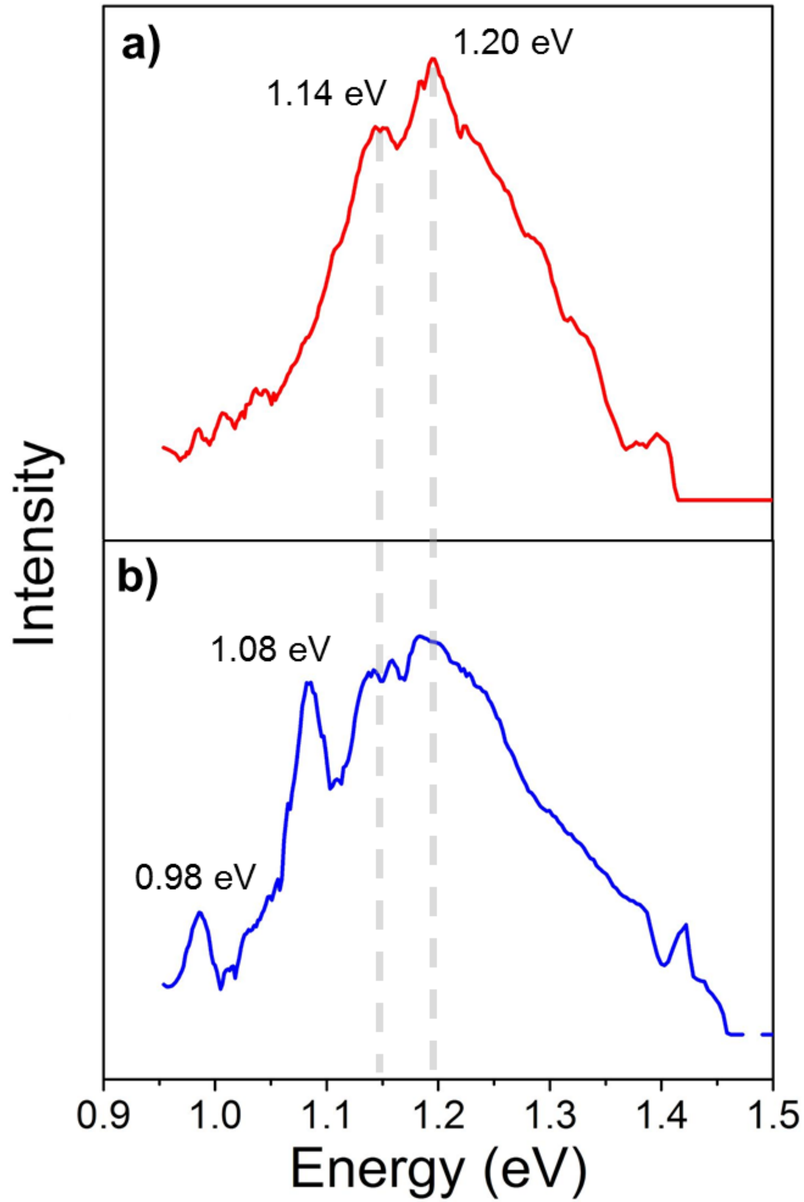

Figure 4.6: Photoluminescence measurements of a) SK quantum dots and b) DE quantum dots with the GaAs substrate peak removed. Measurements were taken at 10K by a 633nm HeNe laser with a spot size of 5 μm and an intensity of 3mW.

Figure 4.7 shows some additional photoluminescence data of droplet epitaxy and SK nanostructures. For these measurements, two samples with quantum dots grown in the exact same manner as in **Fig. 4.1** were fabricated along with an additional droplet epitaxy sample was grown. The new structure is pictured in **Fig. 4.7a** and resemble discs approximately 100±10nm with a central dot approximately 10±1nm. These structure are fabricated by increasing the Sb flux from $2.8x10^{-7}$ to $8.0x10^{-7}$ Torr. **Figure 4.7b** shows the photoluminescence data of the three samples and overlaid on top of each other. Since the spectrums are very similar to each other, light grey drop lines are used to represent the emission from the SK sample. The measurements were done with a 633nm laser and an 850nm filter. The tail of the GaAs peak can be seen at high energies. Similar to **Fig. 4.6** there is emission at 1.2 and 1.14eV. In these measurements there are no additional peaks at higher energies in the droplet epitaxy sample. The data in **Fig. 4.7** demonstrates that his emission is reproducible and consistent with yet another nanostructure morphology. This further supports the suggestion that the emission is from a shared feature such as the wetting layer.

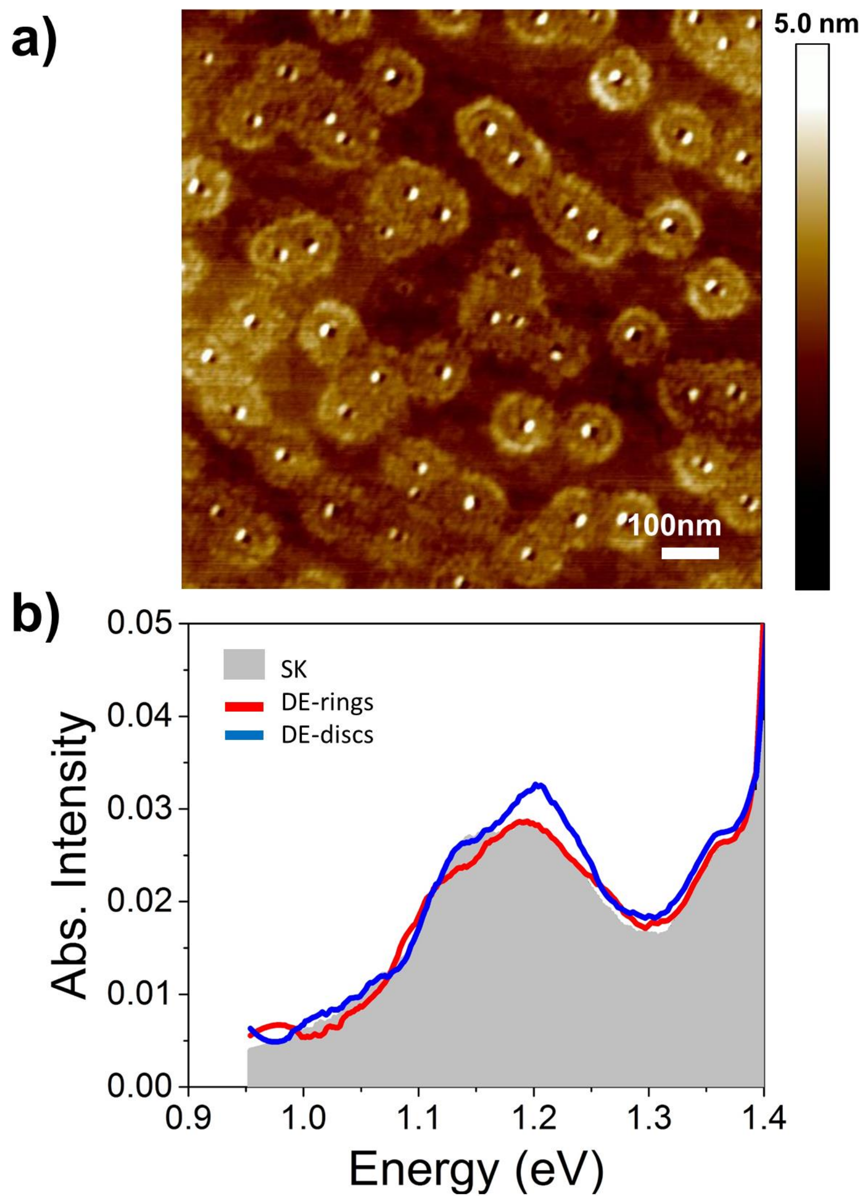

Figure 4.7: a) AFM image showing GaSb Discs grown by droplet epitaxy and b) Photolumminescence measurements of SK dots, DE rings, and DE disks. Measurements were taken in the same manner as Figure 4.6

4.4 Conclusions

In summary, we present on the composition, structure, and optical characteristics of GaSb nanostructures grown by the Stranski-Krastanov and droplet epitaxy growth mechanisms. GaSb ring structures grown by DE are proven to more closely resemble GaSb dots because of the Sb concentration distribution. This indicates DE growth causes heavy As intermixing to occur. The final nanostructure has a much lower Sb concentration than SK dots, but do have increased isotropy. This leads to less strain and prevents defects from forming during capping. EELS measurements indicate that there is no liquid Ga core in the DE dots. Furthermore, the similarities between the SK and DE photoluminescence spectrums suggest that only the wetting layer is emitting.

4.5 GaSb Quantum Dot Motivations and Applications

GaSb exhibits a type II-band offset with GaAs, meaning GaSb quantum dots will confine holes within a potential well, but not electrons. This creates a spatial separation of the electron-hole pair which lengthens recombination time and improves carrier collection.[1] Due to how sensitive quantum confinement effects are to nanostructure size, the ability to control the shape, size, and concentration of GaSb is vital for design of numerous next generation electronic devices, including photovoltaics,[29] charge based memory,[5] quantum computing,[30] and even light emission. For high efficiency photovoltaic applications, specifically intermediate band designs, GaSb quantum dots are embedded in GaAs. Multiple quantum dots are aligned within the GaAs matrix and interact with each other form an intermediate band state within the band gap. This enables the solar cell to more efficiently capture incident infrared photons. Theoretically, intermediate band solar cells will maximize current by absorbing more photons while maintaining the higher

potential of the matrix material.[ref] The quality of this intermediate band is determined in part by the quantum dot shape, position, and uniformity.[ref] Another application of GaSb quantum dots are quantum based memory applications.[ref] In traditional charge based memory, a floating gate is charged and acts as a method of storing information. An SiO_2 layer acts as a 3.2eV energy barrier and the information can be stored upwards of 10 years. However, one drawback of this design is the relatively slow read and write times. This can be improved using III-V quantum dots because of the ability to adjust the energy barrier height through modification of the nanostructure size. The lifetime of stored information would depend on the carrier lifetime within the quantum dots. Due to the type II band alignment and hole confinement, GaSb/GaAs quantum dots can exhibit long storage times, with measured values at 1.6s at room temperature.

4.6 References

1. Hatami, F., Ledentsov, N. N., Grundmann, M., Böhrer, J., Heinrichsdorff, F., Beer, M., ... & Heydenreich, J. (1995). Radiative recombination in type-II GaSb/GaAs quantum dots. *Applied physics letters*, *67*(5), 656-658.
2. Hatami, F., Grundmann, M., Ledentsov, N. N., Heinrichsdorff, F., Heitz, R., Böhrer, J., ... & Kop'ev, P. S. (1998). Carrier dynamics in type-II GaSb/GaAs quantum dots. *Physical Review B*, *57*(8), 4635.
3. Laghumavarapu, R. B., Moscho, A., Khoshakhlagh, A., El-Emawy, M., Lester, L. F., & Huffaker, D. L. (2007). GaSb⁄GaAs type II quantum dot solar cells for enhanced infrared spectral response. *Applied Physics Letters*, *90*(17), 173125.
4. Mano, T., Kuroda, T., Mitsuishi, K., Yamagiwa, M., Guo, X. J., Furuya, K., ... & Koguchi, N. (2007). Ring-shaped GaAs quantum dot laser grown by droplet epitaxy: effects of post-growth annealing on structural and optical properties. *Journal of Crystal Growth*, *301*, 740-743.
5. Marent, A., Geller, M., Schliwa, A., Feise, D., Pötschke, K., Bimberg, D., ... & Öncan, N. (2007). 106years extrapolated hole storage time in GaSb⁄AlAs quantum dots. *Applied Physics Letters*, *91*(24), 242109.
6. Loss, D., & DiVincenzo, D. P. (1998). Quantum computation with quantum dots. *Physical Review A*, *57*(1), 120.
7. Kobayashi, S., Jiang, C., Kawazu, T., & Sakaki, H. (2004). Self-assembled growth of GaSb type II quantum ring structures. *Japanese journal of applied physics*, *43*(5B), L662.

8. Tatebayashi, J., Khoshakhlagh, A., Huang, S. H., Dawson, L. R., Balakrishnan, G., & Huffaker, D. L. (2006). Formation and optical characteristics of strain-relieved and densely stacked GaSb∕GaAs quantum dots. *Applied physics letters*, *89*(20), 203116.
9. Smakman, E. P., Garleff, J. K., Young, R. J., Hayne, M., Rambabu, P., & Koenraad, P. M. (2012). GaSb/GaAs quantum dot formation and demolition studied with cross-sectional scanning tunneling microscopy. *Applied Physics Letters*, *100*(14), 142116.
10. Jo, M., Mano, T., Sakuma, Y., & Sakoda, K. (2012). Extremely high-density GaAs quantum dots grown by droplet epitaxy. *Applied Physics Letters*, *100*(21), 212113.
11. DeJarld, M., Reyes, K., Smereka, P., & Millunchick, J. M. (2013). Mechanisms of ring and island formation in lattice mismatched droplet epitaxy. *Applied Physics Letters*, *102*(13), 133107.
12. Mano, T., & Koguchi, N. (2005). Nanometer-scale GaAs ring structure grown by droplet epitaxy. *Journal of crystal growth*, *278*(1), 108-112.
13. Kawazu, T., Mano, T., Noda, T., Akiyama, Y., & Sakaki, H. (2009). Growth of GaSb dots on GaAs (100) by droplet epitaxy. *physica status solidi (b)*, *246*(4), 733-735.
14. Kawazu, T., Noda, T., Mano, T., Sakuma, Y., & Sakaki, H. (2015). Growth and optical properties of GaSb/GaAs type-II quantum dots with and without wetting layer. *Japanese Journal of Applied Physics*, *54*(4S), 04DH01.
15. Kawazu, T., Mano, T., Noda, T., & Sakaki, H. (2010). Thermal annealing of GaSb quantum dots in GaAs formed by droplet epitaxy. *Physica E: Low-dimensional Systems and Nanostructures*, *42*(10), 2742-2744.

16. Kawazu, T., Noda, T., Mano, T., Sakuma, Y., & Sakaki, H. (2013). Post-growth annealing of GaSb quantum dots in GaAs formed by droplet epitaxy. *physica status solidi (c)*, *10*(11), 1505-1508.

17. Kawazu, T., Noda, T., Sakuma, Y., & Sakaki, H. (2016). Excitation power dependence of photoluminescence spectra of GaSb type-II quantum dots in GaAs grown by droplet epitaxy. *AIP Advances*, *6*(4), 045312.

18. Kawazu, T., Noda, T., Mano, T., Jo, M., & Sakaki, H. (2010). Effects of Antimony Flux on Morphology and Photoluminescence Spectra of GaSb Quantum Dots Formed on GaAs by Droplet Epitaxy. *Journal of Nonlinear Optical Physics & Materials*, *19*(04), 819-826.

19. Sanguinetti, S., Watanabe, K., Tateno, T., Gurioli, M., Werner, P., Wakaki, M., & Koguchi, N. (2003). Modified droplet epitaxy GaAs/AlGaAs quantum dots grown on a variable thickness wetting layer. *Journal of crystal growth*, *253*(1), 71-76.

20. Martin, A. J., Hunter, A. H., Saucer, T. W., Sih, V., Marquis, E. A., & Millunchick, J. (2013). Atom probe tomography analysis of different modes of Sb intermixing in GaSb quantum dots and wells. *Applied Physics Letters*, *103*(12), 122102.

21. Sears, K., Wong-Leung, J., Tan, H. H., & Jagadish, C. (2006). A transmission electron microscopy study of defects formed through the capping layer of self-assembled InAs⁄GaAs quantum dot samples. *Journal of applied physics*, *99*(11), 113503.

22. Kamarudin, M. A., Hayne, M., Zhuang, Q. D., Kolosov, O., Nuytten, T., Moshchalkov, V. V., & Dinelli, F. (2010). GaSb quantum dot morphology for different

growth temperatures and the dissolution effect of the GaAs capping layer. *Journal of Physics D: Applied Physics*, *43*(6), 065402.

23. Reyes, K., Smereka, P., Nothern, D., Millunchick, J. M., Bietti, S., Somaschini, C., ... & Frigeri, C. (2013). Unified model of droplet epitaxy for compound semiconductor nanostructures: experiments and theory. *Physical Review B*, *87*(16), 165406.
24. Nowozin, T., Marent, A., Bonato, L., Schliwa, A., Bimberg, D., Smakman, E. P., ... & Hayne, M. (2012). Linking structural and electronic properties of high-purity self-assembled GaSb/GaAs quantum dots. *Physical review b*, *86*(3), 035305.
25. Müller-Kirsch, L., Heitz, R., Schliwa, A., Stier, O., Bimberg, D., Kirmse, H., & Neumann, W. (2001). Many-particle effects in type II quantum dots. *Applied Physics Letters*, *78*(10), 1418-1420.
26. Suzuki, K., Hogg, R. A., & Arakawa, Y. (1999). Structural and optical properties of type II GaSb/GaAs self-assembled quantum dots grown by molecular beam epitaxy. *Journal of applied physics*, *85*(12), 8349-8352.
27. Kawazu, T., Noda, T., Mano, T., Sakuma, Y., & Sakaki, H. (2013). Growth of GaSb quantum dots on GaAs (311) A. *Journal of Crystal Growth*, *378*, 475-479.
28. Cheah, W. K., Fan, W. J., Yoon, S. F., Tan, K. H., Liu, R., & Wee, A. T. S. (2005). Surfactant and impurity properties of antimony on GaAs and GaAs 1− x N x on GaAs [100] by solid source molecular beam epitaxy. *Thin solid films*, *488*(1), 56-61.
29. Hwang, J., Martin, A. J., Millunchick, J. M., & Phillips, J. D. (2012). Thermal emission in type-II GaSb/GaAs quantum dots and prospects for intermediate band solar energy conversion. *Journal of Applied Physics*, *111*(7), 074514.

30. Kroutvar, M., Ducommun, Y., Heiss, D., Bichler, M., Schuh, D., Abstreiter, G., & Finley, J. J. (2004). Optically programmable electron spin memory using semiconductor quantum dots. *Nature*, *432*(7013), 81-84.
31. Lin, S. Y., Tseng, C. C., Lin, W. H., Mai, S. C., Wu, S. Y., Chen, S. H., & Chyi, J. I. (2010). Room-temperature operation type-II GaSb/GaAs quantum-dot infrared light-emitting diode. *Applied physics letters*, *96*(12), 123503.

Chapter 5
GaAs Nanowires for on-chip optoelectronic device integration

High quality GaAs nanowire growth is demonstrated on polycrystalline films at temperatures of 400°C. Undoped, Si-doped, and Be-doped nanowires were grown at T_s=400°C on oxide (indium tin oxide) and metallic (platinum and titanium) films. Be doping is shown to significantly reduce the nanowire diameter and improve the nanowire aspect ratio to 50:1. Photoluminescence measurements of Be doped nanowires are 1-2 orders of magnitude stronger than undoped and Si-doped nanowires and have thermal activation energies of 14meV, which is comparable to nanowires grown on crystalline substrates. Electrical measurements confirm that the metal-semiconductor junction is Ohmic. Changing the doping element during growth allows the growth of core-shell nanowire structures. These results demonstrate the feasibility of integrating nanowire-based optoelectronic devices directly on CMOS chips.

5.1 Introduction

Wireless sensor networks are the backbone of the evolving system of interconnected commercialized devices known as the Internet of Things.[1] These networks are comprised of low power sensor nodes utilized in smart appliances, environmental monitors, and implantable biomedical devices.[2-4] Millimeter scale sensors have already

demonstrated energy-autonomous operation using photovoltaic cells in conjunction with both solar[5-7] and indoor lighting.[8] Incorporation of optoelectronic devices into wireless sensor nodes is currently achieved externally by wire bonding separate components into a stacked unit.[5,9] Integrating silicon CMOS and III-V optoelectronic devices as a single component would eliminate the need for wire bonding and decrease the thickness. Material incompatibility, especially between the Si-based logic circuits and the GaAs-based optoelectronics, limits this approach due to defects formed between dissimilar materials.[10,11] There has been some success using lattice engineered substrates,[12] flip-chip[13] and fluidic self-assembly methods,[14] but the amount of processing and thus the cost required for these techniques is excessive for most applications.

This study attempts to integrate these devices by using self-assembled GaAs nanostructures. Nanowires will act as the active region of the optoelectronic device and will be grown directly on the surface of the pre-packaged sensor. The nanowires can be grown on either an exposed metal pad, or subsequently deposited conducting films. It has already been demonstrated that nanowires can be used to create light emitting diodes[15-19] and solar cells with a fraction of the material.[20-24] To enable on-chip nanowire growth, sufficiently high quality nanowires have to be deposited directly on polycrystalline conductive layers at temperatures at or below 450°C to prevent degradation of metallic interconnects.[25] GaN nanowire LEDs have been grown on metallic films with great success but requires substrate temperatures of 800°C.[26,27] GaAs nanowire growth by vapor deposition has previously been demonstrated on polycrystalline films with mixed results.[28-31] In some reports the nanowires have a high aspect ratio with full surface coverage, but in others the nanowires are sparse and misshapen. Here we present on

the growth of GaAs nanowires on polycrystalline conducting films at 400°C. We investigate the impact of doping and growth rate on the nanowire density and morphology. We find that the structural and optoelectronic quality can be improved with Be dopants. Be doped nanowires have a high aspect ratio (50:1), a reduced number of stacking faults, and strong room temperature photoluminescence. Switching doping elements during growth demonstrates control over axial and sidewall nanowire growth, enabling core-shell nanowire formation. This study presents a significant step forward towards the direct integration of III-V devices on CMOS technology.

5.2 Experimental Methods

Three polycrystalline films were examined as substrate candidates, indium tin oxide, platinum, and titanium. For the samples with ITO films, oxide-free p-doped silicon substrates were coated with 100 nm of ITO at room temperature at rate of 1.8 A/s with 40sccm Ar and 1sccm O_2 at 139W of DC power. For samples with Pt films, Pt/TiO/Si/SiO_2 substrates were purchased from Radiant Technologies. For samples with Ti films, 4nm of titanium was e-beam deposited on oxide-free Si wafers using an Enerjet system.

Each substrate was coated with a thin film of Au to act as the catalyst necessary for nanowire growth. For both ITO and Pt films, 5nm of Au was sputter coated at room temperature under 5 mTorr vacuum for 16s with the Ar plasma at 18V. For the Ti film, 5nm of Au was deposited using e-beam deposition immediately after Ti deposition. This both prevents Ti oxidation and acts as the catalyst for nanowire growth.

The GaAs nanowires are grown using a solid source molecular beam epitaxy chamber and the well-known Vapor-Liquid-Solid (VLS) mechanism.[32] GaAs growth

without an Au catalyst resulted in the growth of a rough film and no nanowires. Samples were heated to 400°C, after which they were exposed to an As_4 flux. The growth temperature was found by heating sensors containing wire-bonded stacks of Si devices developed by Blaauw et al.[5-7] in the chamber to find an upper limit before device failure. These samples were heated to 300, 400, and 500°C and annealed for 30 minutes and removed. Devices annealed to 500°C exhibited open circuit responses whereas samples heated to 400°C and 300°C remained functional, consistent with other CMOS temperature studies.[25] Thus, all subsequent nanowire growths were conducted at substrate temperatures of 400°C, and to initiate growth, Ga was introduced at a rate either 0.8 or 1.3 monolayers/second (ML/s). The ratio of As_4/Ga beam equivalent pressures was 10 in all growths. Growth times varied between $5 \leq t \leq 60$ minutes. Si and Be elemental sources were used as n and p type dopants as indicated, using fluxes that result in doping concentrations of $4x10^{19}/cm^3$ in planar GaAs films.

5.3 Data Analysis

5.3.1 Growth on Polycrystalline films

Initial studies were performed on conducting oxides, specifically indium tin oxide (ITO), a conductive oxide widely used as a top contact in photovoltaic applications due to its transparency. **Figure 5.1a-c** shows scanning electron microscope (SEM) images of nanowires grown on indium tin oxide (ITO) and show that nanowires form a dense forest with orientations in many different directions. The nanowires are heavily tapered and often end in a sharp point. This type of tapered morphology is also seen in GaAs nanowires grown on crystalline substrates.[33,34] **Figure 5.1b** is a cross sectional image of the sample in **Fig. 5.1a**. From this image it is clear that the majority of nanowires extends in a direction not parallel to the surface normal. Also, the nanowires are not all the same length, with there being a higher density of short and thin nanowires near the GaAs/ITO interface. A high magnification image of the GaAs-ITO interface (indicated by the dotted yellow line) is seen in **Fig. 5.1c** and a layer of continuous GaAs, confirmed by energy dispersive electron X-ray spectroscopy, can be seen at the base of the nanowires. In all of the samples measured both nanowires and the continuous film are present. Similar growths were done on the silicon dioxide layer on the backside of the Pt samples and the results were identical.

a

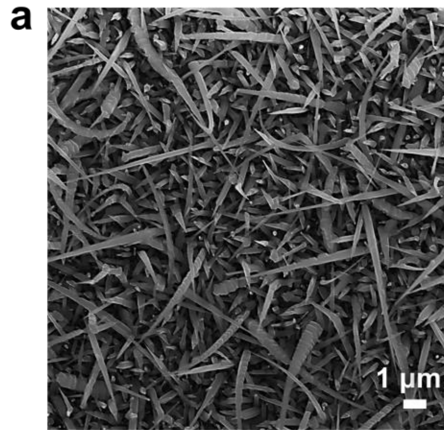

b

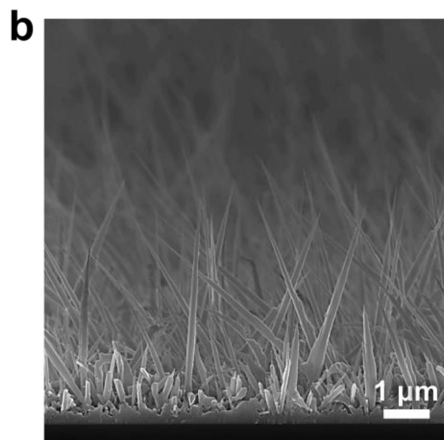

c

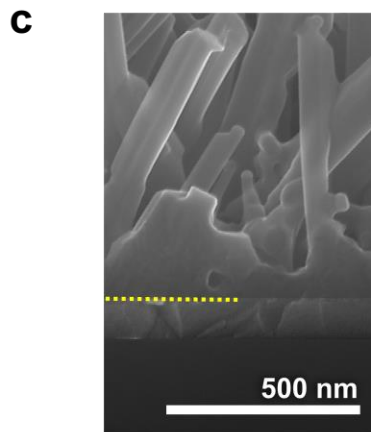

Figure 5.1*:* a) Top down and b) cross sectional scanning electron microscope (SEM) images of GaAs nanowires grown on indium tin oxide (ITO) for 30 minutes. c) High magnification SEM image of the GaAs-ITO interface, with the interface between the ITO and GaAs (dotted line) indicated.

The variation in nanowire orientation exhibited in **Fig. 5.1** may be caused by epitaxial or random nucleation. An epitaxial relationship between the polycrystalline ITO and GaAs is improbable given the 79% lattice mismatch between them.[35,36] Rather, the nanowire growth is likely initiated by random nucleation events at the catalyst-film interface. As such, the orientation of the fastest growing crystalline direction, in this case the c-plane of wurzite GaAs, would depend on the orientation of the nuclei with respect to the interface normal. Initially the orientation of the nanowires is expected to be mostly random with respect to the substrate normal and is responsible for the variation in nanowire heights in **Fig. 5.1b.** As the nanowires continue to increase in length, those having orientations far away from the surface normal will tend to terminate either by impinging on, or becoming shadowed by other nanowires. Collisions with growing nanowires can be seen clearly in **Fig. 5.1c.** This explains why there are very thin and short nanowires closer to the substrate. The tapering observed in **Fig. 5.1** is likely from a combination of sidewall growth and a shrinking catalyst, which are both well-documented phenomena in molecular beam epitaxy nanowire growth.[37-42]

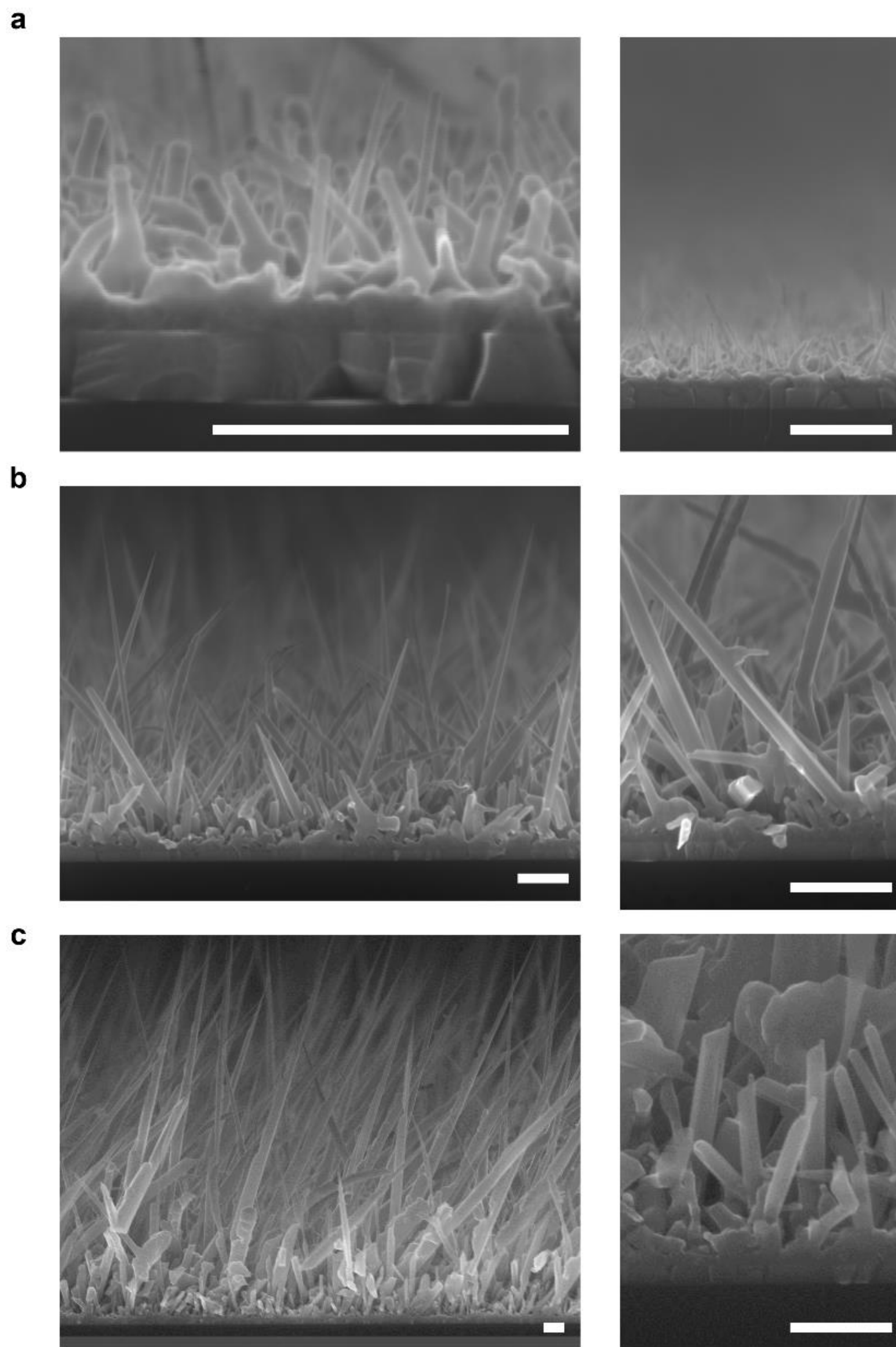

Figure 5.2: Cross-sectional SEM micrographs of Nanowires grown on ITO after a) 5 min, b) 20 minutes, and c) 60 minutes. All scale bars are 500nm.

Figure 5.2 shows the evolution of nanowire growth as a function of deposition time. The left half of the figure shows a cross section of the overall morphology of the nanowires, while the right half shows higher resolution images of the ITO-nanowire interface. For deposition time of 5 minutes (**Fig. 5.2a**), the nanowires are 170 ± 30nm tall and the Au catalysts can easily be seen at their apex. The height variations are likely due to individual factors such as fluctuations in catalyst size and orientation. A continuous GaAs film can be seen very clearly, similar to **Fig. 5.1c.** After 20 minutes of growth (**Fig. 5.2b**), the average height increases to 1.0 ± 0.3 μm. There is a large amount of small nanowires near the substrate, likely caused by termination events. Nanowire tapering is also much more apparent. After 60 minutes of growth (**Fig. 5.2c**), the height increases to 8±1μm, and their density is high. Almost all of the nanowires are tapered and have irregular sidewalls. Compared to **Fig. 5.2a** and **Fig. 5.2b,** the nanowires are oriented in a similar direction, with all of the nanowires pointing towards the left. When comparing each of the growths at the same magnification, short nanowires of similar heights are visible in all samples.

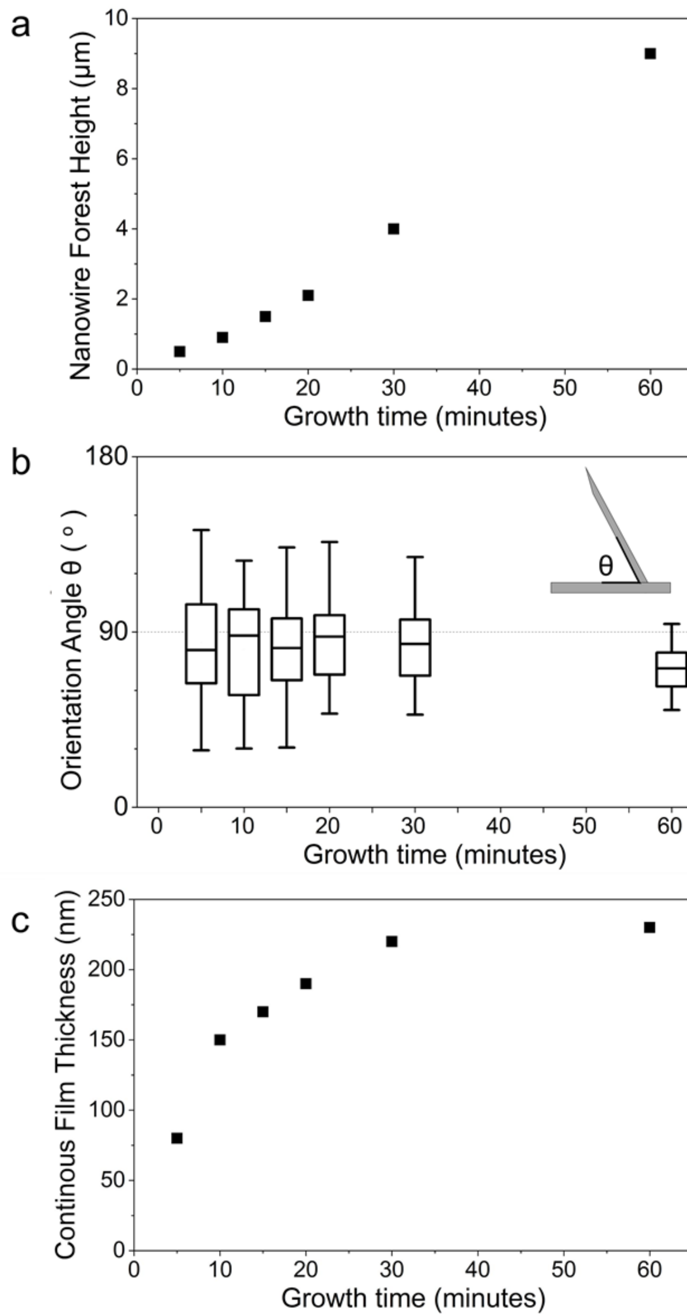

Figure 5.3: Statistical measurements of nanowire samples grown on ITO with growth times between 5 and 60 minutes. a) Nanowire forest height, b) nanowire orientation angle and the c) continuous film thickness are measured.

A more statistical analysis of the growths in **Fig. 5.2** including additional growths is provided in **Fig. 5.3. Figure 5.3** plots the nanowire forest height, nanowire orientation, and continuous layer thickness of GaAs nanowires grown on ITO as a function of growth time. The forest height is defined as the upper limit of the perpendicular distance between the nanowire tip and the substrate. It has a strong positive linear correlation to the growth time (R^2 = 0.992), as would be expected. **Figure 5.3b** is a box and whisker plot showing the distribution of the orientation between the nanowires and the underlying substrate. A minimum of thirty nanowires were measured on each sample. The range (denoted by the error bars) of the distribution decreases with deposition time, consistent with the fact that orientations far away from the surface normal (θ=90°) impinge on other nanowires or are shadowed by tilted nanowires. The interquartile range (denoted by the box) also decreases with deposition time, signifying a reduction in nanowire angle variation. After an hour of growth, the median nanowire orientation converges towards an angle of ~70°. This convergence is somewhat surprising, because if all near-normal orientations were equally possible, the distribution should center around 90°. However, an angled orientation presents a larger capture surface for the impinging flux allowing tilted nanowires to grow faster. This is seen in **Fig. 5.2c** in which all of the nanowires are orientated toward the left.

Figure 5.3c shows the thickness of the continuous film under the nanowires as a function of growth time. The film thickness increases with growth time and saturates at a thickness of 230nm. This behavior suggests that the continuous film is not a precursor to nanowire growth, but a competitive process. During deposition a portion of the flux is

incorporated into the continuous layer. As the nanowires get longer, the impinging flux is captured by the nanowires as opposed to reaching the continuous layer below.

5.3.2 Doping and Nanowire Formation

Doping of GaAs is a necessary step in the formation of optoelectronic devices. Si and Be dopants were used for n and p type GaAs respectively. **Figure 5.4** shows the effect of incorporating dopants into the growth of nanowires on ITO. For these growths, GaAs was deposited for 15 minutes. **Figure 5.4a** is an SEM image of undoped GaAs nanowires provided for comparison purposes. Similar to **Fig. 5.1**, the nanowires are randomly oriented and heavily tapered. The overall morphology of Si-doped nanowires (**Fig. 5.4b**) is similar to the undoped wires, except that some nanowires are curved with rough sidewalls (indicated in **Fig. 5.4b** with arrows). Because they consistently curve towards the surface, it is likely that this curvature arises due to the fact that the sidewall facing the impinging flux grows more quickly than the opposite sidewall. It is known that Si doping decreases both the Si and Ga vacancy diffusion coefficient in bulk GaAs.[43,44] It has been demonstrated that dopant incorporation during nanowire growth is dominated by diffusion on the sidewalls as opposed to dissolution within the catalyst.[45] Thus, any dopant effects would be observed on the outer surface of the nanowires, meaning Si-doping would reduce diffusion along the sidewalls and promote lateral growth of the nanowires. The gold catalyst is not visible on any of the Si doped nanowires. The catalyst may have migrated from the apex of the nanowire, contributing to the tapered morphology. This type of catalyst migration has also been observed in other nanowire growths.[37,38]

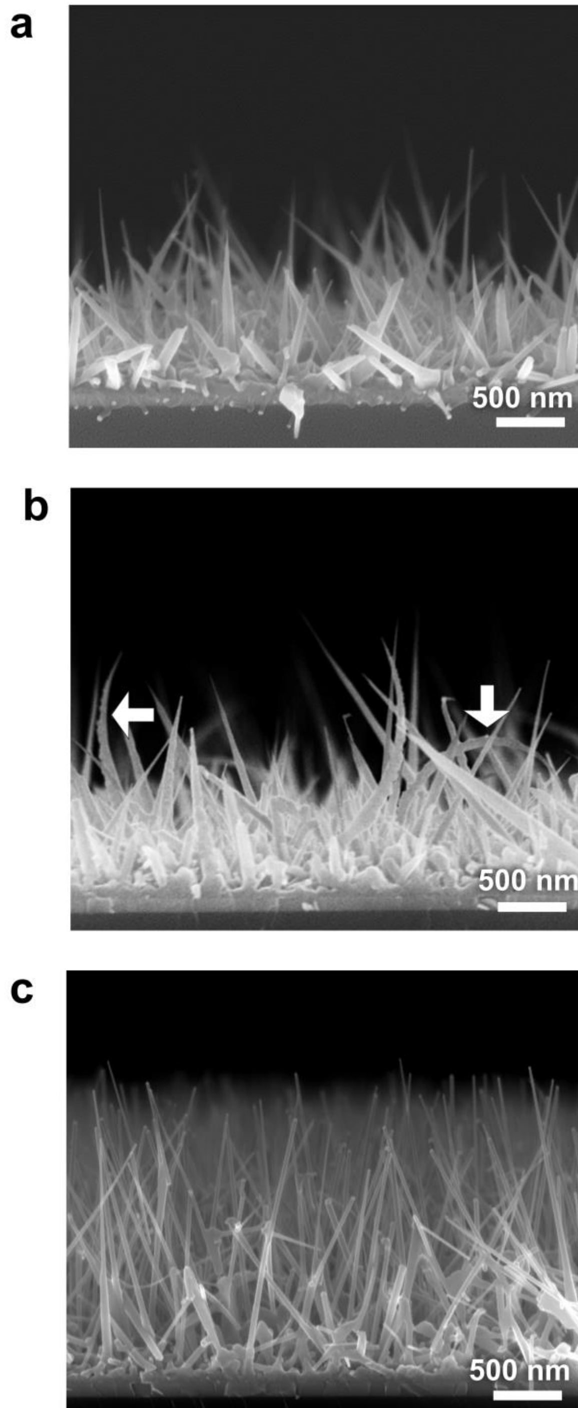

Figure 5.4: Cross-sectional SEM images of GaAs nanowires grown on ITO for 15 minutes with a) no doping, b) Si doping, and c) Be doping.

Figure 5.4c shows GaAs nanowires doped with Be. Be-doping leads to an increase in nanowire density, a reduction in nanowire diameter, and a 60% increase in nanowire forest height (to 2.2±0.2μm). These nanowires are less tapered, and tend to be oriented closer to 90°. We propose that the Be dopant may have a surfactant effect on the nanowire sidewalls, improving the diffusion of Ga and As. This behavior has been observed for sulfur atoms during the growth of GaSb nanowires.[46] Alternatively, Be may be preventing the migration of the Au catalyst, as suggested by the near-constant diameter of the nanowire along its length. Both of these effects could explain the changes in morphology observed between **Fig. 5.4a** and **Fig. 5.4c.**

5.3.3 Structural and Optical Characteristics of Doped Nanowires

Undoped and Be-doped nanowires are measured for their structural integrity with a transmission electron microscope (TEM) measurements. The measurements, presented in **Fig. 5.5** show that the microstructure of the nanowires varies with doping. The TEM samples are made by removing the nanowires from the substrate and dispersing them on a grid. **Figure 5.5a** is a collection of transmission electron microscope images used to form a single image of an undoped nanowire. The nanowire has very rough sidewalls, evidence of stacking faults, tapering, and ends in a sharp point. There is no evidence of the Au catalyst in this or other undoped nanowires. **Figure 5.5b** is a high resolution image of the same nanowire, and confirms the presence of multiple stacking faults and rough sidewalls. These observations are consistent with prior reports of the consequences of Au-migration, namely roughened sidewalls and tapering.[37] The observed nanowire morphology may also be due to the low temperatures of these growths, which is also known to induce tapering.[47-49] The corresponding diffraction pattern

demonstrates that the crystalline structure is wurtzite which is expected in GaAs nanowires.[50]

Figure 5.5c shows a low resolution TEM image of a single Si doped nanowire. The nanowire is curved and the catalyst cannot be seen at the tip of nanowire. The sidewalls are uneven and there are regions with different widths. **Figure 5.5d** is a high resolution image of the same nanowire. This image confirms the rough surfaces at the sidewalls of the nanowire. Included in this image are a series of stacking faults. Regions such as these are common throughout the length of the nanowire, but there are less than the undoped nanowire. The crystal orientation of this nanowire was also wurtzite as indicated by the diffraction pattern.

Figure 5.5e is a low resolution image of single Be doped nanowire clearly showing the Au catalyst at the nanowire tip. Furthermore, the sidewalls appear smooth and the diameter unchanging along the length of the nanowire, providing further evidence that Be inhibits migration of the catalyst. **Figure 5.5f** is a high resolution image of a single Be doped nanowire and its corresponding diffraction pattern. A few stacking faults are visible in this image, and the sidewalls are smooth. As with the undoped nanowire, the diffraction pattern indicates that the crystal structure is wurtzite. The stark differences between **Fig. 5.5b** and **Fig. 5.5f** confirms that along with an improved morphology **Fig. 5.4**, Be-doping also corresponds to an improved crystal structure.

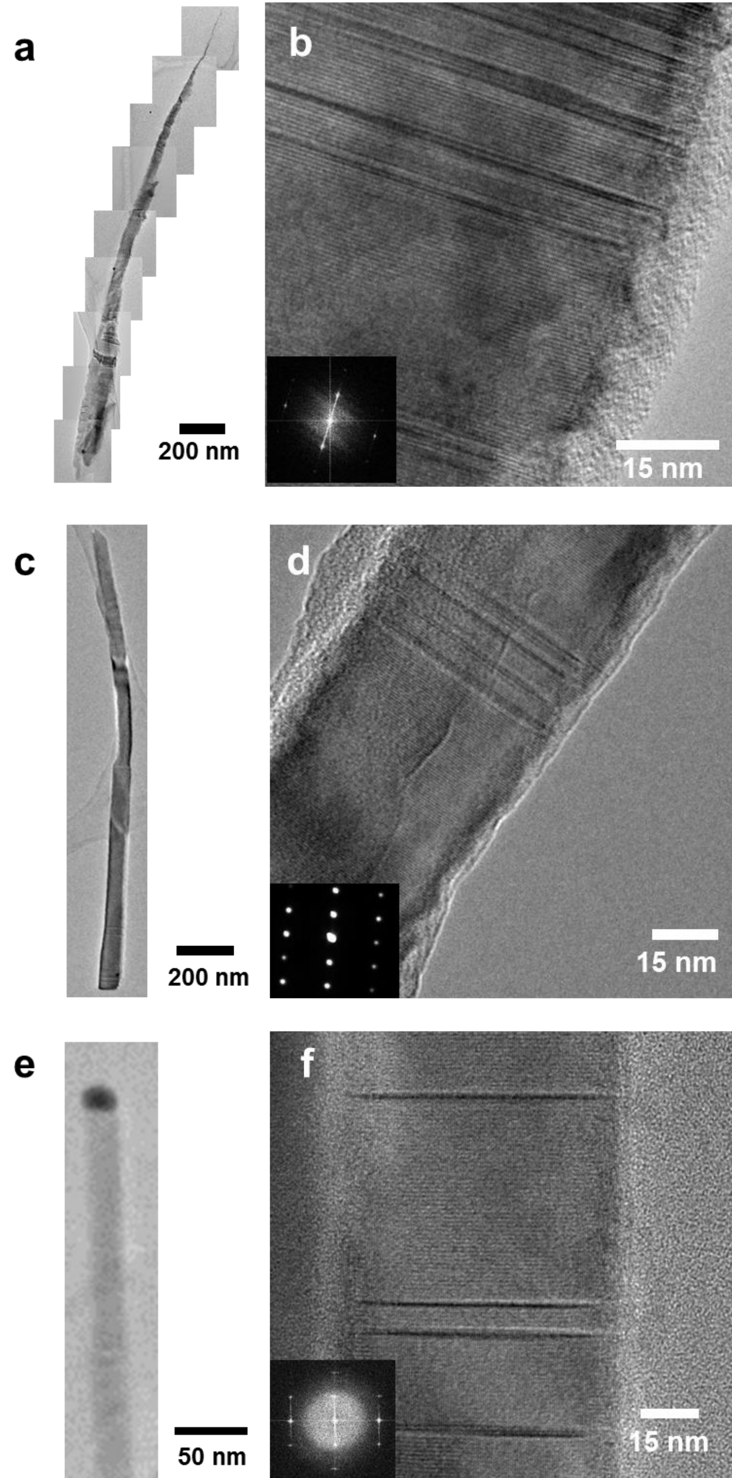

Figure 5.5: Transmission Electron Microscope images and diffraction patterns of a-b) undoped, c-d) Si doped, and e-f) Be doped GaAs nanowires grown on ITO.

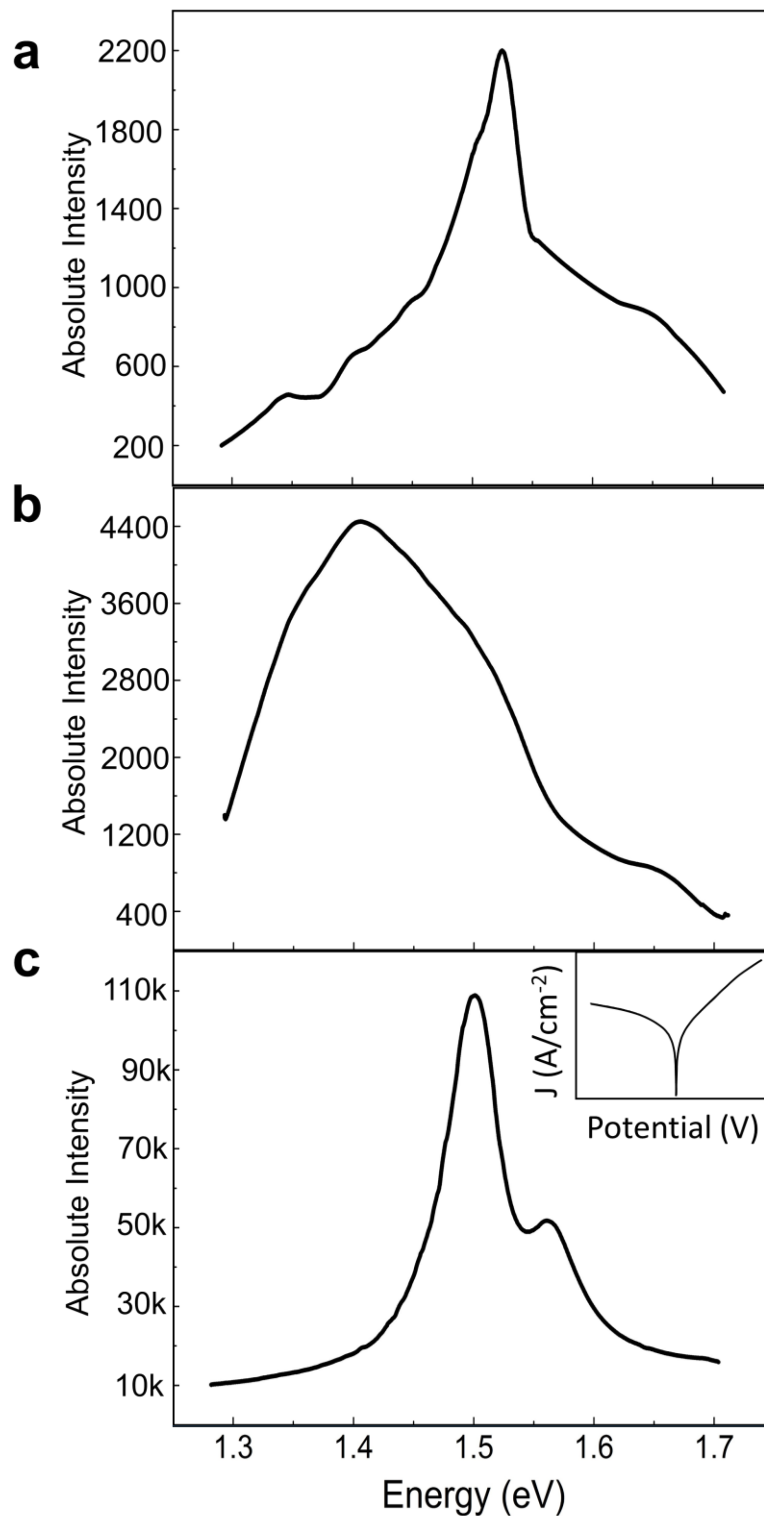

Figure 5.6: Photoluminescence data of nanowires grown on ITO with a) no doping, b) Si doping, and c) Be doping. (inset) Current Density vs Electrical Potential of Be doped nanowires.

Photoluminescence measurements of the samples in **Fig. 5.4** were carried out at 10K with a 633nm HeNe laser with an output power of 1mW and a spot size of 5um^2. The nanowire forests were still attached to the Si-ITO substrate which was mounted to a cold finger. Absolute intensity values are provided, and for comparison bulk GaAs provided 5x10^6 counts (not pictured) with a similar setup. The undoped nanowires (**Fig. 5.6a**) have weak peak response at 1.52eV (FWHM= 45 meV) superimposed on less intense broad emission. The position of 1.52 eV is expected for GaAs at 10K, but the cause of the broad background emission is not clear. The Si doped nanowires emit a slightly stronger response at 1.41 eV (FWHM= 210 meV) (**Fig. 5.6b**). The peak is fairly broad and at energies lower than expected for GaAs. It may be emission from a radiative defect caused by either Si or GaAs, but emission in this range has previously been attributed to zinc-blende and wurtzite heterojunctions within GaAs nanowires.[51] Comparatively, Be doped nanowires have an optical response that is approximately 25 times stronger, with a major peak at 1.50eV (FWHM=41 meV) and a secondary peak that is 20% as intense at 1.57 eV (FWHM=31 meV) (**Fig. 5.6c**). The 20 meV redshift of the primary peak likely corresponds to the Be doping level and is consistent with other published PL measurements of Be-doped GaAs.[52] The secondary peak at 1.57 eV could either be the result of quantum confinement or a Burstein-Moss effect.[53-56] In order for this 70 meV blue shift to arise from quantum confinement, the nanowires would have to be on the order of 10 nm in diameter. While the diameter average of the nanowires in these samples is 40±10 nm, there is a small population of nanowires less than 15nm in diameter. On the other hand, in order for the blue shift to arise from the Burstein-Moss effect, the doping concentration would have to be approximately 9.2x10^{19} cm^{-3}. It is difficult to quantify the

dopant incorporation into the nanostructures, but based on planar measurements using the same doping flux, a Burstein-Moss related blue shift feasible.

From **Fig 5.4-5.6,** it is clear that the Be doped nanowires are superior in morphological, structural, and optical quality. To examine the capabilities of the nanowire-ITO interface at transmitting current electrical testing was performed. For this the GaAs nanowires were backfilled with parylene, followed by the e-beam deposition of 10nm of Ti and 100nm of Au to act as a top contact. To ensure a strong connection between the nanowires and the top contact, the sample was annealed at 300°C for 1 minute and without this step there is an open circuit. A bottom contact was formed similarly on the backside of the Si wafer. **The inset in Fig. 5.6c** shows IV measurements of Be doped nanowires on ITO. The asymmetry in the IV curve at positive and negative voltages presented in **Fig. 6c** signifies a Schottky contact. This is unsurprising as ITO is known to form a Schottky contact with p-type GaAs.[57] While these measurements do show current passing through the interface, an Ohmic contact is necessary for a device.

5.3.4 Effect of Surface Energy and Growth on Metallic Films

Metallic polycrystalline films (Pt and Ti) that would form an Ohmic contact with GaAs were explored. **Figure 7** shows top down SEM images of nanowires grown on Pt. **Figure 5.7a** is a plan-view SEM image of nanowires grown under identical conditions as those in **Fig. 5.1**. While there is a small number of tapered nanowires of varying sizes, the majority of the substrate is covered by a rough contiguous film, likely the result of planar polycrystalline GaAs growth similar to the continuous film observed in **Fig. 5.1c.** The difference in the morphology between the two substrates is likely related to changes in the relative surface energies of the catalyst, conductive films, and GaAs. Nanowire formation via the VLS growth mode requires that the catalyst forms isolated droplets on the surface. At growth temperatures of 400°C, the deposited Au film is a solid, but because it forms a eutectic alloy, it melts upon the introduction of Ga.[58] ITO has a lower surface energy (0.02-0.03J/m^2)[59,60] compared to Au-Ga (1.15 J/m^2),[61] resulting in dewetting of the catalyst which promote droplet isolation. Pt, on the other hand, has a much higher surface energy (2.3-2.8 J/m^2),[62,63] and thus exhibits a decreased tendency for droplet formation. The catalyst may be comprised of more complex alloys, namely $Au_xPt_yGa_z$ or $Au_xIn_yGa_z$, that could also impact the relative surface energy.

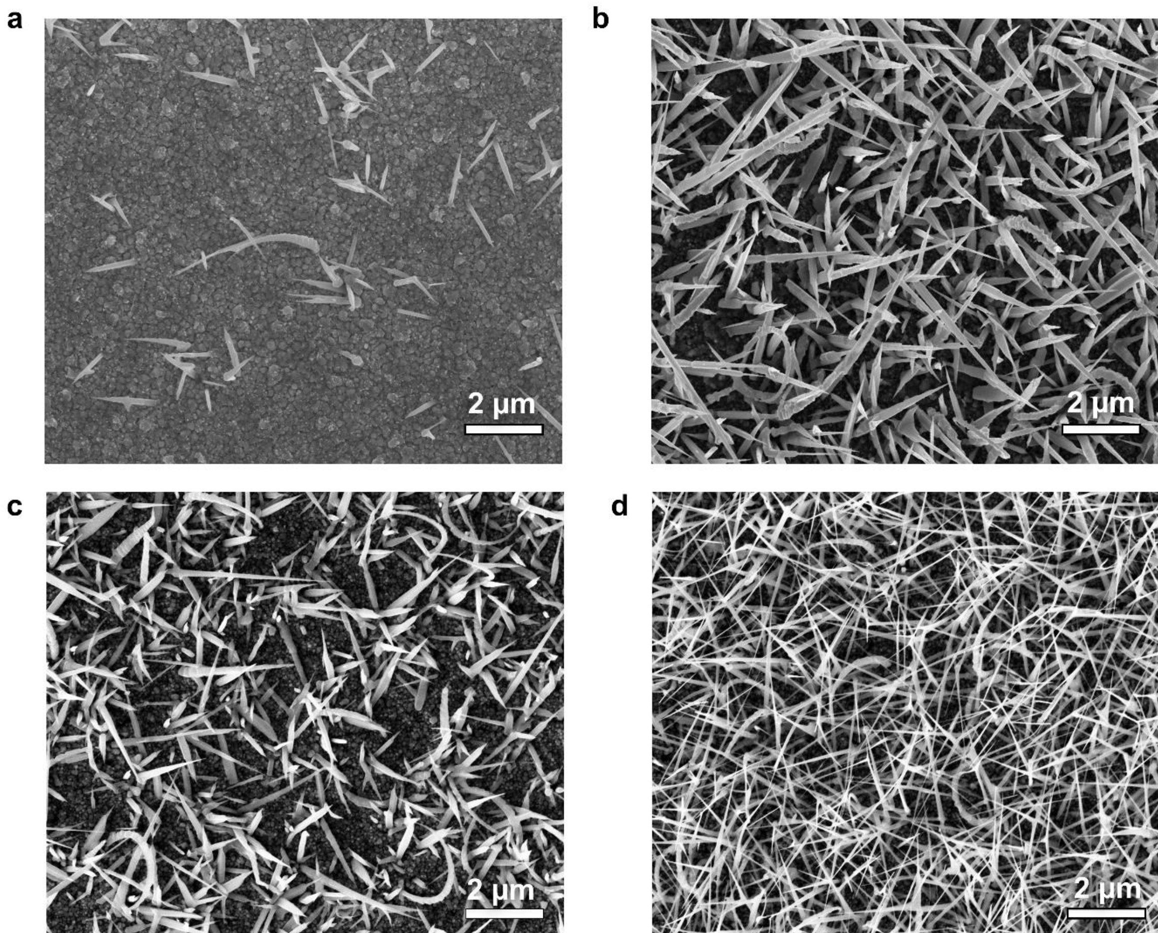

Figure 5.7: Plan-view SEM images of GaAs nanowires grown on Pt films at a) low Ga fluxes ($6x10^{-7}$ Torr) and b) high Ga fluxes ($9x10^{-7}$ Torr) along with the addition of c) Si and d) Be dopants at the higher deposition rate.

A higher Ga deposition rate is found to overcome this limitation and allow for nanowire formation. **Figure 7b** is a plan-view SEM image of nanowires on Pt grown at a higher Ga deposition rate (1.3 ML/s). In contrast to the sample grown at the lower Ga deposition rate (0.8 ML/s) seen in **Fig. 5.7a**, the highly tapered and randomly oriented nanowires in **Fig. 5.7b** completely cover the substrate surface. We propose that the faster deposition rate promotes random perturbations in the thickness of the catalyst layer, also called a Mullins-Sekerka instability,[64] that can lead to the formation of distinct droplets

that in turn catalyze nanowire growth. The effect of dopants on the nanowire shape is similar for these samples as for those grown on ITO. **Figure 5.7c** is a plan-view SEM image of GaAs nanowires doped with Si deposited at a high rate on Pt. Here, the nanowire density is somewhat lower than for the undoped samples, suggesting that the addition of Si inhibits nanowire growth. The addition of Be results in very thin, randomly oriented, and dense nanowires (**Fig. 5.7d**). Occasional curved nanowires are observed in all of the samples grown on Pt. Overall, the dopants effect on growth is very similar in metallic and oxide films.

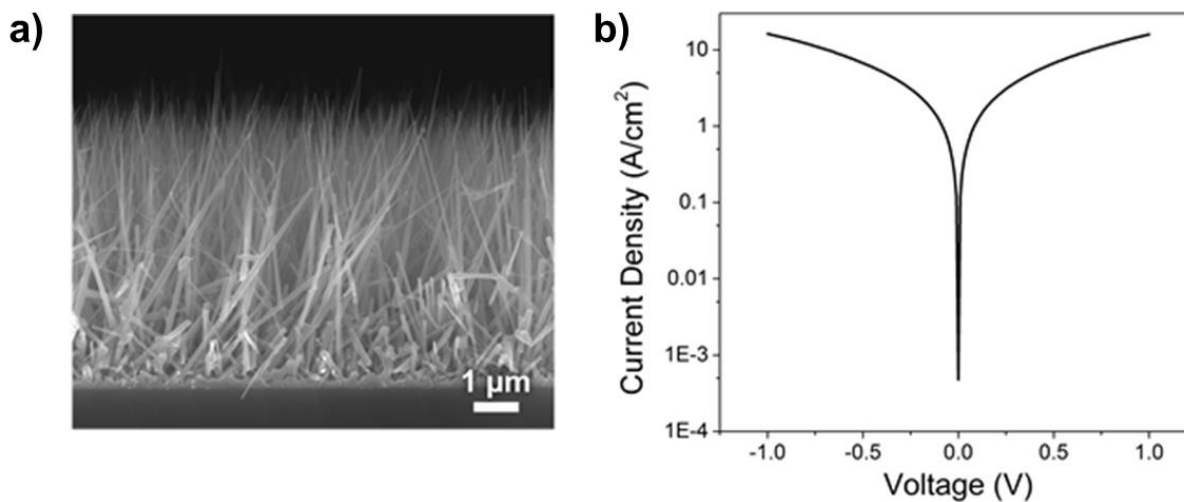

Figure 5.8: a) Cross-sectional SEM images of Be-doped GaAs nanowires grown for 30 minutes on a Ti film. b) I-V characteristics of Be-doped nanowires on Ti

Nanowire growth was explored on Ti, another metallic film, due to its widespread use in current semiconductor processing. Nanowire growth on Ti behaved similarly to Pt, as evident from the cross-sectional SEM image (**Fig 5.8a**). **Figure 5.8b** depicts the current density characteristics of Be-nanowires on Ti films. The samples were prepared for IV measurements using a parylene backfill in an identical manner to the samples with

ITO films. The IV curve for the nanowires grown on Ti is symmetric for negative and positive voltages meaning the Be-GaAs nanowires form an Ohmic connection with the Ti film. This is promising for the development of nanowire based optoelectronic devices on polycrystalline substrates because it shows that current can pass unimpeded between the nanowires and film.

5.3.5 Temperature Dependent Photoluminescence

Figure 5.9 shows the temperature dependent photoluminescence study of Be doped nanowires on Ti. Primary peaks at 1.50 (labeled as peak 1 in Fig. 7c) and 1.57 eV (peak 2) at 10K shift to 1.41 and 1.50 eV at room temperature. The intensity decreases and the peaks become less defined with increasing temperature. The 1.50 and 1.40 peak at 10K and room temperature respectively correspond to the p-type GaAs.[52] Similar to **Fig. 5.6c**, it is believed that the higher energy peak is the result of either a Burstein-Moss effect or quantum confinement. In the case of nanowires grown on Ti, this higher energy peak is significantly more pronounced. The position of this peak at room temperature is identical to that of another study of GaAs nanowires in which the optical emission of single nanowires are measured for quantum confinement.[53] The fact that there is a strong optical response at room temperature suggests that these nanowires are of sufficient quality to be used in optoelectronic devices.

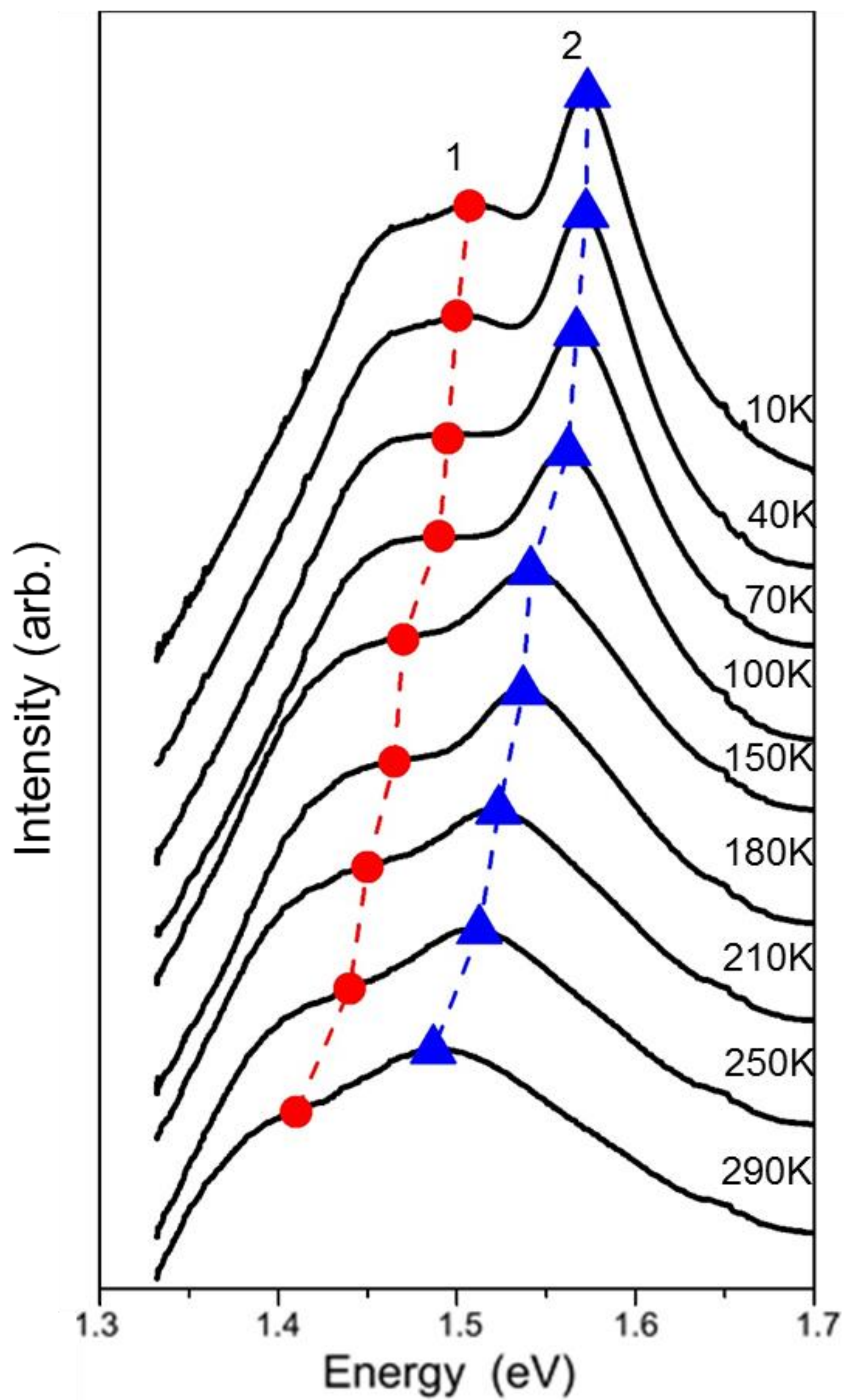

Figure 5.9: Temperature dependent photoluminescence of Be nanowires on Ti.

Figure 5.10 shows the temperature dependence of the emission energy of peaks 1 and 2. The trendlines were calculated using the Varshni equation, for bulk GaAs, but modified with different energies at T=0K (E_{G0}).[65] The energy positions of the both peaks decrease with increasing temperature and closely follow the calculated trendline. This close correlation suggests the nanowire features represented by peaks 1 and 2 have a similar temperature dependence to bulk GaAs. This is expected and provides evidence for similarities between the nanowires and single-crystalline bulk GaAs.

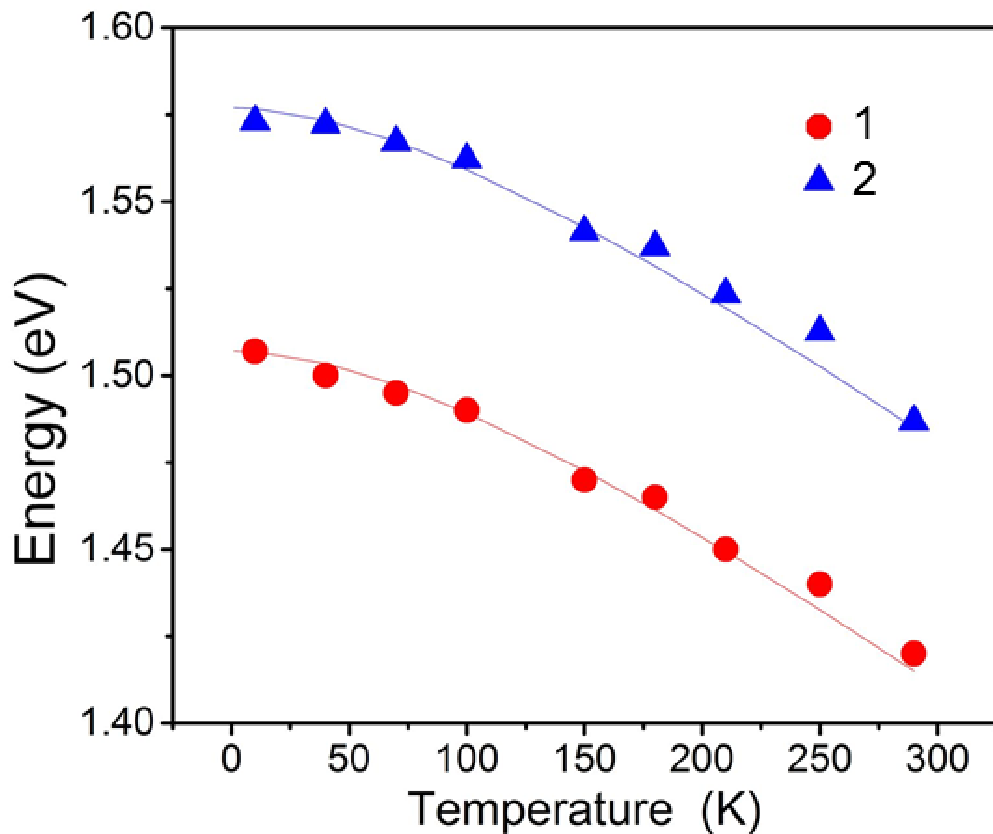

Figure 5.10: The photoluminescence peak energy positions vs temperature of Be doped nanowires on Ti

Figure 5.11 shows the plot of $I_0/I - 1$ vs 1/T, where I_0 is the integrated photoluminescence intensity extrapolated at T=0K and I is the integrated

photoluminescence intensity at temperature T, in order to determine the thermal activation energy for exciton formation (E_A). At temperatures above 50K we see quenching of the intensity, corresponding to an E_A of approximately 14meV. For comparison, nanowires grown near 600°C on GaAs and Si crystalline substrates have been reported with high temperature activation energies E_A of 17meV and 77meV respectively.[66,67] This suggests that the Be doped nanowires presented in this study are of fairly high quality and comparable to those grown at high temperatures on crystalline substrates.

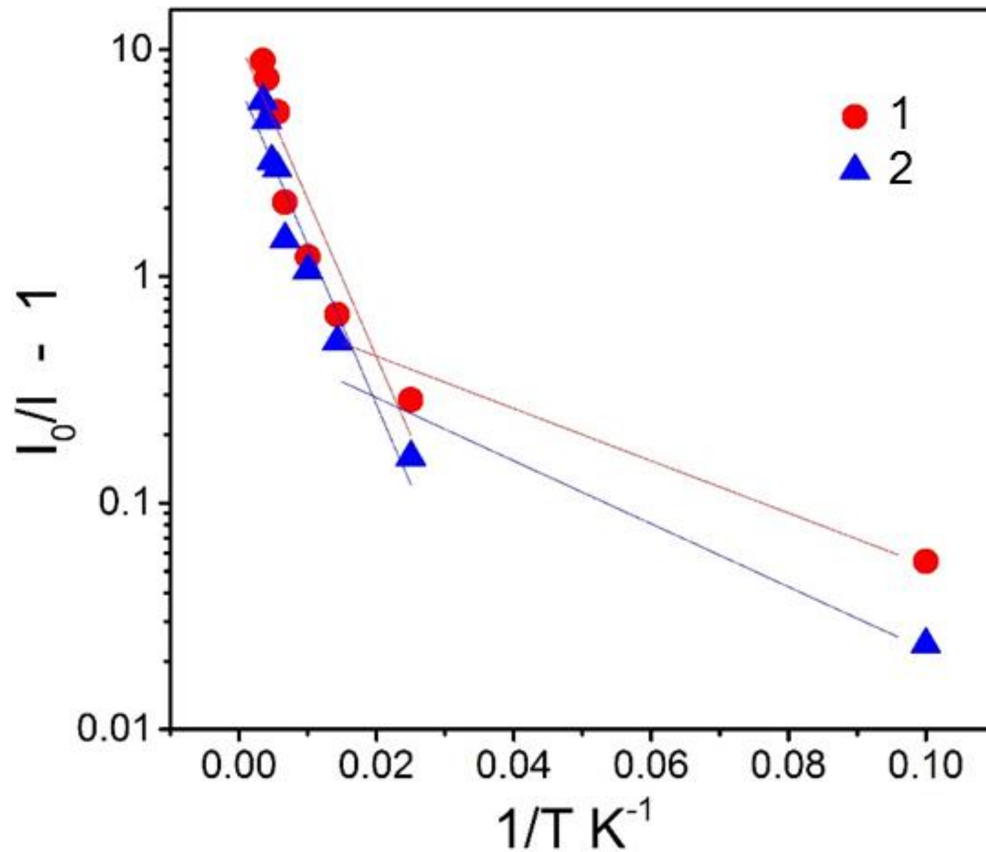

Figure 5.11: The integrated photoluminescence peak intensity vs inverse temperature of Be doped GaAs nanowires on Ti

5.3.6 Core-Shell Nanowires

For GaAs nanowire device fabrication, it is necessary to create a PN junction within the structure. One common method of doing this is the core-shell method. Initially a nanowire is grown using a single dopant type. Afterwards, the next part of the device, such as an intrinsic layer or a layer with the opposite dopant, is grown. However, the growth is controlled so that this next layer, and any subsequent layers are grown around the nanowire perimeter and do not substantially increase the height of the nanowire. The new layer acts as a “shell” around the original nanowire “core.” Any further layers are deposited and the device structure is created in the radial direction. This device layout is especially useful for photovoltaics as it increases the junction surface area improving minority carrier capture and passivates the sidewalls of the core region preventing loss.

For creating a PN junction using the nanowires in this study, we first started with the p-type Be-doped nanowire as the core. The superior morphology, uniformity in nanowire structure and lack of tapering from **Fig. 5.4** would create the foundation of a high density PN nanowire forest. Next, we introduced Si-doped GaAs to create an n-type layer. As observed in **Fig. 5.4** Si-doping increased sidewall growth and resulted in heavily tapered nanowire structures. As such, we expected the Si-doped GaAs to preferably adhere to the sidewalls as opposed to interact with the catalyst and this is more or less what we observed during growths.

Figure 5.12 shows high magnification SEM images of GaAs core-shell nanowires grown on ITO (**Fig. 5.12a-b**) and Ti (**Fig. 5.12c-d**) substrates. The output power of the doping eurotherms is the same as those used in **Fig. 5.4.** For the nanowires grown on ITO, the Be doped nanowire was grown at a Ga deposition rate (r_{Ga}) of 0.8 ML/s for t=15

minutes with an V/III As/Ga flux ratio of 10. After 15 minutes the growth was interrupted and the Ga deposition rate was reduced (r_{Ga}=0.4 ML/s) before depositing Si doped GaAs for t=8minutes (**Fig. 5.12a**) or t=15minutes (**Fig. 5.12b**). The V/III flux ratio was also increased to 26. The nanowires are not tapered and mostly uniform in height. The nanowire forests (not shown) are approximately 1.7 ± 0.2μm (**Fig. 5.12a**) and 1.8 ± 0.2μm (**Fig. 5.12b**) tall. In both samples the gold catalyst can still be seen on the apex of the nanowires.

From the images in **Fig. 5.12a** and **Fig. 5.12b** the core-shell regions are immediately obvious. In both samples, the nanowires have regions with two different diameters. The bulk of the nanowire is consistent in size until it nears the apex, at which it very sharply decreases in width. In **Fig. 5.12a** the bulk of the nanowire is approximately 50 ± 3nm wide and the region near the nanowire apex is approximately 27 ± 5nm wide. In **Fig. 5.12b** the bulk of the nanowire is approximately 77 ± 5nm wide and the region near the nanowire apex is approximately 25 ± 5nm wide. As a result of longer Si-doped GaAs deposition times (t=8 minutes in **Fig. 5.12a** to t=15 minutes in **Fig. 5.12b**), the bulk region of the nanowire increases approximately 50% in width. Furthermore, the nanowire forest height remains the same within error. This suggests Si-doped GaAs is mostly adhering to the sidewalls of the nanowire, creating a shell-like structure. This is consistent with our hypothesis and observations in **Fig. 5.4**. Comparatively, the thinner region near the apex remains the same diameter within error. This region is likely characteristic of the original Be-doped nanowire. However, without precise characterization, it is difficult to say whether we expect this region to be Be-doped or Si-doped. It is possible the Si-doped GaAs does not interact with the nanowire near the catalyst and only grows along the

sidewalls, leaving a portion of the Be-doped core exposed. Alternatively, it is possible the Si-doped GaAs does interact with the catalyst region, but at a significantly reduced rate than the sidewall region. As such there may be some vertical nanowire growth as a result of the Si-doping step, but it is so small the increase in height is indistinguishable.

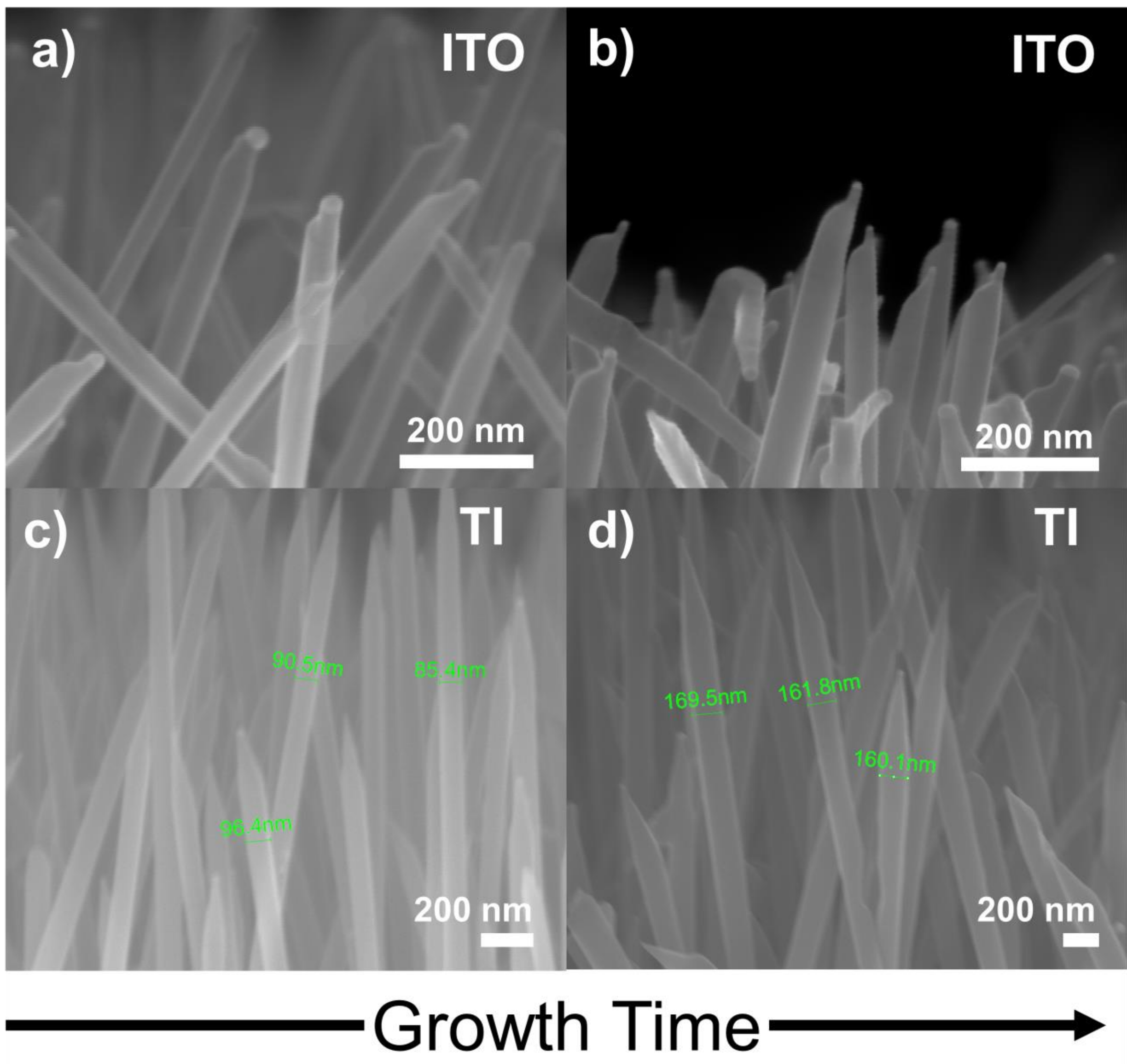

Figure 5.12: GaAs core-shell nanowires grown on a-b) ITO and c-d) Ti substrates with varied shell deposition steps.

Similar studies were performed on Ti substrates (**Fig. 5.12c-d**). For these nanowires, the Be doped nanowire was grown at a Ga deposition rate (r_{Ga}) of 1.3 ML/s for t=20 minutes with a V/III As/Ga flux ratio of 10. After 20 minutes the growth was interrupted and the Ga deposition rate was reduced (r_{Ga}=0.8 ML/s for **Fig. 5.12c** and r_{Ga}=0.4 ML/s for **Fig.5.12d**) before depositing Si doped GaAs for t=15 minutes (**Fig. 5.12c**) or t=60minutes (**Fig. 5.12d**). The V/III flux ratio was also increased to 26 in **Fig. 5.12c** and 40 in **Fig. 5.12d**. The nanowires grown on Ti are not tapered except for the region near the apex, where it sharply tapers of into a point. The nanowires and mostly uniform in height and the forests (not shown) are approximately 5.8 ± 0.3μm (**Fig. 5.12c**) and 6.4 ± 0.3μm (**Fig. 5.12d**) tall. In both samples the gold catalyst can still be seen on the apex of the nanowires.

In both **Fig. 5.12c** and **Fig. 5.12d** the bulk of the nanowires are consistent in size until it nears the apex, at which gradually decreases in width forming a tapered tip. In **Fig. 5.12c** the bulk of the nanowire is approximately 90 ± 5nm wide and the region directly under the catalyst at the nanowire apex is approximately 23 ± 5nm wide. In **Fig. 5.12d** the bulk of the nanowire is approximately 165 ± 8nm wide and region directly under the catalyst at the nanowire apex is approximately 27 ± 7nm wide. Similar to the ITO nanowires, we observe an increase in nanowire width with more Si-GaAs deposition. Based on the r_{Ga} and Si-GaAs deposition times, approximately 100% more Si-GaAs was deposited in **Fig. 5.12d** compared to **Fig. 5.12c**. This in close agreement with the approximately 80% increase in nanowire width measured between **Fig. 5.12c** and **Fig. 5.12d**. Furthermore, the shorter width of the nanowire near the apex is within error to the ITO sample, suggesting this resembles the width of the original Be-doped nanowires. This

is an agreement with the hypothesis that the majority of Si-doped GaAs adheres to the nanowire sidewalls.

However, unlike the nanowires grown on ITO, the core-shell structure is not as immediately obvious. This is because there is not a sharp change in nanowire width near the apex. Rather there is a steady decrease approximately 190 ± 30nm (**Fig. 5.12c**) and 400 ± 50nm (**Fig. 5.12d**) below the catalyst. This tapered structure vs sharp width change in the Ti vs. ITO samples may be due to a difference in catalyst - nanowire contact angle. It has previously been demonstrated that the nanowire-catalyst contact angle can be heavily influential in the nanowire growth.[42,58] Based on the surface energy differences between metals and oxides, we expect increased wetting on the metal resulting in a smaller catalyst-substrate contact angle on Ti compared to ITO. It is possible that this discrepancy impacts the behavior of GaAs sidewall growth in the regions near the catalyst.

The impact of excessive doping was also measured on the core-shell nanowire growth structures. **Figure 5.13** shows core-shell nanowires grown on ITO with low and high Be/Si doping. In **Fig. 5.13a-b** The output power of the Be and Si eurotherms were 10.0 and 7.0 respectively. For **Fig. 5.13c-d** the output power of the Be and Si eurotherms were 11.5 and 9.5 respectively. For comparison the output power of the Be and Si eurotherms in **Fig. 5.4** was 10.0 and 9.0 respectively. Unfortunately doping calibrations of planar GaAs growth using the same eurotherm output power values in **Fig. 5.13** is not available. The growth time of both the Be and Si step was 7.5 min (15 min total growth time) in **Fig. 5.13a** and **Fig. 5.13c** and 15min (30 min total growth time) in **Fig. 5.13b** and **Fig. 5.13d**. In these samples the r_{Ga}= 0.8 ML/s and the V/II As/Ga flux ratio was at 10.

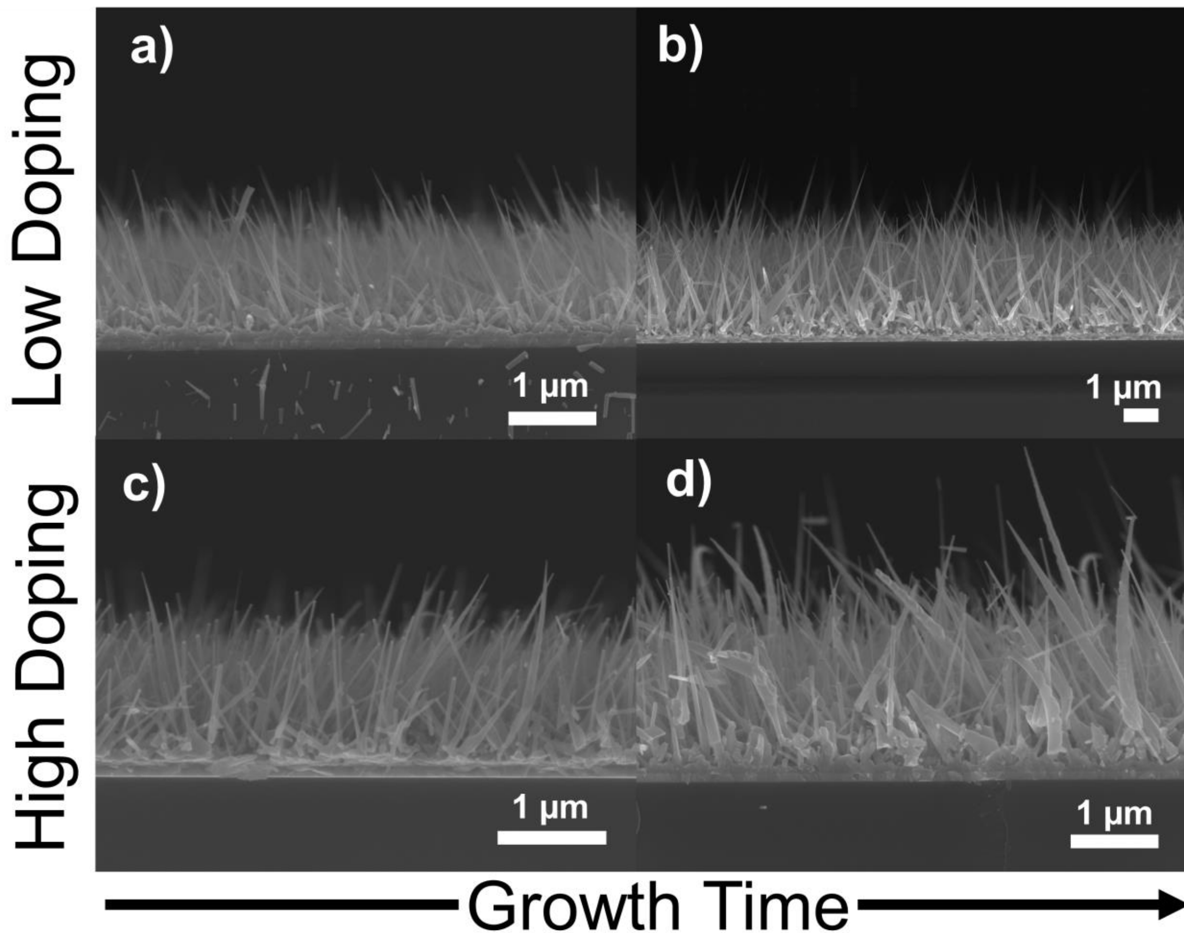

Figure 5.13: GaAs nanowires grown on ITO with a-b) low and c) high Be and Si doping levels. Each doping step was either a,c) 7.5 min or b,d) 15 min long.

In the samples with low doping, the nanowire forest height increased from 1.8 ± 0.1μm in **Fig. 5.13a** to 3.3 ± 0.2 μm in **Fig. 5.13b.** The width of the nanowires increased from 50 ± 6nm in **Fig. 5.13a** to 85 ± 7nm in **Fig. 5.13b.** These measurements are consistent with what we would expect from **Fig. 5.12**. Specifically, the deposition time of the Si doping step increased by 100% and we observe an approximately 70% increase in nanowire width. This observation is in close agreement with the 80% change in nanowire width observed in **Fig 5.12**.The deposition time of Be doping step also increases

by 100% and the nanowire forest height increases by approximately 80%. These two observations suggest that the Be doping step controls the final nanowire forest height, whereas Si-doping step controls the final nanowire width. The SEM images also show that nanowires are slightly tapered but mostly uniform in height. There is little change in nanowire morphology between **Fig. 5.13a** and **Fig. 5.13b**.

In the samples with high doping, the nanowire forest height increased from 1.3 ± 0.1μm in **Fig. 5.13c** to 2.2 ± 0.4 μm in **Fig. 5.13d**. The width of the nanowires increased from 46 ± 10nm in **Fig. 5.13c** to 100 ± 30nm in **Fig. 5.13d**. In these samples we observe a similar 70% and increase in height between the two samples consistent with **Fig. 5.13a-d**. However, there is an approximately 100% increase in width which is 20-30% larger than that observed in **Fig. 5 .13a-d** and **Fig. 5.12d.** Additionally, the variance of the width is much wider in **Fig. 5.13c** and **Fig. 5.13d** than in the previous core-shell growths. This discrepancy can be observed in the nanowire morphology as well. For example, in **Fig. 5.13c** the majority of the nanowires are not tapered and the nanowire catalyst is visible at the apex (under high magnification). However, there is a small percentage of nanowires (5%) that are tapered and have noticeably rougher sidewalls. In **Fig. 5.13d** rough sidewalls become much more prominent (50-60%) and some of the nanowires show curvature and resemble those in **Fig. 5.4b.** The nanowire height is much less uniform, with the outliers being the nanowires that exhibit a high degree of tapering and rough sidewalls. This is in stark contrast to the nanowires with low doping in **Fig. 5.13b**. From **Fig. 5.13** it is clear that increasing the Si doping beyond a certain level causes the morphology of the nanowire shell to exhibit properties similar to those that are solely Si-doped. This morphology is undesirable for device fabrication purposes due to the non-

uniform height distribution. This morphology is also undesirable because of its reduced optical and structure characteristics (**Fig. 5.5** and **Fig. 5.6**). It is suggested for device quality nanowires that the Si eurootherm output power remains low enough to prevent this type of nanowire morphology.

5.4 Conclusions

In summary, we have been able to demonstrate that Be doping can enable the growth of high quality GaAs nanowire growth at low temperatures on polycrystalline films. Among other applications, this will allow for direct integration of nanowire-based optoelectronic devices with conventional CMOS technology. We demonstrate that nanowires can be grown on polycrystalline ITO, Pt and Ti films, but believe the process can be applied to other oxide and metallic surfaces. Growth on polycrystalline substrates will cause nanowires to have random orientations, which can result in termination events, reducing nanowire density. We show that by growing with Be, these termination events can be reduced, and the nanowire quality can be improved. The nanowires have a thermal activation energy of 14meV which is comparable to GaAs nanowires grown on crystalline substrates and at higher temperatures. A greater understanding of the dopant interactions and development of a p-n junction is necessary and the direction of future work.

5.5 References

1. Gubbi, J., Buyya, R., Marusic, S., & Palaniswami, M. (2013). Internet of Things (IoT): A vision, architectural elements, and future directions. *Future Generation Computer Systems*, *29*(7), 1645-1660.
2. Lee, I., Kim, Y., Bang, S., Kim, G., Ha, H., Chen, Y. P., ... & Foo, Z. (2014, September). Circuit techniques for miniaturized biomedical sensors. In *CICC* (pp. 1-7).
3. Akyildiz, I. F., Su, W., Sankarasubramaniam, Y., & Cayirci, E. (2002). Wireless Sensor Networks: A Survey. Comput-er Networks, 38, 393-422.
4. Domingo, M. C. (2012). An overview of the Internet of Things for people with disabilities. *Journal of Network and Computer Applications*, *35*(2), 584-596.
5. Jung, W., Oh, S., Bang, S., Lee, Y., Foo, Z., Kim, G., ... & Blaauw, D. (2014). An ultra-low power fully integrated energy harvester based on self-oscillating switched-capacitor voltage doubler. *IEEE Journal of Solid-State Circuits*, *49*(12), 2800-2811.
6. Lee, Y., Bang, S., Lee, I., Kim, Y., Kim, G., Ghaed, M. H., ... & Blaauw, D. (2013). A Modular 1 mm Die-Stacked Sensing Platform With Low Power I C Inter-Die Communication and Multi-Modal Energy Harvesting. *IEEE Journal of Solid-State Circuits*, *48*(1), 229-243.
7. Fojtik, M., Kim, D., Chen, G., Lin, Y. S., Fick, D., Park, J., ... & Sylvester, D. (2013). A millimeter-scale energy-autonomous sensor system with stacked battery and solar cells. *IEEE Journal of Solid-State Circuits*, *48*(3), 801-813.

8. Teran, A. S., Wong, J., Lim, W., Kim, G., Lee, Y., Blaauw, D., & Phillips, J. D. (2015). AlGaAs photovoltaics for indoor energy harvesting in mm-scale wireless sensor nodes. *IEEE Transactions on Electron Devices*, *62*(7), 2170-2175.
9. Warneke, B. A., Scott, M. D., Leibowitz, B. S., Zhou, L., Bellew, C. L., Chediak, J. A., ... & Pister, K. S. (2002). An autonomous 16 mm 3 solar-powered node for distributed wireless sensor networks. In *Sensors, 2002. Proceedings of IEEE* (Vol. 2, pp. 1510-1515). IEEE.
10. Tsai, H. L., & Lee, J. W. (1987). Defect structures at the GaAs/Si interface after annealing. *Applied physics letters*, *51*(2), 130-132.
11. Lee, J. W., Shichijo, H., Tsai, H. L., & Matyi, R. J. (1987). Defect reduction by thermal annealing of GaAs layers grown by molecular beam epitaxy on Si substrates. *Applied Physics Letters*, *50*(1), 31-33.
12. Dohrman, C. L., Chilukuri, K., Isaacson, D. M., Lee, M. L., & Fitzgerald, E. A. (2006). Fabrication of silicon on lattice-engineered substrate (SOLES) as a platform for monolithic integration of CMOS and optoelectronic devices. *Materials Science and Engineering: B*, *135*(3), 235-237.
13. Goossen, K. W., Walker, J. A., D'asaro, L. A., Hui, S. P., Tseng, B., Leibenguth, R., ... & Lentine, A. L. (1995). GaAs MQW modulators integrated with silicon CMOS. *IEEE Photonics Technology Letters*, *7*(4), 360-362.
14. Yeh, H. J., & Smith, J. S. (1994). Fluidic self-assembly for the integration of GaAs light-emitting diodes on Si substrates. *IEEE Photonics Technology Letters*, *6*(6), 706-708.

15. Tomioka, K., Motohisa, J., Hara, S., Hiruma, K., & Fukui, T. (2010). GaAs/AlGaAs core multishell nanowire-based light-emitting diodes on Si. *Nano letters*, *10*(5), 1639-1644.

16. Hersee, S. D., Fairchild, M., Rishinaramangalam, A. K., Ferdous, M. S., Zhang, L., Varangis, P. M., ... & Talin, A. A. (2009). GaN nanowire light emitting diodes based on templated and scalable nanowire growth. *Electronics Letters*, *45*(1), 75-76.

17. Sadaf, S. M., Ra, Y. H., Szkopek, T., & Mi, Z. (2016). Monolithically Integrated Metal/Semiconductor Tunnel Junction Nanowire Light-Emitting Diodes. *Nano letters*, *16*(2), 1076-1080.

18. Qian, F., Gradecak, S., Li, Y., Wen, C. Y., & Lieber, C. M. (2005). Core/multishell nanowire heterostructures as multicolor, high-efficiency light-emitting diodes. *Nano letters*, *5*(11), 2287-2291.

19. Bao, J., Zimmler, M. A., Capasso, F., Wang, X., & Ren, Z. F. (2006). Broadband ZnO single-nanowire light-emitting diode. *Nano letters*, *6*(8), 1719-1722.

20. Garnett, E. C., Brongersma, M. L., Cui, Y., & McGehee, M. D. (2011). Nanowire solar cells. *Annual Review of Materials Research*, *41*, 269-295.

21. Nakai, E., Yoshimura, M., Tomioka, K., & Fukui, T. (2013). GaAs/InGaP Core–Multishell Nanowire-Array-Based Solar Cells. *Japanese Journal of Applied Physics*, *52*(5R), 055002.

22. Mariani, G., Scofield, A. C., Hung, C. H., & Huffaker, D. L. (2013). GaAs nanopillar-array solar cells employing in situ surface passivation. *Nature communications*, *4*, 1497.

23. Yao, M., Huang, N., Cong, S., Chi, C. Y., Seyedi, M. A., Lin, Y. T., ... & Zhou, C. (2014). GaAs nanowire array solar cells with axial p–i–n junctions. *Nano letters*, *14*(6), 3293-3303.

24. Tsakalakos, L., Balch, J., Fronheiser, J., Korevaar, B. A., Sulima, O., & Rand, J. (2007). Silicon nanowire solar cells. *Applied Physics Letters*, *91*(23), 233117.

25. Takeuchi, H., Wung, A., Sun, X., Howe, R. T., & King, T. J. (2005). Thermal budget limits of quarter-micrometer foundry CMOS for post-processing MEMS devices. *IEEE transactions on Electron Devices*, *52*(9), 2081-2086.

26. Calabrese, G., Corfdir, P., Gao, G., Pfüller, C., Trampert, A., Brandt, O., ... & Fernández-Garrido, S. (2016). Molecular beam epitaxy of single crystalline GaN nanowires on a flexible Ti foil. *Applied Physics Letters*, *108*(20), 202101.

27. Sarwar, A. T. M., Carnevale, S. D., Yang, F., Kent, T. F., Jamison, J. J., McComb, D. W., & Myers, R. C. (2015). Semiconductor Nanowire Light-Emitting Diodes Grown on Metal: A Direction Toward Large-Scale Fabrication of Nanowire Devices. *Small*, *11*(40), 5402-5408.

28. Statkute, G. (2008). Growth of GaAs nanowires on Au, Au/Pd, Ag, Ni, Ga, Cu, Al, Ti metal films. *arXiv preprint arXiv:0811.4248*.

29. Dhaka, V., Haggren, T., Jussila, H., Jiang, H., Kauppinen, E., Huhtio, T., ... & Lipsanen, H. (2012). High quality GaAs nanowires grown on glass substrates. *Nano letters*, *12*(4), 1912-1918.

30. Wu, D., Tang, X., Wang, K., Olivier, A., & Li, X. (2016). Parameters study on the growth of GaAs nanowires on indium tin oxide by metal-organic chemical vapor deposition. *Journal of Applied Physics*, *119*(9), 094305.

31. Ikejiri, K., Ishizaka, F., Tomioka, K., & Fukui, T. (2013). GaAs nanowire growth on polycrystalline silicon thin films using selective-area MOVPE. *Nanotechnology*, *24*(11), 115304.

32. Wagner, R. S., & Ellis, W. C. (1964). Vapor-liquid-solid mechanism of single crystal growth. *Applied Physics Letters*, *4*(5), 89-90.

33. Tchernycheva, M., Harmand, J. C., Patriarche, G., Travers, L., & Cirlin, G. E. (2006). Temperature conditions for GaAs nanowire formation by Au-assisted molecular beam epitaxy. *Nanotechnology*, *17*(16), 4025.

34. Harmand, J. C., Tchernycheva, M., Patriarche, G., Travers, L., Glas, F., & Cirlin, G. (2007). GaAs nanowires formed by Au-assisted molecular beam epitaxy: Effect of growth temperature. *Journal of Crystal Growth*, *301*, 853-856.

35. Kim, H., Gilmore, C. M., Pique, A., Horwitz, J. S., Mattoussi, H., Murata, H., ... & Chrisey, D. B. (1999). Electrical, optical, and structural properties of indium–tin–oxide thin films for organic light-emitting devices. *Journal of Applied Physics*, *86*(11), 6451-6461.

36. Nadaud, N., Lequeux, N., Nanot, M., Jove, J., & Roisnel, T. (1998). Structural studies of tin-doped indium oxide (ITO) and In 4 Sn 3 O 12. *Journal of Solid State Chemistry*, *135*(1), 140-148.

37. Hannon, J. B., Kodambaka, S., Ross, F. M., & Tromp, R. M. (2006). The influence of the surface migration of gold on the growth of silicon nanowires. *Nature*, *440*(7080), 69-71.

38. Kawashima, T., Mizutani, T., Nakagawa, T., Torii, H., Saitoh, T., Komori, K., & Fujii, M. (2008). Control of surface migration of gold particles on Si nanowires. *Nano letters*, *8*(1), 362-368.

39. Bar-Sadan, M., Barthel, J., Shtrikman, H., & Houben, L. (2012). Direct imaging of single Au atoms within GaAs nanowires. *Nano letters*, *12*(5), 2352-2356.

40. Allen, J. E., Hemesath, E. R., Perea, D. E., Lensch-Falk, J. L., Li, Z. Y., Yin, F., ... & Lauhon, L. J. (2008). High-resolution detection of Au catalyst atoms in Si nanowires. *Nature nanotechnology*, *3*(3), 168-173.

41. Zhou, H. L., Hoang, T. B., Dheeraj, D. L., Van Helvoort, A. T. J., Liu, L., Harmand, J. C., ... & Weman, H. (2009). Wurtzite GaAs/AlGaAs core–shell nanowires grown by molecular beam epitaxy. *Nanotechnology*, *20*(41), 415701.

42. Kodambaka, S., Tersoff, J., Reuter, M. C., & Ross, F. M. (2006). Diameter-independent kinetics in the vapor-liquid-solid growth of Si nanowires. *Physical review letters*, *96*(9), 096105.

43. Li, W. Q., Bhattacharya, P. K., Kwok, S. H., & Merlin, R. (1992). Molecular-beam epitaxial growth and characterization of silicon-doped AlGaAs and GaAs on (311) A GaAs substrates and their device applications. *Journal of applied physics*, *72*(7), 3129-3135.

44. Lee, J. L., Wei, L., Tanigawa, S., & Kawabe, M. (1991). Impurity effects on both the creation and the migration of Ga vacancies in GaAs. *Journal of applied physics*, *70*(2), 674-684.

45. Koren, E., Berkovitch, N., & Rosenwaks, Y. (2010). Measurement of active dopant distribution and diffusion in individual silicon nanowires. *Nano letters*, *10*(4), 1163-1167.

46. Yang, Z. X., Han, N., Fang, M., Lin, H., Cheung, H. Y., Yip, S., ... & Ho, J. C. (2014). Surfactant-assisted chemical vapour deposition of high-performance small-diameter GaSb nanowires. *Nature communications*, *5*.

47. Tchernycheva, M., Harmand, J. C., Patriarche, G., Travers, L., & Cirlin, G. E. (2006). Temperature conditions for GaAs nanowire formation by Au-assisted molecular beam epitaxy. *Nanotechnology*, *17*(16), 4025.

48. Plante, M. C., & LaPierre, R. R. (2008). Au-assisted growth of GaAs nanowires by gas source molecular beam epitaxy: Tapering, sidewall faceting and crystal structure. *Journal of Crystal Growth*, *310*(2), 356-363.

49. Dick, K. A., Deppert, K., Mårtensson, T., Mandl, B., Samuelson, L., & Seifert, W. (2005). Failure of the vapor-liquid-solid mechanism in Au-assisted MOVPE growth of InAs nanowires. *Nano letters*, *5*(4), 761-764.

50. Heiss, M., Conesa-Boj, S., Ren, J., Tseng, H. H., Gali, A., Rudolph, A., ... & Reiger, E. (2011). Direct correlation of crystal structure and optical properties in wurtzite/zinc-blende GaAs nanowire heterostructures. *Physical Review B*, *83*(4), 045303.

51. Vainorius, N., Jacobsson, D., Lehmann, S., Gustafsson, A., Dick, K. A., Samuelson, L., & Pistol, M. E. (2014). Observation of type-II recombination in single wurtzite/zinc-blende GaAs heterojunction nanowires. *Physical Review B*, *89*(16), 165423.

52. Scott, G. B., Duggan, G., Dawson, P., & Weimann, G. (1981). A photoluminescence study of beryllium-doped GaAs grown by molecular beam epitaxy. *Journal of Applied Physics*, *52*(11), 6888-6894.

53. Duan, X., Wang, J., & Lieber, C. M. (2000). Synthesis and optical properties of gallium arsenide nanowires. *Applied Physics Letters*, *76*(9), 1116-1118.

54. Burstein, E. (1954). Anomalous optical absorption limit in InSb. *Physical Review*, *93*(3), 632.

55. Moss, T.S. (1954) The interpretation of the properties of indium antimonide. *Proceedings of the Physical Society. Section B*. (67) 775

56. Sarkar, A., Ghosh, S., Chaudhuri, S., & Pal, A. K. (1991). Studies on electron transport properties and the Burstein-Moss shift in indium-doped ZnO films. *Thin Solid Films*, *204*(2), 255-264.

57. Morgan, D. V., Aliyu, Y., & Bunce, R. W. (1992). The Thermal Stability of Indium-Tin-Oxide/n-GaAs Schottky Contacts. *physica status solidi (a)*, *133*(1), 77-93.

58. Harmand, J. C., Patriarche, G., Péré-Laperne, N., Merat-Combes, M. N., Travers, L., & Glas, F. (2005). Analysis of vapor-liquid-solid mechanism in Au-assisted GaAs nanowire growth. *Applied Physics Letters*, *87*(20), 203101.

59. Kim, J. S., Friend, R. H., & Cacialli, F. (1999). Surface energy and polarity of treated indium–tin–oxide anodes for polymer light-emitting diodes studied by contact-angle measurements. *Journal of Applied Physics*, *86*(5), 2774-2778.

60. Petrosino, M., Vacca, P., Licciardo, G. D., Rubino, A., & Bellone, S. (2007, December). The effect of ITO surface energy on OLED electrical properties. In

Physics of Semiconductor Devices, 2007. IWPSD 2007. International Workshop on (pp. 606-609). IEEE.

61. Sakong, S., Du, Y. A., & Kratzer, P. (2013). Atomistic modeling of the Au droplet–GaAs interface for size-selective nanowire growth. *Physical Review B*, *88*(15), 155309.
62. Vitos, L., Ruban, A. V., Skriver, H. L., & Kollar, J. (1998). The surface energy of metals. *Surface Science*, *411*(1), 186-202.
63. Singh-Miller, N. E., & Marzari, N. (2009). Surface energies, work functions, and surface relaxations of low-index metallic surfaces from first principles. *Physical Review B*, *80*(23), 235407.
64. Mullins, W. W., & Sekerka, R. F. (1964). Stability of a planar interface during solidification of a dilute binary alloy. *Journal of applied physics*, *35*(2), 444-451.
65. Kasap, S. O. (2006). *Principles of electronic materials and devices*. McGraw-Hill.
66. Titova, L. V., Hoang, T. B., Jackson, H. E., Smith, L. M., Yarrison-Rice, J. M., Kim, Y., ... & Jagadish, C. (2006). Temperature dependence of photoluminescence from single core-shell GaAs–AlGaAs nanowires.
67. Breuer, S., Pfüller, C., Flissikowski, T., Brandt, O., Grahn, H. T., Geelhaar, L., & Riechert, H. (2011). Suitability of Au-and self-assisted GaAs nanowires for optoelectronic applications. *Nano letters*, *11*(3), 1276-1279.

Chapter 6
Bismuth as a catalyst for GaAs nanowire growth

Vapor-liquid-solid growth (VLS) of GaAs using Bi droplets as the catalyst is presented. The growth is exceedingly difficult due to the high volatility of the Bi droplets requiring concurrent Bi deposition. The nanostructures that result from the VLS growth are short discs and in some cases the discs are overlapped by another disc or series of discs with increasingly larger sizes. This structure forms due to the Bi droplet increasing in size during growth. At some point during nanostructure formation, the Bi droplet becomes too large and destabilizes, whereupon it drops off the disc onto the substrate and begins the catalysis of a new disc with a larger radius. The observed contact angle at destabilization is found by measuring the size of adjacent discs and found to be too large for the Gibbs' criterion, suggesting failure is due to droplet-sidewall wetting.

6.1 Introduction

Semiconductor nanowires have shown to be very beneficial in the advancement of thermoelectrics,[1,2] photovoltaics,[3,4] biological sensing,[5] and even on-chip optoelectronic integration. For optoelectronic device, nanowires are typically grown epitaxially via the vapor-liquid-solid (VLS) mechanism in which a liquid metal is used as a catalyst to facilitate the growth of the nanowire at the catalyst/semiconductor interface.[6] Several models describing the VLS process emphasize the strong dependence of growth

chemistry and parameters on the interaction between the catalyst and underlying crystal.[6-10] These interactions have been shown to give rise to kinking, crawling, and structural phase transitions.[11-13] Being able to understand how these phenomena occur can grant insight on how to control all aspects of nanowire growth.

Au nanoparticles have proven to be a very reliable catalyst for Si and III-V nanowire formation. However, studies have shown that Au can incorporate during nanowire growth and introduce deep level defects which severely hamper device performance.[14,15] As a result, other metals such as Ga, Al and In have been investigated as potential alternatives, but many of these methods require an additional mask, such as a perforated oxide layer, in order to produce quality vertical nanowires.[16-21] Liquid Bi droplets has been largely unexplored as a catalyst for epitaxial growth of III-V compound semiconductors and may be a strong alternative. Solution-based catalysis of of SnS_2, GaAs, InP, GaP, and InAs nanowires has already been demonstrated using nanocrystalline Bi particles.[22,23] Additionally, liquid Bi droplets were used as a catalyst in the growth of CdTe/CdSe, PbTe, and Si nanowires on plastic and glass substrates using vapor deposition techniques.[24-26] Like Ga and In, Bi has a very low melting point and because it is a group V element, it will not introduce deep level defects.[27] It also has a low incorporation rate due its large atomic size, making ternary formation difficult.[27-29] Here we present on the dynamics of initial disc formation using Bi as a catalyst for VLS growth of epitaxial GaAs structures, and show how the resulting nanostructure may be affected by droplet destabilization.

6.2 Experimental Methods

GaAs nanostructures were grown using a molecular beam epitaxy chamber. All samples consisted of a n-type Si doped GaAs (100) substrate with a 500nm GaAs buffer layer grown at T_s=580°C at a Ga deposition rate of r_{Ga}=0.6 monolayers/second. The substrates were annealed for 10 minutes under As and then the temperature was reduced to either 320°C or 360°C as measured by a low temperature optical pyrometer. Once at growth temperature the As overpressure (5.6×10^{-7} Torr $\leq BEP_{As} \leq 6.1 \times 10^{-6}$ Torr) was modified to the desired growth conditions and Bi (5.4×10^{-8} Torr $\leq BEP_{As} \leq 1.4 \times 10^{-6}$ Torr) was deposited for 15s to create droplets. Immediately afterwards, a Ga flux (BEP_{Ga}=2×10^{-7} Torr) was introduced for 5 to 45 minutes, in addition to the As and Bi flux. The Ga, As and Bi beam equivalent pressure (BEP) were varied between each trial as detailed in Table I. After deposition all of the shutters were closed and the samples were quenched. Once removed from the chamber the samples were examined using secondary electrons in a scanning electron microscope. Cross sectional images were taken by cleaving the sample in air before mounting on a 90° SEM stage.

6.3 Data Analysis

6.3.1 Bismuth Catalyst Formation and Desorption

Nanowires are produced via the VLS mechanism only when the crystallization at the Bi_{ℓ}-$GaAs_{s}$ interface is faster than epitaxial growth in areas without a catalyst. At the growth temperatures used in this study, the vapor pressure of Bi is high enough to completely desorb within the 5-10 minute growth window. Comparatively, Au, Ag, Ga, and In have lower vapor pressures. As such, a constant flux of catalyst material is necessary to prevent complete evaporation. A delicate balance between Bi deposition and desorption is required to maintain a constant droplet size.

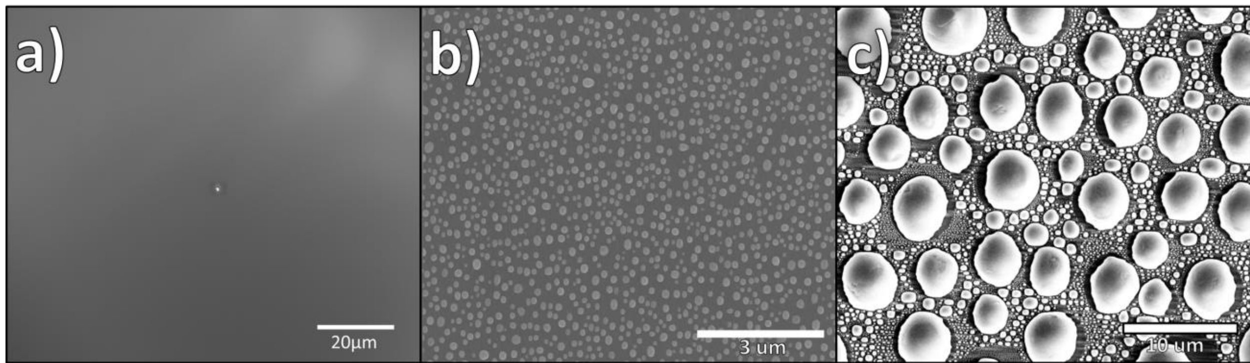

Figure 6.1: Planar SEM images of growths at T_s=320°C with increasing Bi fluxes and correspond to a) sample A b) sample B and c) sample C.

Figure 6.1 shows SEM images of the concurrent deposition of Ga, As, and Bi at T_S=320°C for 45 minutes as a function of increasing Bi flux. **Figure 1a** shows growth conditions in which If the Bi flux is significantly lower than the desorption rate (BEP_{Bi} = 5.4x10^{-8}). There is no Bi present on the surface and there is planar growth of GaAs. **Figure 1b** shows growth conditions with a slightly higher Bi flux (BEP_{Bi} = 1.1x10^{-7}). There is a uniform distribution of lens-shaped droplets caused by a balance between the the Bi

desorption rate and Bi arrival. The lens-shaped droplets are maintained on the surface for extended periods of time. **Figure 1c** shows growth if the Bi flux is very high (BEP_{Bi} = $1.4x10^{-6}$). In this case the surface is covered with a bimodal distribution of droplets. The Bi desorption rate is very sensitive to substrate temperature, and higher Bi flux is needed with increasing substrate temperature to maintain the same droplet size. Maintaining uniform droplets is highly dependent on precise equipment manipulation to reproduce identical Bi flux and substrate temperature relationships.

The size and density of Bi droplets are dictated by temperature, Bi flux, and deposition duration, while their shape is dictated by capillary forces. The liquid droplets are lens-shaped with a wetting angle θ_w dependent on the interfacial energies. Since the densities of liquid and solid Bi differ by only 3%,[27] the liquid Bi contact angle can be approximated from the cross-sections of solid droplets. **Figure 6.2** shows a cross-sectional SEM image of solid Bi droplets and the contact angle between solid Bi and GaAs can be measured. Using approximately 15 measurements over two samples, the equilibrium wetting angle θ_w for liquid Bi is found to be 78 ± 2°. Cross-sectional SEM also shows that the Bi droplets exhibit almost no etching of the GaAs substrate at temperatures of T_s=360°C, suggesting that there is very low solubility of GaAs in liquid Bi (**Fig. 6.2**). In comparision, liquid Ga droplets have shown to etch GaAs substrates at elevated temperatures.[30,31] This suggests that Ga and As vapor dissolution is also low, which would mean a low crystallization flux at the Bi_ℓ-$GaAs_s$ interface corresponding to a slow nanowire growth rate.

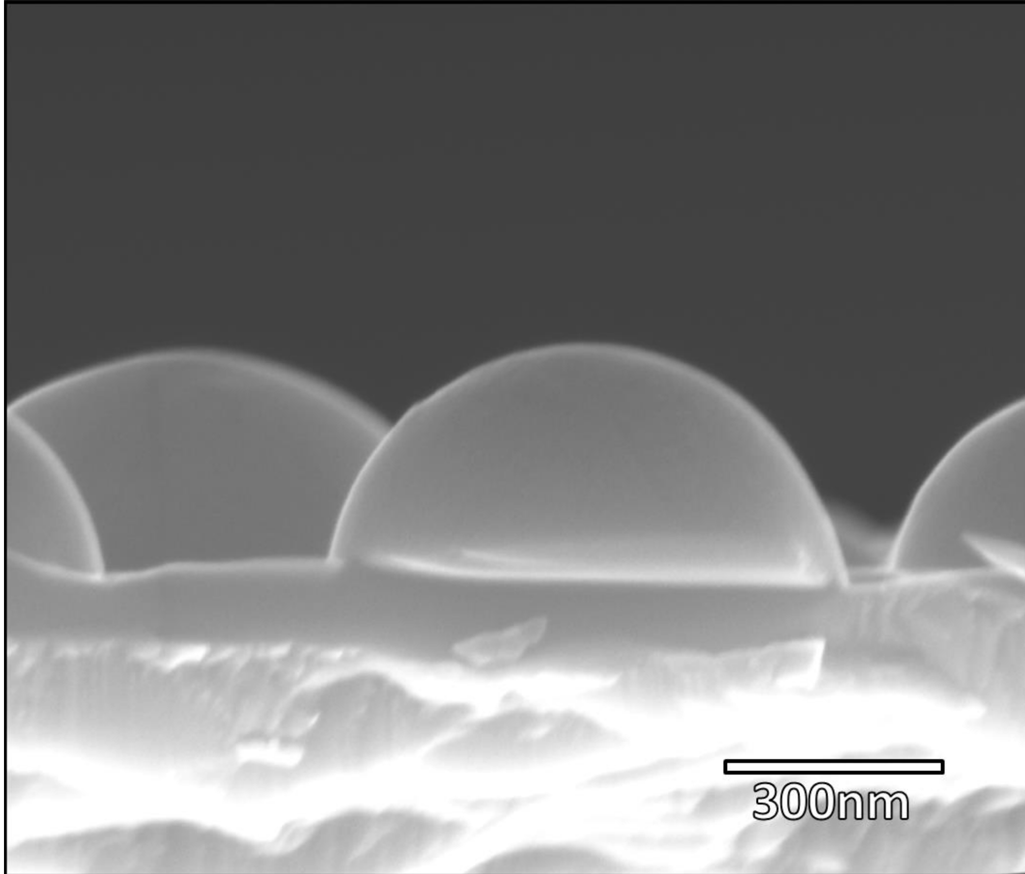

Figure 6.2: Cross-sectional SEM images of Bi droplets on sample D at T_s=360°C.

Table I: Sample List

Sample	Temp (^oC)	Growth time (min)	Ga BEP (Torr)	As BEP (Torr)	Bi BEP (Torr)
A	320	45	$2x10^{-7}$	$5.5x10^{-6}$	$5.4x10^{-8}$
B	320	45	$2x10^{-7}$	$5.4x10^{-6}$	$1.1x10^{-7}$
C	320	45	$2x10^{-7}$	$6.1x10^{-6}$	$1.4x10^{-6}$
D	360	45	$2x10^{-7}$	$5.5x10^{-7}$	$6.2x10^{-7}$
E	360	10	$2x10^{-7}$	$1.0x10^{-6}$	$5x10^{-7}$
F	360	5	$2x10^{-7}$	$1.0x10^{-6}$	$7x10^{-7}$
G	360	45	$2x10^{-7}$	$5.6x10^{-7}$	$6.4x10^{-7}$
H	400	40	$2x10^{-7}$	$5.6x10^{-6}$	$1.1x10^{-6}$
I	330	20	$4x10^{-7}$	$4.0x10^{-6}$	$2.0x10^{-8}$
J	380	20	$1.6x10^{-7}$	$5.7x10^{-7}$	$5x10^{-7}$
K	400	40	$2.1x10^{-7}$	$5.6x10^{-6}$	$5.5x10^{-7}$
L	250	50	$2.4x10^{-7}$	$5.6x10^{-6}$	$3.2x10^{-8}$ (15s only)
	-	-	In BEP (Torr)	-	-
M	270	0.25	N/A	N/A	$7x10^{-7}$
N	320	60	$2x10^{-7}$	$3.0x10^{-6}$	$3x10^{-7}$

6.3.2 Self-terminating VLS growth

In addition to a fast crystallization flux at the Bi_ℓ-$GaAs_s$ interface, the droplet needs to be stable over long periods of time in order for VLS growth to occur (**Fig. 6.1b**). **Figure 6.3** shows an example of a growth in which both of these conditions are met and VLS growth is observerd. The growth in **Fig. 6.3** corresponds to concurrent deposition of Ga (BEP_{Ga}= $2x10^{-7}$ Torr), As (BEP_{As}=$1x10^{-6}$ Torr), and Bi (BEP_{Bi}=$5x10^{-7}$ Torr) for 10 minutes. Multiple lens-shaped droplets approximately 1.5μm in diameter can be seen across the image. Adjacent to each of these droplets is a disc or staircase of discs approximately 300nm in height. There is no preferential direction of the sequence of discs; some are linearly aligned while others are stacked along random directions. For some nanostructures a very small droplet of Bi can be seen near the disc opposite the larger Bi droplet. These disc nanostructures clearly form via VLS growth in which the bismuth droplet increases in diameter with every subsequent step. This is because the concurrent Bi flux is slightly higher than the rate of desorption. While the change in catalyst size during growth has been reported, it has been primarily observed for tapered nanowires formed due to the evaporation or incorporation of the catalyst.[32]

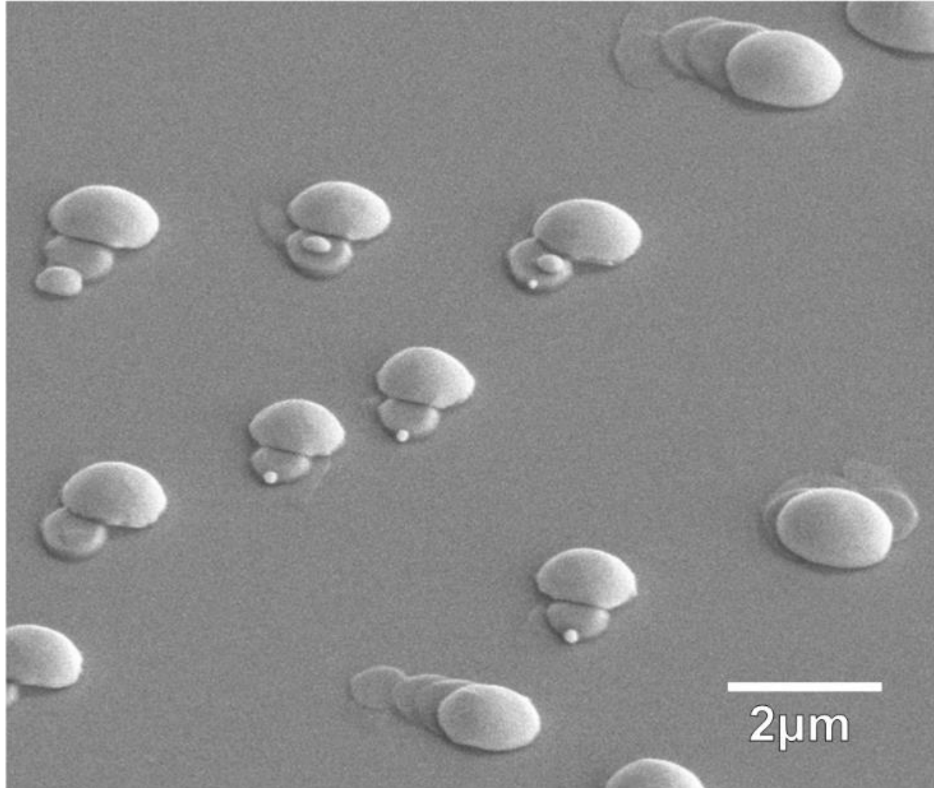

Figure 6.3: 45° angled SEM image of staircase nanostructures formed on sample E. Identical structures also appeared on Sample F.

6.3.3 Catalyst destabilization mechanism

The features in **Fig. 6.3** can be explained by using simple geometric considerations of the VLS growth process, detailed in a schematic in **Fig. 6.4**. All Bi_ℓ droplets form as a result of the initial Bi deposition step (**Fig. 6.4a**). Vapor elements are incorporated into the droplet and, solid GaAs begins to form at the Bi_ℓ-GaAs interface (**Fig. 6.4b**). If the arrival rate of Bi is larger than the desorption rate, as is the case for **Fig. 6.3**, the droplet will grow in volume but remains pinned to the initial disc diameter.[33] As a result, the contact angle θ must increase to accommodate the additional volume (**Fig. 6.4c**) Assuming that the droplet diameter is pinned to the initial disc diameter, the contact angle will continue to increase until it reaches a critical angle θ_c (**Fig. 6.4d**) after which the droplet will

destabilize and spill off the disc (**Fig. 6.4g**). θ_c is given by the Gibb's criterion $\theta_c = \theta_w + (180^o - \varphi)$, where θ_w is the wetting angle between the liquid droplet and the substrate, and φ is the angle between the droplet-disc interface and the disc sidewall.[34] In these experiments, $\varphi = 90^o$ such that $\theta_c = 168 \pm 2^o$.This method assumes that the droplet is pined to the initial disc diameter.

Another possibility is that as the droplet fails due to sidewall wetting. In this case, the droplet does not remain pinned at the disc edges and instead wets the disc sidewalls as it grows larger. Similar behavior has been observed on the macroscale with deionized water.[33] As more Bi is deposited, an increased proportion of the droplet extends down the sidewall and the vapor-liquid-solid triple junction approaches the substrate (**Fig. 6.3e**). Once the triple junction reaches the substrate (**Fig. 6.3f**), the surface tension is broken and the droplet spills off the disc to wet the substrate and reestablish its equilibrium shape, though at a larger diameter (**Fig. 6.3g**). Due to the high density of liquid Bi_ℓ, the entire droplet is carried to one side with the momentum of the spilling portion, in agreement with the behavior of mercury droplets.[34] As seen in **Fig. 6.2**, sometimes a small portion of the droplet separates from the main droplet and either remains on the surface of the disc or spills off the opposite edge. This process of the catalyst repeatedly reaching a supercritical state and dropping off the disc continues stepwise over the duration of the growth (**Fig. 6.3h**).

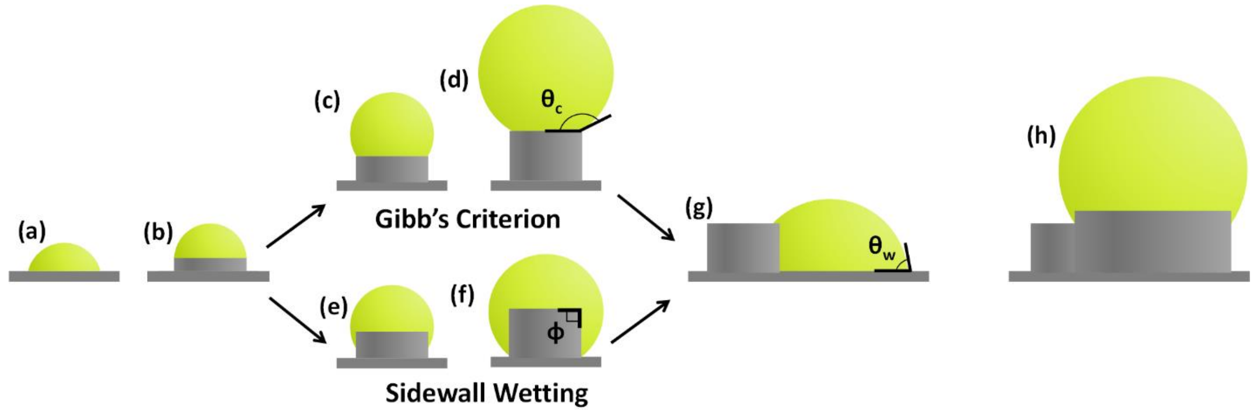

Figure 6.4: Schematic illustrating the stages of staircase nanostructure formation. a) Initial Bi_ℓ droplet formation, b) catalysis of GaAs VLS growth c) droplet growth with pinned edges, d) droplet destabilization by the Gibb's Criterion, e) droplet growth with sidewall wetting, f) droplet destabilization by substrate contact, g) droplet re-equilibrates on substrate, and h) growth of a new disc.

Both methods in **Fig. 6.4** are feasible, but the θ_c is vastly different in both Gibb's Criterion and sidewall wetting destabilization. θ_c may be determined experimentally by measuring the dimensions of subsequent discs in the SEM images. Assuming the droplets are spherical sections and pinned at the edges with no sidewall wetting, the volume of the droplet is given by:

$$V = \frac{\pi}{6}\left(3\tan\frac{\theta}{2} + \left(tan\frac{\theta}{2}\right)^3\right)r^3 \tag{1}$$

where r is the radius of the disc and θ is the contact angle. The radii is measured directly from the discs in the SEM images (**Fig. 6.2**). We assume that droplet-sidewall pinning occurs before significant droplet growth such that the volume of the droplet at the critical angle is equal to that of the droplet that has spilled off the disc. Substituting the segment radii and contact angles of both the critical and re-equilibrated droplet into the expression for the droplet volume (1), we obtain a single equation with one unknown, the θ_c. The

critical angle θ_c becomes a function of the initial disc radius r_1, the final disc radius r_2, and θ_w such that:

$$3\tan\left(\frac{\theta_c}{2}\right) + \tan^3\left(\frac{\theta_c}{2}\right) = \left[3\tan\left(\frac{\theta_w}{2}\right) + \tan^3\left(\frac{\theta_w}{2}\right)\right]\left(\frac{r_2}{r_1}\right)^3 \quad (2)$$

Twenty-one different staircase structures were measured to provide an average distribution of the critical contact angle. The disc radii range in diameters from 220 to 500nm and only droplets with at least two uncovered discs were included. We find the θ_c from equation 2 to be $\theta_c = 97\pm13^o$. This is significantly lower than the Gibb's criterion, suggesting the droplet destabilizes prior to reaching this limit. Furthermore, a spherical segment with a contact angle that obeys the Gibb's Criterion with segment radii measured in the SEM images would have a volume approximately twenty times that of solidified Bi droplets pictured in **Fig. 6.2** and diameters 2.7 times larger. Due to Bi desorption during sample quenching, it is probable that the liquid Bi_ℓ droplets at growth temperature are slightly larger than those in **Fig. 6.2**, but this would not account for a factor of twenty difference. Also, the density of features in **Fig. 6.2** would not account for such large Bi_ℓ droplets as the separation between some features is less than 2.7 times the diameter of the solidified Bi.

Therefore, based on the dimensions of the SEM features, it is improbable that the droplet reached the Gibb's criterion and instead destabilized due to sidewall wetting (**Fig. 6.4e-f**). The observed $\theta_c = 97\pm13^o$ suggests that there is a very short time frame in which nanowire growth can propagate before droplet destabilization. The growth is significantly limited due to sidewall wetting and precise instrument controls are necessary to repeatedly manage Bi flux to create nanostructures.

In some cases we were able to observe nanowire type formations across the sample. **Figure 6.5** shows a collection of these features in Samples I-L which have various growth parameters. With the exception of Sample J, these features were not consistent across the surface and only appeared in a few locations. It is likely these features were allowed to form due to random fluctuations in growth that occurred across the sample. In **Figure 6.5a** horizontal features appear above the surface of the substrate. These features closely resemble a nanowire that may be grown at a shallow angle to the substrate. The surrounding substrate growth caused the majority of this nanowire to be embedded. A Bi droplet can be seen at the end of the horizontal nanowire. These features were only observed in one or two regions across the sample. Specifically they were observed in a region of the sample that was depressed with the surrounding substrate, possibly because of a screw dislocation or other propagating defect at the surface. The remainder of the surface simply showed Bi droplets similar to **Fig. 6.1b**. It is possible this type of horizontal nanowire growth occurred across the whole sample and was only visible in this depressed region where substrate growth was limited. It is also possible that the balance of fluxes at these depressed regions allowed for the appropriate balance to create these nanostructures. Sample J (**Fig. 6.5b**) also exhibited these horizontal nanowire growths but across the entire surface. In these images the droplet is surrounded by a ring, as if the feature is being covered by th surrounding substrate growth. Attempts at repeating this growth however were unsuccessful, and resulted in growths with Bi droplets. **Figure 6.5c** shows a solitary nanowire growth on Sample K. Similar to Sample I (**Fig. 6.5a**) this feature was observed in a depressed region of the sample. However, this completely vertical nanowire was only observed in one location and smaller staircase

structures observed in **Fig. 6.3** were seen in other depressed regions. Similar to **Fig. 6.5a** it is unclear what growth conditions allowed for this solitary nanowire to grow. Lastly, a nanowire cluster is observed in Sample L (**Fig. 6.5d**). The cluster consists of many different nanowires that extend in many different directions and sometimes collide with each other. Some of the longer nanowires extend over the substrate in all directions. Underneath these longer nanowires are depressed regions in the film, observed by the darker contrast. This suggests that these longer nanowires may be shadowing the substrate from the incoming GaAs flux. The inset shows a close up of the center of the cluster, showing that these nanowires are coated in Bi droplets. It appears that these Bi droplets can catalyzing nanowire growth on top other nanowires, forming the cluster present in **Fig. 6.5d**. Similar to the other features present in **Fig. 6.5**, it is unclear what growth conditions caused this feature to form, or if it originated from a defect already on the substrate. It is possible that the growth condition within this cluster were favorable to nanowire growth, allowing rampant nanowire formation in multiple directions. Based on the observations in **Fig. 6.3** and **Fig. 6.5** it is likely that GaAs nanowire growth is theoretically possible with a Bi catalyst but experimentally inaccessible as of yet due to extremely precise growth requirements.

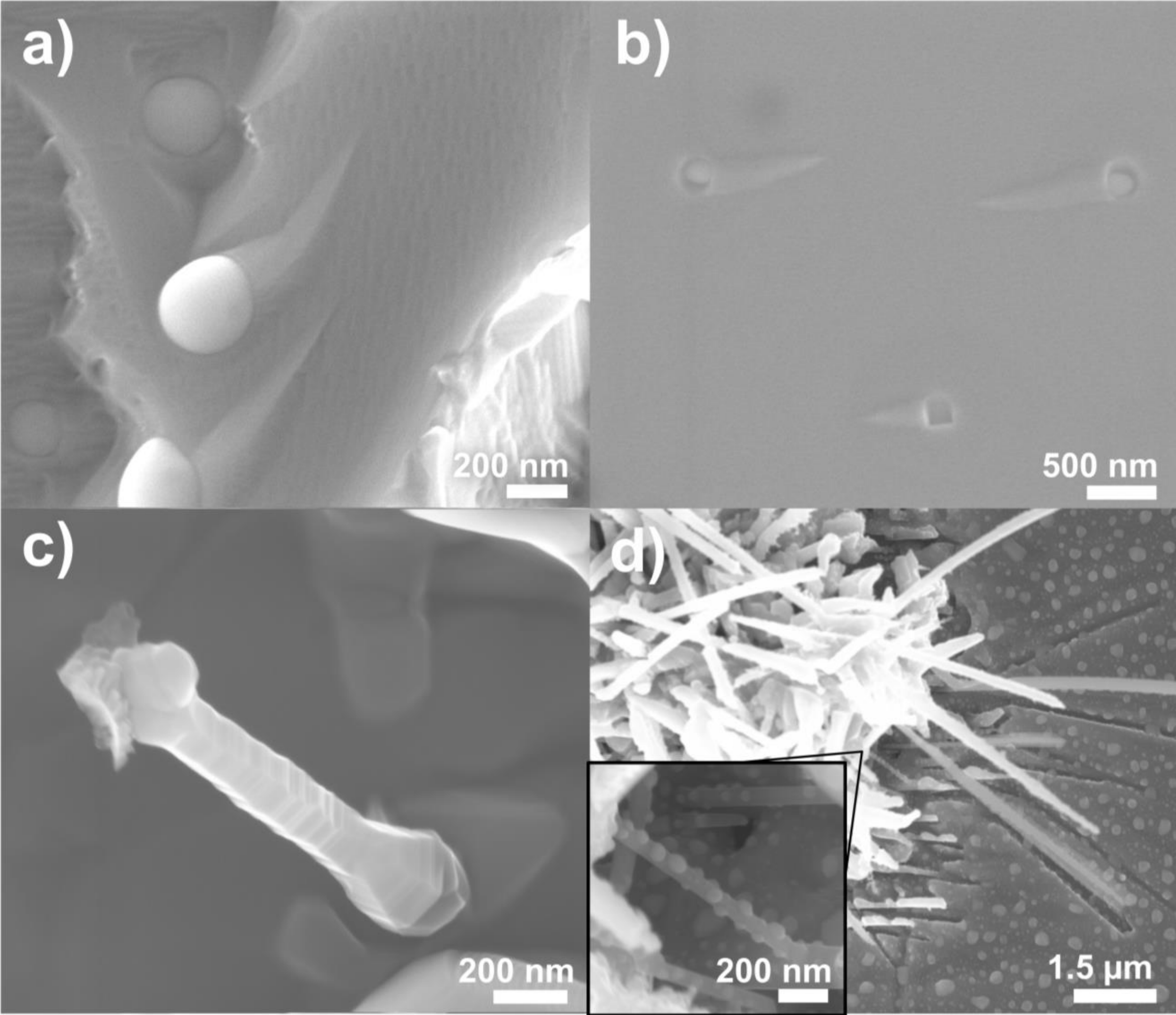

Figure 6.5: SEM images of nanowire features that are overgrown observed in a) Sample I and b) Sample J as well as nanowire features above the surface in c) Sample K and Sample L

6.3.4 Other Material Systems

Some preliminary work was done using other material systems in addition to Ga-As-Bi VLS growth. **Figure 6.6** shows cross sectional images of InAs catalyzed Bi growth. **Figure 6.6a** shows the result of Bi deposition on InAs films. A cross section of the droplet shows that the droplet significantly dissolves the underlying InAs substrate. This is significantly different than Bi droplets on GaAs (**Fig. 6.2**). Attempts at VLS catalyzed InAs growth only resulted in droplet formation as seen in **Fig. 6.6b**. Cross sections of these samples were consistent with the Bi droplet study in Sample M (**Fig. 6.6a**) showing noticeable substrate dissolution. It is unclear whether the increased dissolution of InAs in Bi is advantageous or disadvantageous to VLS growth.

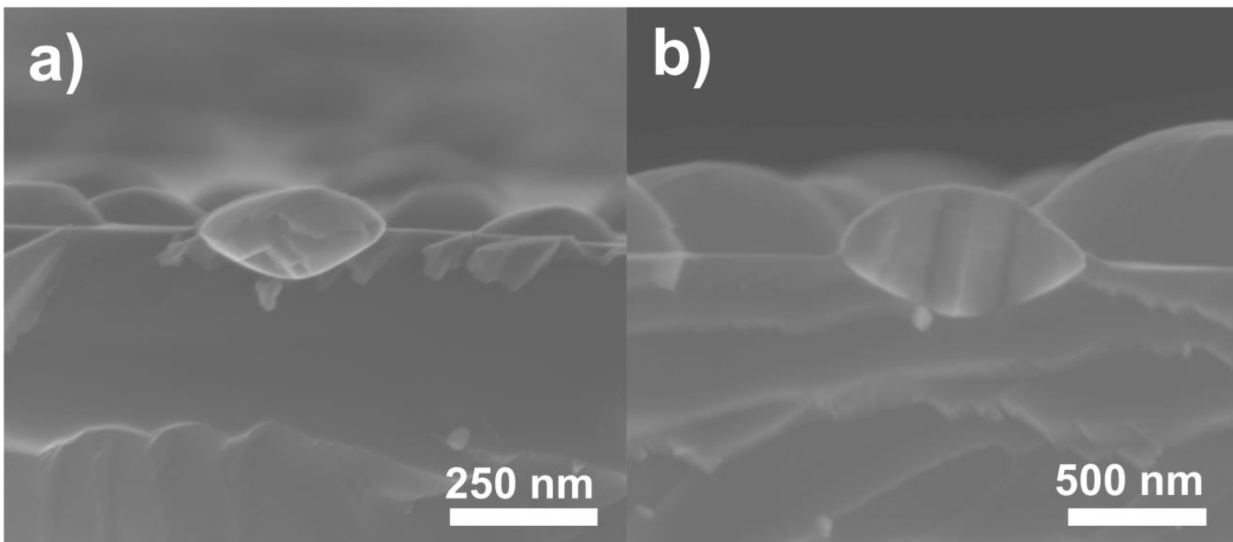

Figure 6.6: Bi droplets on InAs without concurrent InAs deposition on a) Sample M and with concurrent InAs deposition on b) Sample N

Lastly, attempts were made to use Sb to catalyze VLS growth on GaAs. However, at the substrate temperatures used in this study no droplet formation was observed and attempts only resulted in film growth.

6.4 Conclusions

Despite showing evidence that VLS mechanism is capable of producing Bi-catalyzed epitaxial GaAs nanostructures, this process is severely limited by sidewall wetting induced droplet destabilization. A concurrent Bi flux needs to be applied to maintain the size of the catalyst due to the high volatility of the liquid Bi_ℓ at growth temperatures. If the Bi deposition rate is only slightly greater than the desorption rate, the droplet is stable enough to catalyze VLS growth but will grow in size resulting in a unique staircase nanostructure. As the droplet grows, it begins to wet the sidewall until the triple point of the droplet extends to the substrate and the surface tension is broken. This dynamic catalyst technique could be used in the formation of Bi catalyzed GaAs nanowires. If the growth rate at the Bi_ℓ-GaAs interface is faster than the propagation of the triple point down the sidewall, destabilization could be delayed or prevented allowing for nanowire formation. However, this requires precise control over the equipment.

6.5 GaAs Nanowire Motivation and Applications

GaAs nanowires have been studied for a wide arrange of applications from photovoltaics,[35,36] biosensors,[37,38] thermoelectrics,[39,40] light emitting diodes,[41,42] transistors,[43,44] photodetectors,[42,45] and even nanolasers.[46,47] Despite demonstrating record breaking performance in some fields,[4] the challenge nanowires have faced is transferring this performance to a commercial scale.

For this reason, utilizing nanowires' unique growth processes for integrating nanowires for on-chip optoelectronics may be a more commercially viable avenue. Low power and wireless communication technologies have enabled the miniaturization of complete computer systems to millimeters and smaller.[48-50] These remote sensors

promise revolutionary methods of data collection for machine learning, environmental monitoring, and healthcare.[51-52] With dimensions on the scale of a millimeter, each additional feature added to the sensor can significantly increase the overall size. Optoelectronic devices, such as a photovoltaic cell, light emitting diode, or photodetector are often incorporated in conjunction with a silicon logic chip.[53,54] Because of fundamental material differences between the optoelectronic device and the silicon logic chip, two components, instead of one, need to be attached to the sensor. Specifically, the optoelectronic device is typically made from III-V compound semiconductors which are not lattice matched with either the silicon wafer or the exposed metal contacts on the surface of the silicon wafer.[55,56] Nanowires may be a low cost solution to integrate these devices on the same wafer. III-V nanowires grown on the exposed metal pads of the silicon logic chip could function as the optoelectronic device. Dislocations which propagate during lattice mismatched epitaxial growth do not impact a nanowire's crystal quality due to the nanowire's small radial dimensions and high percentage of surface area.[57]

Another area where GaAs nanowires may be useful is for biosensing. Nanowires are very appealing for sensors and biological applications because of the ability to detect small electrical changes in the nanowire based on functionalization by a biological agent.[5,37,38] However, there is not one nanowire device for all bio applications and nanowires are just a tool for detection of specific traits. For example, GaAs nanowire field effect transistors have been used to detect the electrical activity of human skeletal muscles. Researchers used a stochastic resonance technique to measure weak electromyogram signals, the electrical signals induced by muscle contraction. Using the

nanowire FET's they were able to obtain a signal to noise ratio than those of conventional detection techniques.[37]

6.6 References

1. Johnson, Justin C., et al. "Single gallium nitride nanowire lasers." *Nature materials* 1.2 (2002): 106-110.

2. Nozik, A. J. (2002). Quantum dot solar cells. *Physica E: Low-dimensional Systems and Nanostructures*, *14*(1), 115-120.

3. Tian, B., Zheng, X., Kempa, T. J., Fang, Y., Yu, N., Yu, G., ... & Lieber, C. M. (2007). Coaxial silicon nanowires as solar cells and nanoelectronic power sources. *Nature*, *449*(7164), 885-889.

4. Boukai, A. I., Bunimovich, Y., Tahir-Kheli, J., Yu, J. K., Goddard Iii, W. A., & Heath, J. R. (2008). Silicon nanowires as efficient thermoelectric materials. *Nature*, *451*(7175), 168-171.

5. Gao, Z., Agarwal, A., Trigg, A. D., Singh, N., Fang, C., Tung, C. H., ... & Kong, J. (2007). Silicon nanowire arrays for label-free detection of DNA. *Analytical Chemistry*, *79*(9), 3291-3297.

6. Wagner, R. S., & Ellis, W. C. (1964). Vapor-liquid-solid mechanism of single crystal growth. *Applied Physics Letters*, *4*(5), 89-90.

7. Kratzer, P., Sakong, S., & Pankoke, V. (2012). Catalytic role of gold nanoparticle in GaAs nanowire growth: a density functional theory study. *Nano letters*, *12*(2), 943-948.

8. Givargizov, E. I. (1975). Fundamental aspects of VLS growth. *Journal of Crystal Growth*, *31*, 20-30.

9. Dick, K. A., Deppert, K., Mårtensson, T., Mandl, B., Samuelson, L., & Seifert, W. (2005). Failure of the vapor-liquid-solid mechanism in Au-assisted MOVPE growth of InAs nanowires. *Nano letters*, *5*(4), 761-764.

10. Dubrovskii, V. G., Cirlin, G. E., Sibirev, N. V., Jabeen, F., Harmand, J. C., & Werner, P. (2011). New mode of vapor− liquid− solid nanowire growth. *Nano letters*, *11*(3), 1247-1253.

11. Schwarz, K. W., & Tersoff, J. (2010). Elementary processes in nanowire growth. *Nano letters*, *11*(2), 316-320.

12. Tian, B., Xie, P., Kempa, T. J., Bell, D. C., & Lieber, C. M. (2009). Single-crystalline kinked semiconductor nanowire superstructures. *Nature nanotechnology*, *4*(12), 824-829.

13. Schwarz, K. W., & Tersoff, J. (2012). Multiplicity of steady modes of nanowire growth. *Nano letters*, *12*(3), 1329-1332.

14. Oh, S. H., Benthem, K. V., Molina, S. I., Borisevich, A. Y., Luo, W., Werner, P., ... & Pennycook, S. J. (2008). Point defect configurations of supersaturated Au atoms inside Si nanowires. *Nano letters*, *8*(4), 1016-1019.

15. Allen, J. E., Hemesath, E. R., Perea, D. E., Lensch-Falk, J. L., Li, Z. Y., Yin, F., ... & Lauhon, L. J. (2008). High-resolution detection of Au catalyst atoms in Si nanowires. *Nature nanotechnology*, *3*(3), 168-173.

16. Bae, J., Kulkarni, N. N., Zhou, J. P., Ekerdt, J. G., & Shih, C. K. (2008). VLS growth of Si nanocones using Ga and Al catalysts. *Journal of Crystal Growth*, *310*(20), 4407-4411.

17. Grap, T., Rieger, T., Blömers, C., Schäpers, T., Grützmacher, D., & Lepsa, M. I. (2013). Self-catalyzed VLS grown InAs nanowires with twinning superlattices. *Nanotechnology*, *24*(33), 335601.

18. Ambrosini, S., Fanetti, M., Grillo, V., Franciosi, A., & Rubini, S. (2011). Vapor-liquid-solid and vapor-solid growth of self-catalyzed GaAs nanowires. *AIP Advances*, *1*(4), 042142.

19. Ambrosini, S., Fanetti, M., Grillo, V., Franciosi, A., & Rubini, S. (2011). Self-catalyzed GaAs nanowire growth on Si-treated GaAs (100) substrates. *Journal of Applied Physics*, *109*(9), 094306.

20. Cirlin, G. E., Dubrovskii, V. G., Samsonenko, Y. B., Bouravleuv, A. D., Durose, K., Proskuryakov, Y. Y., ... & Zeze, D. (2010). Self-catalyzed, pure zincblende GaAs nanowires grown on Si (111) by molecular beam epitaxy. *Physical Review B*, *82*(3), 035302.

21. Wang, N., Zhang, Y., & Zhu, J. (2001). Growth of silicon nanowires via nickel/SiCl4 vapor-liquid-solid reaction. *Journal of materials science letters*, *20*(1), 89-91.

22. Yella, A., Mugnaioli, E., Panthöfer, M., Therese, H. A., Kolb, U., & Tremel, W. (2009). Bismuth-Catalyzed Growth of SnS2 Nanotubes and Their Stability. *Angewandte Chemie International Edition*, *48*(35), 6426-6430.

23. Fanfair, D. D., & Korgel, B. A. (2005). Bismuth nanocrystal-seeded III-V semiconductor nanowire synthesis. *Crystal growth & design*, *5*(5), 1971-1976.

24. Lee, S. K., Yu, Y., Perez, O., Puscas, S., Kosel, T. H., & Kuno, M. (2009). Bismuth-assisted CdSe and CdTe nanowire growth on plastics. *Chemistry of Materials*, *22*(1), 77-84.

25. Volobuev, V. V., Stetsenko, A. N., Mateychenko, P. V., Zubarev, E. N., Samburskaya, T., Dziawa, P., ... & Sipatov, A. Y. (2011). Bi catalyzed VLS growth of PbTe (001) nanowires. *Journal of Crystal Growth*, *318*(1), 1105-1108.

26. Yu, L., Fortuna, F., O'Donnell, B., Jeon, T., Foldyna, M., Picardi, G., & Roca i Cabarrocas, P. (2012). Bismuth-catalyzed and doped silicon nanowires for one-pump-down fabrication of radial junction solar cells. *Nano letters*, *12*(8), 4153-4158.
27. Lide, D. R. (Ed.). (2004). *CRC handbook of chemistry and physics* (Vol. 85). CRC press.
28. Li, C., Zeng, Z. Q., Fan, D. S., Hirono, Y., Wu, J., Morgan, T. A., ... & Salamo, G. J. (2011). Bismuth nano-droplets for group-V based molecular-beam droplet epitaxy. *Applied Physics Letters*, *99*(24), 243113.
29. Vardar, G., Paleg, S. W., Warren, M. V., Kang, M., Jeon, S., & Goldman, R. S. (2013). Mechanisms of droplet formation and Bi incorporation during molecular beam epitaxy of GaAsBi. *Applied Physics Letters*, *102*(4), 042106.
30. Reyes, K., Smereka, P., Nothern, D., Millunchick, J. M., Bietti, S., Somaschini, C., ... & Frigeri, C. (2013). Unified model of droplet epitaxy for compound semiconductor nanostructures: experiments and theory. *Physical Review B*, *87*(16), 165406.
31. DeJarld, M., Reyes, K., Smereka, P., & Millunchick, J. M. (2013). Mechanisms of ring and island formation in lattice mismatched droplet epitaxy. *Applied Physics Letters*, *102*(13), 133107.
32. Cao, L., Garipcan, B., Atchison, J. S., Ni, C., Nabet, B., & Spanier, J. E. (2006). Instability and transport of metal catalyst in the growth of tapered silicon nanowires. *Nano letters*, *6*(9), 1852-1857.
33. Mueller, J., Haghparastmojaveri, N., Alan, T., & Neild, A. (2013). The role height plays in the spreading of liquid droplets over sharp edges. *Applied Physics Letters*, *102*(4), 041605.

34. Oliver, J. F., Huh, C., & Mason, S. G. (1977). Resistance to spreading of liquids by sharp edges. *Journal of Colloid and Interface Science*, *59*(3), 568-581.

35. Czaban, J. A., Thompson, D. A., & LaPierre, R. R. (2008). GaAs core− shell nanowires for photovoltaic applications. *Nano Letters*, *9*(1), 148-154.

36. Colombo, C., Heiss, M., Grätzel, M., & Fontcuberta i Morral, A. (2009). Gallium arsenide pin radial structures for photovoltaic applications. *Applied Physics Letters*, *94*(EPFL-ARTICLE-148563).

37. Imai, Y., Sato, M., Tanaka, T., Kasai, S., Hagiwara, Y., Ishizaki, H., ... & Arakawa, T. (2014). Detection of weak biological signal utilizing stochastic resonance in a GaAs-based nanowire FET and its parallel summing network. *Japanese Journal of Applied Physics*, *53*(6S), 06JE01.

38. Patolsky, F., Zheng, G., & Lieber, C. M. (2006). Nanowire sensors for medicine and the life sciences.

39. Mingo, N. (2004). Thermoelectric figure of merit and maximum power factor in III–V semiconductor nanowires. *Applied Physics Letters*, *84*(14), 2652-2654.

40. Martin, P. N., Aksamija, Z., Pop, E., & Ravaioli, U. (2010). Reduced thermal conductivity in nanoengineered rough Ge and GaAs nanowires. *Nano letters*, *10*(4), 1120-1124.

41. Tomioka, K., Motohisa, J., Hara, S., Hiruma, K., & Fukui, T. (2010). GaAs/AlGaAs core multishell nanowire-based light-emitting diodes on Si. *Nano letters*, *10*(5), 1639-1644.

42. Gudiksen, M. S., Lauhon, L. J., Wang, J., Smith, D. C., & Lieber, C. M. (2002). Growth of nanowire superlattice structures for nanoscale photonics and electronics. *Nature*, *415*(6872), 617-620.

43. Kasai, S., & Asai, T. (2008). Stochastic resonance in schottky wrap gate-controlled GaAs nanowire field-effect transistors and their networks. *Applied physics express*, *1*(8), 083001.

44. Miao, X., Chabak, K., Zhang, C., K. Mohseni, P., Walker Jr, D., & Li, X. (2014). High-Speed Planar GaAs Nanowire Arrays with f max> 75 GHz by Wafer-Scale Bottom-up Growth. *Nano letters*, *15*(5), 2780-2786.

45. Seyedi, M. A., Yao, M., O'Brien, J., Wang, S. Y., & Dapkus, P. D. (2014). Efficient Schottky-like junction GaAs nanowire photodetector with 9 GHz modulation bandwidth with large active area. *Applied Physics Letters*, *105*(4), 041105.

46. Saxena, D., Mokkapati, S., Parkinson, P., Jiang, N., Gao, Q., Tan, H. H., & Jagadish, C. (2013). Optically pumped room-temperature GaAs nanowire lasers. *Nature Photonics*, *7*(12), 963-968.

47. Mayer, B., Rudolph, D., Schnell, J., Morkötter, S., Winnerl, J., Treu, J., ... & Finley, J. J. (2013). Lasing from individual GaAs-AlGaAs core-shell nanowires up to room temperature. *Nature communications*, *4*.

48. Jung, W., Oh, S., Bang, S., Lee, Y., Foo, Z., Kim, G., ... & Blaauw, D. (2014). An ultra-low power fully integrated energy harvester based on self-oscillating switched-capacitor voltage doubler. *IEEE Journal of Solid-State Circuits*, *49*(12), 2800-2811.

49. Lee, Y., Bang, S., Lee, I., Kim, Y., Kim, G., Ghaed, M. H., ... & Blaauw, D. (2013). A Modular 1 mm Die-Stacked Sensing Platform With Low Power I C Inter-Die

Communication and Multi-Modal Energy Harvesting. *IEEE Journal of Solid-State Circuits*, *48*(1), 229-243.

50. Fojtik, M., Kim, D., Chen, G., Lin, Y. S., Fick, D., Park, J., ... & Sylvester, D. (2013). A millimeter-scale energy-autonomous sensor system with stacked battery and solar cells. *IEEE Journal of Solid-State Circuits*, *48*(3), 801-813.
51. Gubbi, J., Buyya, R., Marusic, S., & Palaniswami, M. (2013). Internet of Things (IoT): A vision, architectural elements, and future directions. *Future Generation Computer Systems*, *29*(7), 1645-1660.
52. Lee, I., Kim, Y., Bang, S., Kim, G., Ha, H., Chen, Y. P., ... & Foo, Z. (2014, September). Circuit techniques for miniaturized biomedical sensors. In *CICC* (pp. 1-7).
53. Teran, A. S., Wong, J., Lim, W., Kim, G., Lee, Y., Blaauw, D., & Phillips, J. D. (2015). AlGaAs photovoltaics for indoor energy harvesting in mm-scale wireless sensor nodes. *IEEE Transactions on Electron Devices*, *62*(7), 2170-2175.
54. Warneke, B. A., Scott, M. D., Leibowitz, B. S., Zhou, L., Bellew, C. L., Chediak, J. A., ... & Pister, K. S. (2002). An autonomous 16 mm 3 solar-powered node for distributed wireless sensor networks. In *Sensors, 2002. Proceedings of IEEE* (Vol. 2, pp. 1510-1515). IEEE.
55. Fischer, R., Morkoc, H., Neumann, D. A., Zabel, H., Choi, C., Otsuka, N., ... & Erickson, L. P. (1986). Material properties of high-quality GaAs epitaxial layers grown on Si substrates. *Journal of applied physics*, *60*(5), 1640-1647.
56. Tsai, H. L., & Lee, J. W. (1987). Defect structures at the GaAs/Si interface after annealing. *Applied physics letters*, *51*(2), 130-132.

57. Hersee, S. D., Rishinaramangalam, A. K., Fairchild, M. N., Zhang, L., & Varangis, P. (2011). Threading defect elimination in GaN nanowires. *Journal of Materials Research*, *26*(17), 2293-2298.

Chapter 7
Summary and Future Work

7.1 Summary and Conclusions

This work presents an analysis nanostructure growth mechanisms with the intention of providing a deeper understanding of how these growth mechanisms impact the final nanostructure's physical, electrical, and optical characteristics. The first three studies demonstrate how the shape and structure of embedded GaSb quantum dots can be manipulated by using different chemistries in the encapsulating layer or different growth mechanisms. Stranksi-Krastanov (SK) grown GaSb/GaAs quantum dots capped with $Al_xGa_{1-x}As$ show significant shape retention opposed to those capped with solely GaAs. The Al acts as a diffusion barrier to the Sb, preventing it from out-diffusing from the quantum dot core. This is revealed by XSTM measurements which show a reduced number of demolished quantum dots as well as an increase in the average quantum dot height. However, Sb out-diffusion was a method of relaxing the strain induced in the capping layer by the size of the quantum dot. With the inclusion of Al, this out-diffusion was curtailed and in order to compensate for size-induced the strain, stacking faults formed in the capping layer. This was also revealed by XSTM measurements which show an increase in the number of capping layer defects in the Al-rich samples. The photoluminescence spectrum of the quantum dot emission was also the same in all four

samples, possibly because of the presence of these defects. From this, it was clear that reducing the size of the quantum dots may prevent quantum dot demolition and capping layer defect formation. However, initial studies with GaSb quantum dots of various sizes showed no change in the photoluminescence response. As such, an alternative quantum dot growth mechanism, droplet epitaxy (DE), was explored and we were able to demonstrate that it could be used to create a wide range of GaSb epitaxial nanostructures. The process is heavily influenced by the size of the initial quantum dot as well as the substrate temperature due to a non-trivial energy barrier from the crystallization of lattice mismatched GaSb on GaAs. Next, the effects of capping on nanostructures grown by both methods, SK and DE, was investigated. It was revealed that the droplet epitaxy structures were significantly lower in composition and had shorter height profiles than their SK counterparts. This resulted in almost no quantum dot demolition or capping layer defects in the DE sample as measured by TEM. Despite this, the photoluminescence spectra were nearly identical, suggesting the large quantum dots in the SK sample are not contributing to the emission. Furthermore, it is likely this emission arises from the wetting layer as the Sb wetting layer concentration profiles were nearly identical in both the SK and DE samples.

The other two studies demonstrate how GaAs nanowire morphology, structure, and optical response is impacted by polycrystalline substrates, low temperatures, doping elements, and alternative catalysts. Specifically, using Au-assisted VLS growth we were able to grow GaAs nanowires on polycrystalline indium-tin-oxide films at substrate temperatures of T_s=400°C. The nanowires were heavily tapered, randomly oriented, and varied in height between 500nm and 2µm. When Si dopants were introduced for n-GaAs,

an increase in surface roughening was observed. When Be dopants were introduced for p-GaAs the nanowire morphology changed dramatically: the nanowire density and height increased, the nanowires were more uniform in height, and the tapering present in the undoped sample was almost non-existent. Nanowire growth on metallic Pt and Ti films were also investigated and revealed that a higher growth rate was necessary for complete nanowire coverage due to differences in substrate surface energy ($\gamma_{metal} > \gamma_{catalyst} > \gamma_{ITO}$). Electrical measurements revealed a Schottky contact between the ITO and p-GaAs naonwires and Ohmic contact between Ti and p-GaAs nanowires. Temperature dependent photoluminescence measurements of Be-doped GaAs nanowires on Ti showed room temperature luminescence with a high temperature thermal activation energy of ~14meV. The use of Bi as an alternative catalyst to Au was also investigated using single-crystalline GaAs substrates. Despite observing evidence of Bi-catalyzed growth, complete nanowires could not be grown. This is due to significant Bi vapor pressure at our desired substrate temperatures $300^oC \leq T_s \leq 400^oC$ requiring a concurrent Bi flux during growth. It was identified that after the initial nanopillar formation, the Bi catalyst would destabilize and return to the adjacent substrate film. The impinging Bi flux caused the droplet to grow and wet the sidewalls until it contacted the substrate. This resulted in the growth of unique staircase and buried nanostructures.

7.2 Future Work

The next steps in this work primarily involves improving the optical quality and device performance in the GaSb quantum dot and GaAs nanowire projects respectively. For GaSb quantum dots, we observed almost no change in the photoluminescence response despite significant changes in the physical structure of the embedded nanostructures. A literary search of reported GaSb quantum dot photoluminescence studies reveals that some researchers report emission around 1.22eV,[1-4] similar to our results, while others report emission near 1.0eV.[5-8] The reports that observe emission at 1.0eV consistently incorporate a high temperature anneal step into their growth. For this reason, it is my hypothesis that this high temperature annealing step may be improving the crystal structure of the GaSb/GaAs layer, especially in the capping layer near the quantum dot interface. The emission at 1.22eV that we observe in our experiments may be induced by the wetting layer and impurities at the GaSb-GaAs interface. The high temperature annealing step may eliminate these imperfections and enable the SK and DE quantum dots to luminesce. Furthermore, it is unclear what effect the high temperature annealing step has on the embedded quantum dot structure. The next step in this research would be to growing a capped DE structure similar to the one in Chapter 4 and anneal it at temperatures T_s=600°C prior to quenching in the MBE chamber. If there is noticeable change in the photoluminescence spectrum, further characterization including XSTM and TEM would be desirable. If there is no observable photoluminescence change, then the capping step will also be done at the high temperatures before being examined for differences in optical response.

For GaAs nanowires the next step is to obtain a better understanding of junction formation within these nanowires by demonstrating a P-N junction. Despite measuring I-V characteristics of core-shell nanowires, we continue to observe a linear resistive response. This could be due to multiple causes: 1) the doping levels in the nanowires are high enough that the carriers are tunneling through the depletion region, 2) the reactive ion etch step is etching through the n-type region and carriers are only transporting through the p-type region, 3) the n-type region in the taller nanowires are being etched completely away and a collective few nanowires are shorting the device, or 4) dopants are not being incorporated into the nanowires properly and we are not creating a P-N junction. I propose two concurrent methods of investigation. First, core-shell nanowires will be grown with varying levels of Si doping $0 \leq n_{planar} \leq 10^{19}$. These nanowires will be measured for their morphology using SEM, and some of them will be further analyzed for their structure via TEM, and electrical characteristics via the aforemented processing steps. Second, the electrical characteristics of single nanowires will be examined. This will be achieved by scattering nanowires across a substrate with pre-deposited metal pads. Regions of single nanowires will be then connected to the pads by depositing Pt using a focused ion beam. This method should first be tested with uniformly doped nanowires (Be) before attempting core-shell nanowires. The geometry of core-shell nanowires may make it difficult to confidently attach contacts to the P and N regions of the structure. One possibility would be to FIB out a section of the substrate and electrical contacts could be made between the tip of one wire and the milled out Si-substrate.

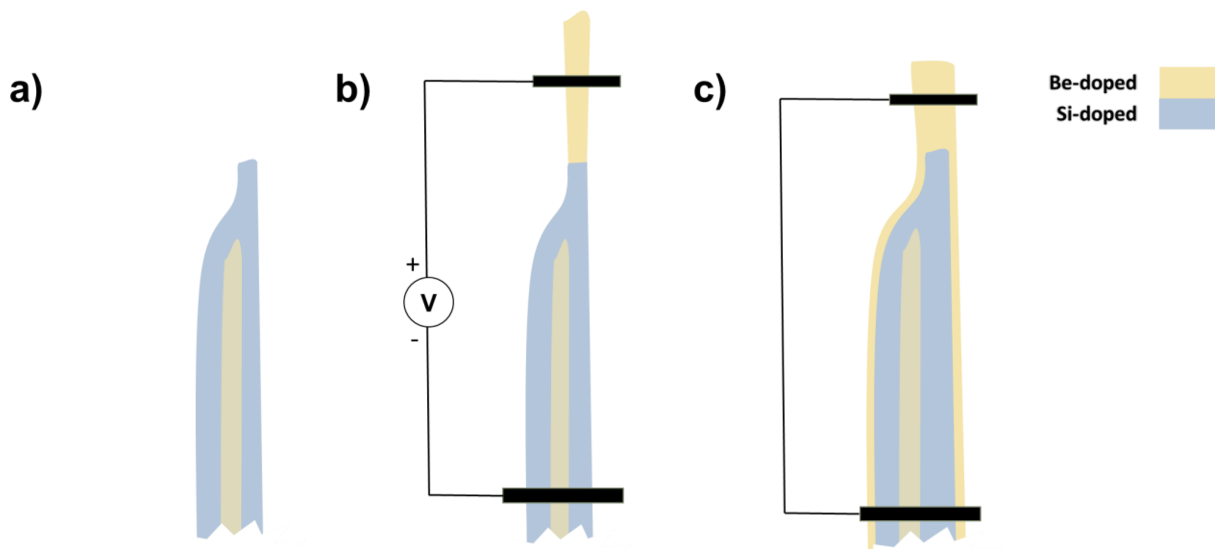

Figure 7.1: Schematic illustrating a proposed P-N-P nanowire device to measure the PN junction in GaAs nanowires. a) Core-shell nanowire and b) favorable and c) unfavorable P-N-P structure.

Another option might be to grow a P-N-P structure. A schematic detailing this growth is provided in **Figure 7.1.** Due to Be-doped nanowires strong response to catalytic growth, the Be doped growth may be isolated near the catalyst region only. This would create a junction between the N-shell and the P-type extension. However, if this growth results in a P-type shell around the Si-doped region then this solution would not work. Furthermore, it is important to note that the PN junction measured using this technique is not wholly representative of the core-shell junction. However, this could be a useful tool in analyzing the quality of the doped material and demonstrating proof of concept.

7.3 References

1. Nowozin, T., Marent, A., Bonato, L., Schliwa, A., Bimberg, D., Smakman, E. P., ... & Hayne, M. (2012). Linking structural and electronic properties of high-purity self-assembled GaSb/GaAs quantum dots. *Physical review b*, *86*(3), 035305.
2. Müller-Kirsch, L., Heitz, R., Schliwa, A., Stier, O., Bimberg, D., Kirmse, H., & Neumann, W. (2001). Many-particle effects in type II quantum dots. *Applied Physics Letters*, *78*(10), 1418-1420.
3. Suzuki, K., Hogg, R. A., & Arakawa, Y. (1999). Structural and optical properties of type II GaSb/GaAs self-assembled quantum dots grown by molecular beam epitaxy. *Journal of applied physics*, *85*(12), 8349-8352.
4. Kawazu, T., Noda, T., Mano, T., Sakuma, Y., & Sakaki, H. (2013). Growth of GaSb quantum dots on GaAs (311) A. *Journal of Crystal Growth*, *378*, 475-479.
5. Kunrugsa, M., Panyakeow, S., & Ratanathammaphan, S. (2015). GaSb/GaAs quantum-ring-with-dot structures grown by droplet epitaxy. *Journal of Crystal Growth*, *416*, 73-77.
6. Alonso-Álvarez, D., Alén, B., García Martínez, J. M., & Ripalda, J. M. (2007). Optical investigation of type II GaSb/GaAs self-assembled quantum dots.
7. Kawazu, T., Mano, T., Noda, T., & Sakaki, H. (2009). Optical properties of GaSb/GaAs type-II quantum dots grown by droplet epitaxy. *Applied Physics Letters*, *94*(8), 081911.
8. Lin, W. H., Wang, K. W., Lin, S. Y., & Wu, M. C. (2013). Improved 1.3-Electroluminescence of InGaAs-Capped Type-II GaSb/GaAs Quantum Rings at Room Temperature. *IEEE Photonics Technology Letters*, *25*(1), 97-99.